Pre-eruptive vapour and its role in controlling eruption style and longevity at Soufrière Hills Volcano

Marie Edmonds[1*], Madeleine C. S. Humphreys[2], Erik H. Hauri[3], Richard A. Herd[4], Geoff Wadge[5], Harriet Rawson[1], Rachel Ledden[1], Melissa Plail[4], Jenni Barclay[4], Alessandro Aiuppa[6, 7], Thomas Christopher[8], Gaetano Giudice[7], Roberto Guida[7]

1 Earth Sciences Dept, University of Cambridge, Downing Street, Cambridge CB2 3EQ, UK.
2 Earth Sciences Dept, University of Oxford, South Parks Road, Oxford OX1 3AN, UK.
3 Department of Terrestrial Magnetism, Carnegie Institution of Washington, 5241 Broad Branch Rd. NW, Washington DC 20015, USA.
4 School of Environmental Sciences, University of East Anglia, Norwich NR9 7TJ, UK.
5 National Centre for Earth Observation, Environmental Systems Science Centre, University of Reading, Reading, UK.
6 Dipartimento DiSTeM, Università di Palermo, Via Archirafi 36, I- 90123 Palermo, Italy.
7 Sezione di Palermo, Istituto Nazionale di Geofisica e Vulcanologia, Via Ugo La Malfa, 153, I-90146 Palermo, Italy.
8 Montserrat Volcano Observatory, Salem, Montserrat, West Indies.

*corresponding author; me201@cam.ac.uk

Abstract

We use volatiles in melt inclusions and nominally anhydrous phenocrysts, with volcanic gas flux and composition, and textural analysis of mafic inclusions, to estimate the mass of exsolved vapour prior to eruption at Soufrière Hills Volcano. Pre-eruptive andesite coexists with exsolved vapour comprising 1.6-2.4 wt% of the bulk magma. Water contents of orthopyroxenes indicate a zone of magma storage at pressures of ~260 MPa, whereas melt inclusions have equilibrated at shallower pressures. Inclusions containing >3 wt% H_2O are enriched in CO_2, suggesting flushing with CO_2-rich gases. Intruding mafic magma contains >8 wt% H_2O at 200-300 MPa. Rapid quenching is accompanied by crystallisation and vesiculation. Upon entrainment into the andesite, mafic inclusions undergo disaggregation, where expansion of volatiles in the interior overcomes the strength of the crystal frameworks, thereby recharging the vapour content of the andesite. Exsolved vapour may amount to 4.3-

8.2 vol% at 300 MPa, with implications for eruption longevity and volume; we estimate the magma reservoir volume to be 60-200 km^3. Exsolved vapour may account for the small volume change at depth during eruptions from geodetic models, and has implications for magma flow: exsolution is likely to in equilibrium during rapid magma ascent, with little nucleation of new bubbles.

1. Introduction

The 1995-2012 eruption of Soufrière Hills Volcano, Montserrat, has provided an unprecedented opportunity to quantify the volatile budget of a long-lived lava dome eruption and to study in detail the implications of pre-eruptive vapour and degassing on magma rheology, eruption dynamics and longevity, and for the interpretation of volcano monitoring data and hazard assessment. Arc volcanoes are typically volatile-rich, owing to the contribution of volatile species from devolatilisation of the subducting slab (Tatsumi & Eggins, 1995). The role that volatiles play in melting, fractionation, magma transport and shallow differentiation in arc settings is profound (Sisson and Grove, 1993, Moore and Carmichael, 1998; Schmidt and Poli, 1999). The generation of mafic magmas in the "hot zone" at the base of the arc crust is fundamentally controlled by the H_2O content of the melts, which act to "flux" the amphibolite crust and cause assimilation (Annen et al,. 2006). In shallow storage areas, the exsolved fluid content of stored magma directly influences the compressibility and hence response of the magma body to changes in pressure or volume, ultimately determining magma ascent rates and eruption style, as well as eruption duration and size (Huppert and Woods, 2002). The rate of crystallisation of magma in crustal reservoirs is influenced by the opposing effects of fluxing by CO_2-rich gases from depth, which act to "freeze" the magma (Blundy et al., 2010), and new batches of incoming hot, volatile-rich magma, which act to "defrost" it, by heating and transferring H_2O-rich fluids (e.g. Bachmann and Bergantz, 2006). Sulphur partitions into this fluid (e.g. Scaillet et al., 1998; Zajacz et al., 2012), further enhancing the proportion of vapour coexisting with the magma prior to the eruption, and acting as a convenient tracer to measure in volcanic gases (e.g. Gerlach et al., 2008). In the conduit, transitions between lava dome building and explosive Vulcanian activity are controlled by finely-balanced feedbacks involving the development of permeability during degassing, and the increase in viscosity and consequent retardation of bubble growth caused by crystallisation and H_2O exsolution from the melt (Melnik and Sparks, 1999; Sparks et al., 2000; Melnik and Sparks, 2002; Clarke et al., 2007). The arc magma system is complex; petrological and geochemical evidence points to the erupted porphyritic andesite being a hybrid, the result of perhaps countless recharge events by

pulses of more mafic magma derived from the deep crust (Zellmer et al., 2003; Humphreys et al., 2009a; 2012). Magma and volatiles are almost certainly decoupled for much of their evolution through the arc crust, and timescales for degassing and magma differentiation are likely to be different by orders of magnitude. Understanding the volatile budget is crucial both for volcano monitoring and hazards, and for understanding magmatic transport and evolution in the crust.

The eruption of the Soufrière Hills Volcano has shown complex cycles in eruption rates over long timescales (months to years), thought to be associated with the continuing recharge of magma from deep in the crust and with waxing and waning of overpressure in the magma reservoir, coupled with lava extrusion at the surface (Melnik et al., 2005; Elsworth et al., 2008; Wadge et al., 2010, this volume). The Soufrière Hills eruption is now entering its 17th year and its extraordinary longevity (only 2 similarly long-lived historical eruptions have taken place in the region; Wadge et al., this volume) is worthy of note. However, eruption duration and magnitude can be increased by up to two orders of magnitude if the stored internal energy associated with dissolved volatiles can be released into the magma chamber, and this is a mechanism for inducing complex eruption cycles on long timescales for volatile-rich magmas (Huppert and Woods, 2002). One mechanism for this is the presence of a large fraction of exsolved volatiles in the magma chamber, which increases magma compressibility (Rivalta and Segall, 2008). This effect is particularly important for magmas with a high crystallinity and associated volatile content. As the proportion of exsolved fluid is increased, the increase in compressibility leads to a larger mass of magma having to be erupted in order to relieve a given overpressure, and hence the duration of the resulting effusive eruption will be larger (Huppert and Woods, 2002). We have observed, throughout the eruption so far, that far more sulphur gases are degassed than can be accounted for by degassing of erupting magma alone (Edmonds et al., 2001; Christopher et al., 2010), and this has been ascribed to a pre-eruptive fluid phase containing the bulk of the sulphur (e.g. Wallace and Edmonds, 2011), and fluid replenishment by mafic magma intrusion and degassing (Edmonds et al., 2010). These two hypotheses are not mutually exclusive: we propose that the vapour phase coexisting with magma in the storage reservoir is fed and replenished by input of mafic magma. “Excess sulphur” is a common feature of intermediate eruptions in many tectonic settings, and is a consequence of the low solubility of sulphur in evolved melts, particularly under oxidising conditions (Scaillet et al., 1998; Clemente et al., 2004). Pre-eruptive vapour has been invoked to explain large gas emissions during many recent and historical eruptions (Wallace and Gerlach, 1994; Gerlach et al., 1994; Gerlach et al., 2008). A pre-eruptive exsolved vapour content of ~ 3 wt% was invoked for the dacite erupted in June 1991 at

Pinatubo (Scaillet and Evans, 1999). Melt inclusion studies of the Bishop Tuff rhyolite show that the magma chamber was stratified with respect to exsolved vapour, with <2 wt% in the deeper part of the system, to >6 wt% in the upper part of the magma reservoir (Wallace et al., 1995). Evidence for the preservation of "pre-entrapment" bubbles has also been found in the Bishop Tuff rhyolites, i.e. remnants of the vapour phase that existed in the magma chamber during slow crystallisation (Gualda and Anderson, 2007).

The Soufrière Hills Volcano magma contains abundant inclusions of more mafic magma (Murphy et al., 1998; Murphy et al., 2000; Barclay et al., 2010; Plail et al., this volume; Humphreys et al., 2012). Similar inclusions are documented from volcanic and plutonic settings elsewhere (Walker and Skelhorn, 1966; Eichelberger, 1980; Sparks and Marshall, 1986; Clynne, 1999; Coombs et al., 2006; Browne et al., 2006) and are proposed to result from the sub-liquidus mingling of two magmas with contrasting physical properties (Sparks and Marshall, 1986; Koyaguchi and Blake, 1991). Previous studies of mafic inclusions have focussed on their composition and their crystal textures (Coombs et al., 2006; Martin et al., 2006; Browne et al., 2006; Barclay et al., 2010), but here we focus on the role of the mafic magma in supplying volatiles to the host magma during rapid cooling, crystallisation and vesiculation. A number of studies have proposed mechanisms by which volatiles might be transferred from underplating mafic magmas. "Gas sparging" is the upward flow of a fluid from the mafic to silicic magma across the interface, advecting heat and thus "defrosting" the overlying silicic magma (Bachmann and Bergantz, 2006). It has been proposed that prior to the 1991 eruption of Pinatubo, oxidised mafic magmas intruded the dacite reservoir, carrying high concentrations of sulphur that exsolved during intrusion and cooling, feeding a pre-eruptive vapour phase in the dacite (Hattori, 1993; de Hoog et al., 2004).

Quantifying the mass fraction of volatiles in pre-eruptive magma (both dissolved and exsolved) is of great importance in terms of hazard assessment and interpreting geophysical data. However, it is far easier to quantify volatiles *dissolved* in magma prior to eruption (from melt inclusion data and phase equilibria) than it is to estimate the proportions of *exsolved* volatiles coexisting with magma, particularly when it is an open system that is likely to be receiving fluids (and recharging magmas) from greater depths in the crust. One way in which we might quantify the exsolved vapour fraction coexisting with magma at depth is to measure the flux of volatiles emitted as volcanic gases (representing the exsolved pre-eruptive volatile fraction and a component of the dissolved fraction) in excess of that measured in melt inclusions (the dissolved pre-eruptive volatile fraction), and hence calculate the mass of these species existing as vapour prior to eruption; and this is the approach we take in this paper,

using new constraints from the analysis of melt inclusions, volatiles in phenocrysts and volcanic gases. We firstly review our state of knowledge of the volatile budget of the Soufrière Hills Volcano and present new data on the CO_2 and H_2S flux of volcanic gases, melt inclusion geochemistry (including H_2O and CO_2 measured by Secondary Ion Mass Spectrometry), the H_2O content of nominally anhydrous phenocrysts (orthopyroxene) and a textural study of vesicle size distributions to assess the role that mafic magma plays in recharging fluids in magma storage areas prior to and during eruption. As well as establishing the volatile budget of the Soufrière Hills system, we explore the important role that volatiles play in eruption longevity and style, and their effects on other geophysical manifestations of volcanic activity such as ground deformation and seismicity. We elucidate magma transport, storage and plumbing, establish the likely fluid content of magma in the crust, the role of mafic magma in supplying replenishing volatiles in the system and further investigate the protracted nature of andesite petrogenesis in the arc crust. We make use of RhyoliteMelts (Gualda et al., 2012), a thermodynamic model optimised for H_2O-rich oxidised magmas, to simulate crystallisation and vesiculation of mafic magmas intruding into andesite.

2. Geological, petrological and geochemical setting

Magmas erupted at Soufrière Hills Volcano are andesitic in bulk composition, and have been remarkably consistent over the eruption (Murphy et al., 2000; Zellmer et al., 2003). The andesite is highly crystalline, containing 30-45 wt% phenocrysts and glass accounting for 5-25 vol% (Humphreys et al., 2009a). The phenocryst assemblage is 30-35 vol% plagioclase feldspar, 6-10 vol% hornblende, 2-5% orthopyroxene, 2-4% titanomagnetite and <0.5% quartz. Clinopyroxene (<0.5 vol%) occurs only as microphenocrysts, and apatite and ilmenite are also present in trace amounts. The groundmass mineral phases are similar but amphibole is absent. The andesite contains inclusions of more mafic magma, which show a range of bulk rock compositions, from basalt to andesite (Murphy et al., 2000; Humphreys et al., 2009a; Barclay et al., 2010; Plail et al., this volume; Humphreys et al., 2012), range in volume fraction from 1-12 vol% (Barclay et al., 2010; Plail et al., this volume) and exhibit a diverse range of textures, which has allowed several subtypes to be identified (Plail et al., this volume). Mafic inclusions are generally phenocryst-poor (<5 vol%), with plagioclase feldspar being the dominant framework phase, with amphibole and orthopyroxene (Murphy et al., 2000; Humphreys et al. 2009a; Plail et al., this volume). There is a significant proportion of "inherited" phenocrysts (plag + hbl + opx + qz), inferred to have been derived from the andesite host during mingling (Plail et al., this volume). The groundmass comprises plagioclase ± clinopyroxene ± orthopyroxene ± amphibole, titanomagnetite, and regions of

interstitial rhyolitic glass. As well as the macroscopic mafic inclusions, there is abundant evidence for mafic components in the andesite that have resulted from the disaggregation of inclusions, including anorthitic plagioclase microlites and crystal clots, which may account for as much as a further 6% of the volume of the andesite (Humphreys et al., 2009a; 2012). There is also abundant evidence for heating and disequilibrium, including sieve-textured plagioclase, reverse-zoned phenocrysts, thermal breakdown of hornblende and rounded quartz, all of which require close contact with intruding hot mafic magma (Barclay et al., 1998; Murphy et al., 2000; Humphreys et al., 2009a). Glass in the mafic inclusions is rhyolitic and similar in major element composition to that found within the andesite (Humphreys et al., 2010, Plail et al., this volume). Glass heterogeneity observed in the andesite is proposed to originate from mass transfer of melt from mafic inclusions and subsequent partial diffusive equilibration within the andesite, with small areas of rhyolitic glass in the andesite magma enriched in Ti and K (Humphreys et al., 2010). Temperatures range from 835-875 °C for the andesite host, and 1020 to >1100 °C for the mafic inclusions (Murphy et al., 2000; Humphreys et al., 2009a).

The macro- and microscopic petrological evidence clearly indicates extensive interaction between more mafic magmas and an andesitic magma. The timescale for at least the most recent of these interaction events has been constrained, using Fe-Ti oxide diffusion profiles, to be on the order of days to weeks (Devine et al., 2003), or shortly before eruption. Uranium series disequilibria suggest that the andesite body has resided at cool temperatures in the crust for 10^3-10^4 years, before being remobilized by hotter intruding melts (Zellmer *et al*., 2003). These timescales have led to a model of convective self-mixing and eruption of the andesite, triggered by mafic intrusion, in a shallow crustal magma chamber (Couch et al., 2001), a model which is not fully compatible with observations of substantial mass transfer between the two magmas (Humphreys et al., 2012). Observations of ground deformation likewise require magma supply from depth to explain long-term wide-field inflation during eruptive pauses (Elsworth et al., 2008; Mattioli et al., 2010). It is unclear, however, whether this magma supply represents an end-member mafic component, or an already hybrid magma that has formed at deeper levels in the crust. At this and other arc volcanoes, the emerging picture is one of small ephemeral magma storage regions distributed over a large vertical scale throughout the crust, with little evidence for a single large storage area in the upper crust (e.g. Mastin et al., 2009). Recent geophysical surveys of the arc crust beneath Montserrat have failed to image a large distinct magma chamber at depths of <6 km, but has indicated rather more diffuse zones of (>30%) melt beginning between 5.5 and 7.5 km depth (Paulatto et al., 2012), which may represent the upper reaches of a large vertical zone of magma storage.

The volatile budget of SHV has been constrained through studies of volcanic gases (Hammouya et al., 1998; Young et al., 1998; Edmonds et al., 2001; Watson et al., 2001; Oppenheimer et al., 2002; Edmonds et al., 2002; 2003a, b; 2010; Christopher et al., 2010; this work) and through melt inclusion volatile microanalysis (Barclay et al., 1998; Edmonds et al., 2001; Humphreys et al., 2009; this work). Melt inclusions in phenocrysts of quartz, orthopyroxene and plagioclase are rhyolitic, with 70-75 wt% SiO_2 (Barclay et al., 1998; Edmonds et al., 2001; Humphreys et al., 2009b; Humphreys et al., 2010). They contain up to 100 ppm sulphur (Edmonds et al., 2001), and up to 6000 ppm Cl and 450 ppm F (Edmonds et al., 2001; Humphreys et al., 2009b). The sulphur concentration in the rhyolitic glass is consistent with the solubility of sulphur as constrained by experiments on relatively oxidized rhyolitic melts (Clemente et al., 2004; Zajacz et al., 2012) and with studies of sulphur partitioning, which suggest that sulphur partitions strongly into vapour at upper crustal pressures, with fluid-melt partition coefficients of >50 for low temperature, oxidised silicic magmas (e.g. Scaillet et al., 1998). This partitioning of sulphur into vapour is the accepted explanation for the so-called "excess sulphur problem", that is to say the observation that far more sulphur is emitted in the form of volcanic gases during an eruption than can be explained by degassing of pre-eruptive melt (represented by melt inclusions) alone (see Wallace and Edmonds, 2011, for a review). The magnitude of the excess sulphur emitted by Soufrière Hills Volcano suggests that there is a substantial fluid phase present in the magma when it resides in the upper crust, which is likely to comprise H_2O and CO_2 as well as SO_2 and H_2S. The Cl concentrations measured in melt inclusions at Soufrière Hills are among the highest measured at any arc volcano (Edmonds et al., 2002; Humphreys et al., 2009b), and are very close to the solubility limit for this melt (Signorelli and Carroll, 2002). The petrological account of Cl degassing, as recorded in the difference between melt inclusions and matrix glass concentrations of Cl, scaled up to the erupted mass, is of the same order as the mass of HCl emitted as volcanic gas, suggesting that Cl largely degasses at much lower pressures than crystallisation and melt inclusion entrapment occurs, in tandem with H_2O (Edmonds et al., 2001; 2002; Oppenheimer et al., 2002; Villemant et al., 2008; Humphreys et al., 2009b). H_2O contents of Qz-hosted melt inclusions are up to 4.7 wt% whilst in plagioclase H_2O contents reach 6.3 wt% (Humphreys et al., 2009b) and we present further melt inclusion data in this paper. Equilibration pressures calculated using the quartz melt inclusion H_2O contents alone (incorporation of CO_2 will yield higher pressures) are 115-130 MPa (corresponding to a depth of approximately 5-6 km, assuming a magma density of 2500 kg/m^3). We add to the database of estimates for equilibration pressures in this paper, using both the H_2O and CO_2 contents of melt inclusions hosted by plagioclase and by orthopyroxene and we show here that this

pressure range can be extended substantially higher using hydrogen in nominally anhydrous phenocrysts.

Direct observations of large fluxes of volcanic gas at the surface during both dome building and explosive activity, which have ranged from 1 x 10^6 to >200 x 10^6 kg/day of SO_2, H_2S, HCl and CO_2 (Young et al., 1998; Watson et al., 2001; Edmonds et al., 2001; 2002; 2003a; 2010; Christopher et al., 2010; Carn and Prata, 2010; Christopher et al., this volume), show that volatiles are an important constituent by mass of the hybrid magma system. The volcanic gas flux remains high during eruptive pauses, showing that the segregation of vapour is not coupled to the eruption of andesite and that the gases originate from a deep source and follow permeable pathways to the surface, even when magma is not erupting (Edmonds et al., 2003b; Christopher et al., 2010). This observation, in combination with observations of inflation and seismicity, has been a key indicator that the eruption has merely paused as opposed to ceased during non-eruptive periods from 1995-2012. Another observation that has become very useful for hazard assessment is the molar HCl/SO_2 ratio in volcanic gases, which climbs rapidly to values >1 (it has reached values of around 10) at the onset of lava extrusion, from values <0.3 during pauses (Edmonds et al., 2002; Oppenheimer et al., 2002; Edmonds, 2008; Christopher et al., 2010). This change has been attributed to low pressure (probably < 50 MPa) degassing of water-rich andesite during ascent and eruption, which promotes Cl degassing (Edmonds et al., 2002). The flux of gaseous CO_2 from the volcano, which reached 3-5 x 10^6 kg/day during a short measurement campaign in 2008 (Edmonds et al., 2010) shows that CO_2 is a significant component of the volatile phase and is likely to play an important role in petrogenesis, magma ascent and eruptive dynamics (e.g. Papale and Polacci, 2009) yet has not been quantified in melt inclusions or considered in petrogenetic models to date, which we address in this paper.

3. Methods

3.1. Samples

The samples used in this study are lava dome blocks from pyroclastic flow deposits emplaced on 8th January 2007 in the Belham River Valley, and during January 2010 in Aymers and Whites Rivers, and pumice fall from the sequence of vulcanian explosions in July 13-15 2003 (**table 1**). The lava dome blocks emplaced on 8 January 2008 contained numerous mafic inclusions from centimetres up to a decimetre in dimension, which were of various shapes and vesicularities (Plail et al., this volume; **figure 1**). For the vesicle size distribution study, 13

thin sections were cut from the sampled lava dome blocks, which contained mafic inclusions. The sections were cut such that margins and interiors of the inclusions were well-represented, as well as host andesite proximal and distal (> 5 cm) from mafic inclusions. Two blocks from the mafic enclave BR10a were cut perpendicular to one another to examine textural anisotropy in the mafic magma. For the melt inclusion and phenocryst study, plagioclase and orthopyroxene phenocrysts were picked from crushed pumice samples and mounted in high vacuum-compatible epoxy resin and polished to expose melt inclusions. The melt inclusions commonly displayed at least one shrinkage bubble, but had not undergone significant post-entrapment crystallisation. Pyroxene phenocrysts were pushed into indium metal in an ion probe mount, ground to a flat surface and polished.

3.2. Glass and phenocryst microanalysis

Glass inclusions in plagioclase phenocrysts were analysed using Secondary Ion Microscopy at the NERC Ion Probe facility in Edinburgh and at the SIMS Lab, Carnegie Institution, Washington D.C. At the NERC facility a Cameca ims 4f ion microprobe was used, utilizing a 5nA O^- ion beam on a pre-rastered spot of 10 microns in size. Counts were collected over 10 cycles. H_2O contents were calculated from a daily working curve of H/Si vs. H_2O (Blundy and Cashman, 2005), which gives a straight line with R^2 0.97 or better (**figure 2**) for a set of well-characterised standard glasses, following the procedure described in Humphreys et al. (2006, 2009) and Blundy and Cashman (2005).

The abundance of H_2O in glass inclusions and in orthopyroxene was measured at the Carnegie Institution SIMS lab using a Cameca 6f ion probe and a Cs^+ beam. During the pre-analysis rastering of a 40 x 40 micron spot, secondary ion images of ^1H, ^{12}C and ^{35}Cl were projected on the channel plate, which helped to avoid inclusions and cracks, which appear as bright features on the projected image. The Cs^+ beam generates the negatively charged secondary ions $^1H^-$ and $^{30}Si^-$ (the internal standard) and we use a linear working curve (**figure 2**; Hauri et al., 2002). A linear calibration relating $^{12}C/Si$ to CO_2 concentration for rhyolites was used, which has been observed not to vary significantly in slope between analytical sessions (Hauri et al., 2002). Based on the standard deviation on repeat analyses of standard glasses, precision for H_2O and CO_2 measurements were better than 0.2 wt % and 150 ppm respectively. The H_2O and CO_2 concentrations of the standard glasses were within 5 % of accepted values. Calibration for sulphur, chlorine and fluorine is linear and based on analyses

of a range of rhyolitic standard glasses (details of standards are given in Hauri et al., 2002).

The abundance of H^+ in orthopyroxene was quantified using methods recently developed for the microanalysis of trace amounts of hydrogen (Koga et al., 2003). Pressure in the ion probe sample chamber was $<6 \times 10^{-10}$ Torr during all analyses. A primary beam 20 μm in diameter was rastered over a 50 μm x 50 μm area for 1 – 3 min prior to analysis. After each beam spot was carefully examined, the raster was stopped and a field aperture inserted to permit transmission of ions only from the central 8 μm of the 20 μm beam crater, thus avoiding transmission of hydrogen ions from the edge of the sputter crater and the surface of the sample. Counting times for ^{1}H and ^{30}Si were 5 and 10 s respectively. Detection limits for H_2O in orthopyroxene were typically 1–4 ppm H_2O, determined by the repeat analysis of synthetic H-free orthopyroxene. Well-populated calibration curves for synthetic orthopyroxene crystals (with OH^- and H_2O concentrations measured by FTIR; Koga et al., 2003) for H_2O were used (**figure 2c**; see Hauri et al., 2006 for further analytical details). Calibrations for H_2O were verified for glasses and minerals prior to each analytical session.

Nominally anhydrous minerals such as pyroxene and olivine can incorporate up to a few hundred ppm H_2O into their crystal structure and these minerals are important reservoirs for H_2O in the mantle (Hauri et al., 2006). Pyroxenes also crystallise from H_2O-rich melts in crustal magma reservoirs and are an important constituent of volcanic rocks. We may therefore expect pyroxene to take up H_2O if they grow at high enough pressures such that significant amounts of H_2O remain in the melt. It has been shown experimentally that the solubility of H_2O in orthopyroxene is dependent on the temperature, pressure, aluminium content and perhaps the concentrations of some other components (Rauch and Keppler, 2002; Stalder and Skogby, 2002; Stalder, 2004; Mierdel and Keppler, 2004). The partition coefficient describing the ratio between the concentration of H_2O in the orthopyroxene to the concentration in the melt is controlled primarily by the Al content of the pyroxene. The dominant mechanism of hydroxyl incorporation into pyroxene is solid solution of Mg-Tschermaks component, $MgAl_2SiO_6$ (Grant et al., 2007). In both dry and hydrous orthopyroxene (under H_2O-saturated conditions), the ratio between tetrahedral and octahedral Al is the same, which suggests that the dominant substitution mechanism for H in pyroxene is one or both of (Kohn et al., 2005):

354 $$MgAl^{[6]}Al^{[4]}SiO_6 + H_2O = H_2Al^{[6]}Al^{[4]}SiO_6 + MgO$$
$$MgAl^{[6]}Al^{[4]}SiO_6 + 2H_2O = MgAl^{[6]}Al^{[4]}H_4O_6 + SiO_2$$

355

356 In fact, incorporation of H^+ is accompanied by changes in the environment around both
357 tetrahedral and octahedral sites, suggesting that the hydrogen protonates oxygens which
358 bridge the tetrahedral and octahedral sites (Kohn et al., 2005). The solubility of H_2O in pure
359 enstatite has been observed to be dependent on temperature at mantle pressures, although the
360 temperature dependence becomes weak at low pressures (<1000 MPa; Mierdel and Keppler,
361 2004). At a pressure of 1000 MPa, the solubility of H_2O in pure (Al-free) enstatite was found
362 to be around 100 ppm (Rauch and Keppler, 2002; Mierdel and Keppler, 2004). One of the
363 strongest controls on water solubility is Al content of the pyroxene however, and merely
364 adding 1 wt% Al to enstatite triples the solubility of H_2O at 1500 MPa and 1100 °C (from 400
365 to 1200 ppm). It is proposed that this relationship can be extrapolated to both higher and
366 lower pressures (Rauch and Keppler, 2002), making the solubility for H_2O at pressures of
367 <1000 MPa on the order of a few hundred ppm H_2O. Partitioning of H_2O between melt and
368 orthopyroxene is most strongly controlled by the tetrahedral Al content of orthopyroxene
369 (Hauri et al., 2006), with $D_{H_2O}^{opx/melt}$ varying linearly from 0.003 for 1 wt% Al_2O_3, to 0.025 for 8
370 wt% Al_2O_3 (Hauri et al., 2006; Grant et al., 2007 and references therein). For this study, H_2O
371 in the orthopyroxene was measured using SIMS, and Al_2O_3 using EPMA in order to constrain
372 the most suitable partition coefficient with which to calculate melt H_2O contents in
373 equilibrium with the orthopyroxene along profiles from core to rim.
374
375 Mineral and glass major element and S, Cl and F compositions were analysed using a Cameca
376 SX-100 5-spectrometer electron microprobe at the University of Cambridge. Orthopyroxene
377 major element composition was analysed with a 15 kV, 10 nA beam focused to a 2 μm spot.
378 Glasses were analysed using a 15 μm, 15 kV beam with 2-4 nA beam current for major
379 elements and 10 nA beam for minor elements. Na and Si were analysed first with short
380 counting times in order to reduce migration of alkalis (following Devine et al. 1995; Blundy
381 and Cashman 2005; Humphreys et al. 2006).
382
383 *3.3. Image analysis and the theoretical basis for the textural study*
384
385 Backscatter images of the prepared thin sections of mafic inclusions and andesite host were
386 obtained using a JEOL JSM-820 Scanning Electron Microscope (SEM) operating at an
387 accelerating voltage of 20kV at Earth Sciences, Cambridge. Maps comprising 9 images were

used to acquire sufficient area for analysis. For image analysis of andesite, a magnification of x60 was used and for the mafic inclusions, x30 (owing to the differing vesicle number densities between the two sample types). Where thin sections contained the interface between the mafic and andesite magmas, areas were mapped immediately adjacent to the interface and also at a distance of > 1 cm from the interface. Where the thin section contained just one magma type, areas representative of the thin section were chosen. For all images abnormally large phenocrysts and vesicles were avoided. For the andesite samples, there were commonly crystals growing inside the vesicles (a result of vapour phase crystallization of probably cristobalite or feldspar). The SEM images were manually edited to eliminate these crystals from the vesicles. The software ImageJ was used to set a grey-scale range that isolated the vesicles. The minimum area of vesicle measured was set to 10 pixels to exclude small cracks in phenocrysts and vesicles. The area, perimeter, fit ellipse and centre point coordinates of each vesicle were recorded. The vesicle areas were converted to three dimensional volumes, which introduced some potential errors, derived from (1) the vesicle cross-sections being unlikely to represent the maximum diameter of the vesicle; and (2) larger vesicles being more likely to be intersected by the plane imaged and (3) the vesicles being modeled as spheres, which is not realistic for all samples. To account in part for these potential errors, a distribution of sphere sizes is assumed whereby the largest vesicle measured represents the maximum sphere diameter in the sample and a fraction of the next largest class is then assumed to be from sections across vesicles of the largest vesicle size and so on (Cashman et al., 1994).

Textural studies of the vesicles in volcanic products provide information on the conditions of bubble nucleation and growth in magmas (which usually requires quantifying a timescale for bubble growth independently), which may include quantifying decompression rates and mechanisms of magma fragmentation (Cashman and Mangan, 1994). The most commonly used visualisations are the vesicle volume distribution (VVD) and the vesicle size distribution (VSD). For a steady state open system, a vesiculation history involving discrete nucleation events may yield kinetic information via the population density function:

$$n = n_0 \exp\left(\frac{-L}{G\tau}\right) \qquad (1)$$

where n is the number density of bubbles of a given size per unit volume of melt, L is the equivalent bubble diameter, n_0 is the number density of nuclei, τ is the bubble residence time (estimated using independent textural information) and G is the mean growth rate of bubbles.

Equation 1 was originally used for crystal size distributions (e.g. Cashman and Marsh, 1988; Marsh, 1998) and has since been applied to vesicle populations (Klug and Cashman, 1994; Mangan et al., 1993). In practice it can be applied to linear VSDs where the slope is $-1/G\tau$ and the intercept is n_0.

The shape factor is used to determine the complexity of the shape of the vesicle. A circle has a shape factor of 1 and more complex shapes have shape factors tending towards zero. The shape factor SF is given by

$$SF = \frac{4\pi A}{p^2} \qquad (2)$$

where A is the area of the vesicle and p is the vesicle perimeter.

3.4. Volcanic gas ratios and flux measurements

Throughout the eruption, sulphur dioxide (SO_2) fluxes have been measured routinely using a variety of UV spectroscopic instruments: the COSPEC from 1995-2002 (Young et al., 1998; Watson et al., 2001; Edmonds et al., 2003a) and concomitantly and subsequently by Differential Optical Absorption Spectroscopy using a network of fixed UV spectrometers (Edmonds et al., 2003a; Christopher et al., 2010). Ground-based measurements of SO_2 have been supplemented by satellite-based measurements during large explosive events made by TOMS and subsequently by OMI and by AIRS and SEVIRI (Prata et al., 2007; Carn and Prata, 2010). Measurements of the other major volatile species in the volcanic plume (CO_2, H_2O and H_2S) have only been achieved in recent years, using a multi-component instrument package, Multi-GAS (Aiuppa et al., 2006; Shinohara et al., 2008; Edmonds et al., 2010).

The Multi-GAS system is a multi-component gas analyser system which enables a wide range of gas concentrations to be measured simultaneously, remotely, continuously and on the ground at distances up to several kilometres from a gas vent. The Multi-GAS system used in this study was assembled at the Instituto Nazionale di Geofisica e Vulcanologia (INGV), Sezione di Palermo and stored in a waterproof box powered by a wet 12V 40A/h battery. A Multi-GAS instrument package was deployed for one year at St George's Hill from April 2010 to March 2011 (when it was removed for servicing), following a short trial in July 2009 (Edmonds et al, 2010). The instrument package incorporates electrochemical sensors for SO_2 and for H_2S; and a LI-COR 840 non-dispersive infrared spectrometer for CO_2 and H_2O

458 concentrations. Samples of volcanic plume are fed into the sensor array using an on-board
459 pump (average flow rate of 0.98 l/m), with a filter system to eliminate ash particles. The
460 electrochemical cells produce an electrical current when the gas reacts with a wet membrane.
461 This current is detected on the input board and then converted into a voltage on the power
462 board. The LI-COR spectrometer outputs a voltage when the gas is detected. The voltages are
463 digitised by an analogue to digital signal converter on the micro-board and counts are
464 telemetered back to the volcano observatory, where they are converted into gas concentrations
465 using well-characterised calibration curves established in the laboratory. The gas
466 concentration is measured every second and the median value of 9 measurements is recorded
467 on the micro-board. Though the Multi-GAS can do this continuously, it was programmed to
468 take measurements every 4 hours, yielding 6 cycles a day, to conserve power. Each cycle
469 consists of 20 minutes during which the LI-840, pump and sensors power up and stabilise.
470 Then the Multi-GAS runs for 30 minutes, taking 200 measurements, and then turns off until
471 the next cycle. The raw data yield molar ratios between SO_2, H_2S and CO_2. When combined
472 with SO_2 fluxes measured using the Montserrat Volcano Observatory's DOAS network, CO_2
473 and H_2S fluxes can be calculated from the data. H_2O concentrations were generally too low
474 to be detectable above the considerable background H_2O concentrations.
475
476 Multi-GAS data have a digitisation error of ±0.24 ppm for CO_2 and < 5 ppb for SO_2 and H_2S.
477 The CO_2 sensor has cross sensitivity with H_2O (<1.0ppm CO_2/ppt H_2O) that leads to an error
478 of ±0.03ppm. H_2S has cross sensitivity with SO_2 of around 10%. However as the SO_2 values
479 measured were all very small (nearly all were <1 ppm) relative to H_2S (≈4-15ppm) this error
480 is insignificant. The error on gas fluxes also includes the 30% maximum error generated by
481 the DOAS processing (Edmonds et al., 2003a), due to uncertainties in plume speed and
482 height. The total error in the gas flux e_{tot} was determined from:
483
484 $$e_{tot} = \sqrt{\left(e_X\right)^2 + \left(e_{SO_2 flux}\right)^2} \qquad (3)$$
485
486 where $e_{SO_2 flux}$ is the error on the DOAS-derived SO_2 fluxes and e_X is the error on the molar
487 ratio of gas species measured by the Multi-GAS sensor and is given by:
488
489 $$e_X = \frac{\sigma_X}{\bar{X}} \qquad (4)$$
490

where σ_X is the standard deviation of the set of molar ratios measured during the course of a measurement period and X is the mean molar ratio, which yields a total error of 33% for CO_2 fluxes and 31% for H_2S fluxes (given errors on molar ratios of up to 14% for CO_2/SO_2 and 8% for H_2S/SO_2).

4. Results

4.1. Melt inclusion and orthopyroxene volatile concentrations

Melt inclusion volatile data (for 29 melt inclusions) are shown in **figure 3** and **table 2**. Water concentrations in the melt inclusions range continuously from 0.03 to 6.4 wt%, CO_2 from 0 to 1032 ppm, sulphur from 0 to 80 ppm and chlorine from 0 to 5335 ppm. The water, sulphur and chlorine data are similar in range to those published previously (**figure 3**; Barclay et al., 1998; Edmonds et al., 2001, 2002; Humphreys et al., 2009). CO_2 concentrations are higher than those measured in quartz melt inclusions using FTIR, which were below detection (Barclay et al., 1998). The combined H_2O and CO_2 data yield equilibration pressures ranging from 0 to 300 MPa (from VolatileCalc, Newman and Lowenstern, 2002; **figure 3**).

Sulphur concentrations are remarkably constant in melt inclusions with a H_2O content >1 wt%, with the bulk of the data falling between 17 and 30 ppm S. This trend is consistent with partitioning of sulphur between the melt and an exsolved vapour phase, with the exsolved vapour containing much of the mass of sulphur in the system (Scaillet and Pichavant, 2003). Concentrations of sulphur decline sharply at low H_2O concentrations (**figure 3**), indicating that sulphur degassing is enhanced at low pressures during magma decompression and degassing-induced crystallisation. Chlorine concentrations decrease gradually with the H_2O content of the melt inclusions down to around 2 wt%, and then more rapidly at low H_2O concentrations (**figure 3**). This pattern is consistent with previously published studies of the controls on halogen abundances, which suggest that chlorine melt concentrations are controlled by a combination of partitioning into vapour (with complex changes in partition coefficient related to pressure and melt composition; e.g. Shinohara et al., 1989) and crystallisation (Edmonds et al., 2002; Humphreys et al., 2009). The rapid decrease in Cl concentrations at low H_2O concentrations (**figure 3**) suggest that much of the Cl exsolves from the melt at low pressures, due to enhanced partitioning into vapour. This is consistent with observations of the flux of HCl gas, which increases rapidly during periods of magma decompression and eruption (Edmonds et al., 2008; Christopher et al., 2010) and with experiments (Lesne et al., 2011). Fluorine concentrations range from 23 to 327 ppm (**figure**

527 **3**), with a mean of 119 ppm. Similar to the Cl dataset, the most degassed inclusions with
528 respect to H_2O also display low F concentrations, suggesting that some degassing of fluorine
529 is taking place at low pressures, although the magnitude of the decrease (60-80 ppm) is not as
530 large as for Cl and this is consistent with the low fluxes of gaseous HF measured from the
531 volcano in the past (Edmonds et al., 2002).
532
533 The H_2O concentration across the orthopyroxene crystals ranged from 110 to 230 ppm, with
534 an average value of 159 ppm for a population of 176 spot analyses (**Table 3; figure 4**). These
535 water concentrations are well below the solubility for water in pyroxene at these pressures and
536 Al_2O_3 contents (~ 300 ppm H_2O; Rauch and Keppler, 2002).
537
538 *4.2. Mafic inclusion vesicle size and shape distributions*
539
540 The mafic inclusions can be divided into glassy and crystalline types (**figure 5; table 4**; Plail
541 et al. this volume). The smaller enclaves (<3 cm in diameter) are generally glassy and have
542 20-40 vol% glass, with rounded vesicles, sometimes forming vesicle trains in brown glass
543 pools (**figure 5**). The larger inclusions (>5 cm in size) are more crystalline with diktytaxitic
544 textures, generating more angular and irregular vesicles with complex shapes controlled by
545 crystal morphology (**figure 5**). The margins of the crystalline enclaves are usually glassy
546 however, with vesicles more similar in appearance to those of the entirely glassy enclaves.
547
548 Volume distributions of vesicles contain a single, discrete peak at low equivalent diameter
549 (**figure 6a, left**). Size distributions of vesicles show a negative linear relationship between
550 ln(n) and vesicle diameter, indicating a single event of bubble nucleation and growth, with
551 minor bubble coalescence (**figure 6a, right**). Crystalline enclaves have vesicle distributions
552 that are distinct from those of the glassy enclaves: volume distributions have a single peak at
553 low equivalent diameters but then a steady increase in volume fraction with equivalent
554 diameter after a minimum at around 0.3-0.4 mm (**figure 6b, left**). The size distributions
555 define a concave-upwards curve, approximating a negative linear relationship at equivalent
556 vesicle diameters <0.3 mm (**figure 6b, right**). The distributions suggest a single bubble
557 nucleation and growth event, followed by a significant degree of bubble coalescence. We
558 propose that the bubble nucleation event occurred during intrusion into the cooler andesite,
559 which caused rapid quenching, crystallisation and vesiculation. This is supported by the
560 intimate relationship between the crystal framework and the vesicle population, which
561 suggests the two formed concurrently, similar to the textures observed in mafic inclusions
562 elsewhere (Martin et al., 2006). The slope of the curve for the size distributions (which is

563 proportional to $1/G\tau$) are similar for both the glassy and crystalline types, suggesting that both
564 timescales for vesiculation and bubble growth rates were similar. The distributions for
565 BR10aa and BR10ab (cut perpendicular to each other) are similar, implying, at least for this
566 sample, that the three-dimensional vesicle structure is isotropic. Isotropy is borne out by
567 micro- and macroscopic inspection of the mafic inclusions.
568

569 Vesicles in the host andesite are smaller and more irregular in shape than those in the mafic
570 enclaves (**table 4**). Andesite volume distributions comprise a single peak at around 20 μm
571 (**figure 6c, left**). After this initial peak some distributions, typically those adjacent to
572 enclaves, have sparse high volume vesicles at high equivalent diameters. Size distributions
573 give a well-constrained linear trend at low equivalent diameters and more scattered points
574 curving upwards at higher equivalent diameters (**Figure 6c, right**). Both distributions suggest
575 that the andesite underwent a single episode of bubble nucleation and growth, most likely due
576 to magma decompression and volatile exsolution, which is consistent with the higher bubble
577 number densities at smaller vesicle sizes (Mangan and Sisson, 2000). The steeper slope of the
578 size distribution (which is proportional to $1/G\tau$) compared to the mafic inclusions, suggests
579 that bubble growth rates were much lower in the andesite, consistent with slow magma
580 decompression. The larger vesicles near to the mafic inclusion interfaces may be related to
581 volatile transfer from the mafic magma.

582 Porosities are generally higher for the crystalline inclusions (17-25%, with a mean of 21%)
583 than for the glassy inclusions (11-19%, with a mean of 14%; **table 4**). Although vesicle
584 distributions are similar for the andesite host and the andesite adjacent to enclave, the porosity
585 of the andesite close to the mafic interfaces (<5 cm) is notably less (12-18%, with a mean of
586 14%) than the porosity at a distance from the interface (9-26%, with a mean of 20%; **table 4**),
587 despite having larger vesicles. The lowest vesicle number densities occur at the centre of both
588 types of mafic enclaves, implying a slower cooling rate for the enclave interiors. Shape factor
589 distributions for the mafic inclusions and for the andesite host have a peak between 0.2 and
590 0.5, suggesting largely irregular vesicle shapes (**table 4**). For comparison, shape factor
591 distributions for a Vulcanian bomb and pumice have peaks above 0.6 (**Table 4**), indicating
592 more rounded vesicles. The glassy mafic enclaves have slightly lower modal shape factors
593 (**table 4)** and hence more complex shapes than the vesicles in the crystalline inclusions.
594

595 *4.3. Volcanic gas ratios and fluxes*
596

The plume was detected by the Multi-GAS system 30 times during the measurement period and it was possible to extract the H_2S flux for 19 cycles and the CO_2 flux for 17 cycles. H_2S/SO_2 varied between 0.3 and 2.6 and CO_2/SO_2 varied from 1.0 to 15.1 with averages of 1.3 and 6.7 respectively (**figure 7**; **table 5**). This range encompasses that observed previously during a 1 week period in July 2009 (Edmonds et al., 2010). There is no systematic variation of the two ratios. The fluxes of H_2S and CO_2 were calculated by multiplying the molar ratio by the daily SO_2 flux recorded by DOAS (MVO data). The H_2S and CO_2 fluxes during this period were 106-1051 x 10^3 kg/day and 308-5494 x 10^3 kg/d respectively and averaged at 434 x 10^3 kg/d and 2297 x 10^3 kg/d. These fluxes are higher than those measured previously (Edmonds et al., 2010) and perhaps, for H_2S, for any arc volcano globally. The SO_2 fluxes measured in this study ranged from 107 to 1153 x10^3 kg/d with an average of 295 x 10^3 kg/d, which is below the long-term eruption average of 600 x 10^3 kg/d (Christopher et al., 2010).

The molar ratios CO_2/SO_2 and SO_2/H_2S measured with time by the Multi-GAS sensor are shown in **figure 7a**, and the fluxes of SO_2, CO_2 and H_2S, measured using the DOAS network for the SO_2 flux, and Multi-GAS sensors for CO_2 and H_2S, are shown in **figure 7b**. We estimate that over the course of the 1995-2011 eruption, Soufrière Hills Volcano has now emitted 4.0 +/- 0.6 x 10^9 kg sulphur. The total cumulative mass of sulphur gases emitted during the eruption 1995-2011 is shown in **figure 8**, updated from Christopher et al. (2010) and using the H_2S fluxes measured by the Multi-GAS sensor during 2010 and 2011. During this same period, a total volume of ~1 km^3 magma has been erupted (Wadge et al., 2010; this volume; **figure 8**).

5. Discussion

5.1. Pre-eruptive dissolved volatiles, from melt inclusion and orthopyroxene data

The melt inclusion H_2O-CO_2 data do not fall on a simple closed system degassing trend, as might be expected. The melt inclusions are poor in CO_2 (<50 ppm) for melt inclusions with H_2O <0.3 wt%, and range from 0 to 1032 ppm for melt inclusions with 3.2-6.4 wt% H_2O (**figure 3**). Saturation pressures range from 100-300 MPa for this latter group (**figure 3**). The CO_2 content is generally higher than that measured in quartz melt inclusions (Barclay et al., 1998), and we ascribe this to higher pressures of entrapment in a vertically-elongated magma reservoir. We ascribe the high CO_2 contents of some melt inclusions with the higher H_2O contents, to the equilibration of melts with a deep-derived CO_2-rich vapour phase that is migrating upward through the magma body, similar to that proposed for Mount St Helens

(Blundy et al., 2010) and Soufriere Hills from hornblende zoning profiles (Humphreys et al., 2009) and more commonly, for basaltic systems (Metrich and Wallace, 2008). Over time, as the shallow chamber is flushed by CO_2-rich vapour, the melts become dehydrated and enriched in CO_2, subject to kinetic constraints imposed by the arrangement of permeable gas pathways and the time frame for gas flushing (Yoshimura et al., 2011). A range of H_2O and CO_2 contents can be produced by a fixed composition of the flushing vapour and a diffusion-limited process (Yoshimura et al., 2011); or the flushing volatile phase may be variable in terms of composition. Trace element (Edmonds et al., 2001) and major element (Humphreys et al., 2010) melt inclusion compositions do not support magma mixing as a possible explanation for the trend. The relatively slow diffusion rate for CO_2 compared to H_2O raises the possibility that the melt inclusions are enriched in CO_2 due to a boundary layer effect during rapid crystal growth (e.g Baker et al., 2008). The diffusion rate for CO_2 in rhyolitic melts is similar to that for sulphur (e.g. Baker, 2008). Sulphur concentrations in the melt inclusions do not show heterogeneous enrichments, and instead are approximately constant for the melt inclusions with a H_2O content above 1 wt% (apart from two high values; **figure 3**), and we therefore reject diffusive pile-up as a mechanism for causing CO_2 enrichment in melt inclusions.

The water concentrations measured in the orthopyroxene phenocrysts may be used to estimate melt H_2O concentrations if the opx-melt partition coefficient for H_2O is known. Using an empirical calibration derived from published partition coefficients (**figure 9**) and the measured Al_2O_3 concentration in the orthopyroxenes (**table 3**), we calculate a range in $D_{H_2O}^{opx-melt}$ of 1.3 x 10^{-3} to 3.6 x 10^{-3}. Melt water concentrations calculated using the pyroxene water concentration data are shown in **figures 10 and 11**. The orthopyroxene record melt water concentrations ranging between 4.5 and 10.9 wt% H_2O, with an average value of 7.9 wt% (**figure 11**). Errors are calculated from the range in slopes of the linear regressions it is possible to fit through the calibration data in **figure 9** with an R^2 value of better than 0.6 which, when propagated into the melt H_2O calculation, leads to an average error of +/-11% in accuracy; precision is significantly better. In the crystal interiors, the melt water concentration in equilibrium with this portion of the crystal often varies by up to 2.0 wt% over 100-300 μm (**figure 10**); this magnitude of change in H_2O concentration is well outside analytical error and is likely to be due to real changes in the melt H_2O concentration. To increase melt H_2O concentration at saturation by this amount it would be necessary to increase the magmastatic pressure by around 100 MPa. To reduce melt water concentration by this amount would be more straightforward, and can be achieved by either decompression of around 100 MPa, by isobaric flushing by CO_2-rich gas, or by melt heating. It has been shown that for rhyolite

669 melts there is a negative dependence of solubility on temperature, such that raising the
670 temperature from 850 to 1000 °C at a pressure of 100 MPa reduces the solubility of H_2O by
671 up to 0.5 wt% and will cause H_2O exsolution (Yamashita, 1999). For higher pressures, it is
672 likely that the magnitude of the decrease in solubility will be greater. However, heating also
673 decreases the solubility of CO_2 (Fogel and Rutherford, 1990), yet the melt inclusions with
674 3.0-6.2 wt% H_2O show elevated CO_2 compared to the rest of the population (**figure 5c**). It
675 seems likely therefore that depletions in H_2O concentration of up to 2.0 wt% observed in the
676 interiors of the pyroxene crystals are due to episodes of CO_2-rich gas flushing, which act to
677 decrease melt H_2O concentration and enhance melt CO_2 concentrations. This is consistent
678 with the melt inclusion data (**figure 5c**) and previously published data on Cl and other
679 element zoning in amphibole, which has been interpreted to be the result of gas flushing
680 (Humphreys et al., 2009). The profiles often show depletions in H_2O concentration near to the
681 edges of the crystal (**figure 11b**). Depletions in H_2O content at the crystal rims might be
682 caused by rapid diffusive loss of water during magma decompression and degassing during
683 eruption; alternatively they could be due to heating and/or gas flushing related to mafic
684 magma intrusion shortly before eruption. Changes in H_2O concentration at the rim of the
685 crystal might also be affected by morphological effects.
686
687 Melt H_2O concentrations in melt inclusions, and that calculated from H_2O in orthopyroxene,
688 have distinct but slightly overlapping ranges (**figure 11**). Melt H_2O concentrations calculated
689 from the pyroxenes show a unimodal distribution, in contrast to the melt inclusions, which
690 have a much broader distribution. We propose that these two datasets are complementary,
691 each reflecting different processes within the volcanic system. The melt inclusions have been
692 sealed off from the carrier melts at a range of pressures during storage and transport (as
693 suggested for Mount St Helens melt inclusions by Blundy and Cashman, 2005). The
694 distribution of saturation pressures is even broader when the CO_2 content of the melt
695 inclusions is taken into account, as the high H_2O melt inclusions are also those with the
696 highest CO_2 contents (**figure 3**). The CO_2-rich melt inclusions were sealed off at a higher
697 pressure where melts were being flushed with CO_2-rich vapour, in a zone with high
698 advection/diffusion ratios. The pyroxene data, on the other hand, record a very narrow set of
699 storage conditions, which reflects prolonged residence prior to eruption in a magma storage
700 reservoir in the mid-upper crust. The magma was then transported rapidly enough to the
701 surface to prevent diffusive loss of H^+ from the interior of the crystal. A long storage time at
702 mid-upper crustal pressures is consistent with the phenocrysts' morphology: they are large
703 and euhedral with thin overgrowth rims of a few microns. Saturation pressures calculated
704 from melt H_2O derived from orthopyroxene composition range from 130 to 370 MPa, with an

average of 260 MPa, which is approximately equivalent to a depth of 10 km, with a range of 5-14 km, using a mean density of 2700 kg/m^3. These saturation pressures will be underestimates for these pressure conditions because there is no record of melt CO_2 contents in the pyroxene. It has been proposed, based on ground deformation data, that two storage reservoirs exist beneath Soufrière Hills, one centred at 5 km and one at 17 km (Elsworth et al., 2008; Foroozan et al., 2010). It is possible that the orthopyroxenes grew in this deeper reservoir, whilst most of the melt inclusions equilibrated during magma storage in the upper reservoir and during transport to the surface. It is also possible that the plagioclase grow at lower pressures, therefore trapping melts poorer in volatiles.

5.2. The amount and composition of exsolved volatiles (vapour) in the magma reservoir

The total amount of volcanic gases discharged over the course of the eruption (Christopher et al., 2010), combined with estimates of the total mass of lava erupted (Wadge et al., 2010) can be used in tandem to calculate the likely mass and composition of vapour coexisting with magma prior to eruption. Between July 1995 and July 2011, 4.0 +/- 0.6 x 10^9 kg S gases (SO_2 and H_2S) were emitted. Over the same time period, around 1.1 km^3 magma comprising ~50 vol% phenocrysts was also erupted (Sparks et al., 1998; Wadge et al., 2010; **figure 8**). The lava was erupted discontinuously (in five episodes; **figure 8**; Wadge et al., 2010, this volume) whereas the gas emissions were continuous over months to years timescales (**figure 8**; Edmonds et al., 2010; Christopher et al., 2010).

Melt inclusion data show that there is very little sulphur in melt inclusions (<100 ppm; Edmonds et al., 2001; **figure 3**) and therefore we assume that all of the sulphur emitted resides in a vapour phase in the pre-eruptive magma reservoir (or system of reservoirs). Melt inclusion data for H_2O and CO_2 concentrations and water concentrations in orthopyroxenes (**figure 11**) suggest equilibration pressures of 100-300 MPa and that the inclusions containing high concentrations of CO_2 were in equilibrium with a vapour containing at least 25-50 mol% CO_2 (**figure 3**). Using this information, as well as the mean molar C/S ratio in volcanic gases from the Multi-GAS data (5.0; **figure 7**) and the total mass of sulphur degassed up to July 2011 (4 x 10^9 kg), we calculate the composition and mass of fluid coexisting with the magma in the reservoir. If we assume a pre-eruptive vapour with 50 mol% H_2O and a molar C/S of 5, then we might expect a total mass of 4.3 x 10^{10} kg vapour emitted up to July 2011 (made up of 4.0 x 10^9 kg S, 1.1 x 10^{10} kg H_2O and 2.8 x 10^{10} kg CO_2). These estimates yield a total exsolved vapour of ~1.6 wt% in the bulk magma (which had a total volume of 1.1 km^3, with a density of 2500 kgm^{-3}) prior to eruption. Using a vapour with 75 mol% H_2O and a molar C/S

of 5, these estimates become 6.5 x 10^{10} kg vapour in total (made up of 4.0 x 10^{9} kg S, 3.4 x 10^{10} kg H_2O and 2.8 x 10^{10} kg CO_2). This gas assemblage leads to much higher proportion of exsolved gas, ~2.4 wt%.

The magma storage area may be zoned with respect to exsolved vapour, such that the top of the reservoir falls towards the larger end of this estimate and the base towards the lower end, leading to a total volatile content of around 6.5-9.6 wt% (exsolved plus dissolved volatiles). The volume fraction of such a vapour in the magma depends on the pressure at which the magma is stored, shown in **figure 12** (calculated using the ideal gas law). Melt inclusion H_2O-CO_2 systematics indicate equilibration pressures of between 100 and 300 MPa for the magma reservoir (**figure 12**); we would expect the vapour to occupy ~4.3 to 8.2 vol% at 300 MPa and 12.8 to 25.5 vol% at 100 MPa (**figure 12**). This vapour phase is, however, compressible, and so changes in magma chamber overpressure will change the volume fraction of vapour, by either compression or expansion, and perhaps by inducing dissolution or exsolution also, as the magma is saturated with respect to these volatile species. The vapour phase will therefore act to buffer the magma chamber volume during eruption (and reduction in overpressure) and during recharge (and increase in overpressure). The effects of such a vapour phase have already been observed at Soufrière Hills Volcano. After a lava dome collapse in July 2003, borehole strain-meters recorded a rapid pressurisation of a magma reservoir, attributed to the growth of 1-3 vol% bubbles in response to the unloading of the lava dome, with the resulting decompression being transmitted to depth and causing volatile expansion and exsolution (Voight et al., 2006). The implications of a significant exsolved vapour phase on eruption duration and magnitude, and for the interpretation of volcano monitoring data, are discussed further in a later section.

The uncertainties involved in our estimate for the mass of a pre-eruptive vapour phase stem both from the errors on the measurements themselves, but also from the fact that we are assuming that the magma and the vapour emitted during the eruption coexisted together in a non-stratified magma chamber, such that using their masses in tandem gives us a meaningful mean vapour content for the magma at pressures of 100-300 MPa. If the magma reservoir were stratified with respect to vapour, we might expect much of the gas emission to have been concentrated near the beginning of the eruption, with the gas/magma ratio decreasing with time. We have seen no such pattern, and in fact the eruption has been remarkable in the steadiness of the gas emissions. We are therefore content to assume that the mass balance argument is a meaningful one and the estimates we have made for the pre-eruptive vapour content of the magma are valid.

5.3. The source of exsolved vapour in complex hybrid magmas

We propose that the vapour in equilibrium and erupted with the andesite magma is recharged by intruding mafic magma that is rich in volatiles. We suggest that the mechanisms by which this occurs are by a) vesiculation and entrainment of bubbles from the mafic magma interface into the andesite and b) mafic inclusion formation and flotation at the interface, followed by auto-fragmentation or disaggregation and release of volatiles into the andesite during decompression.

The vesicle textures and petrology of the mafic inclusions in the andesite are clearly the result of a complex pressure-temperature-time path, which begins with decompression during ascent from the lower-mid crust, during which the melt falls below its liquidus temperature. The mafic inclusion petrology, dominantly a network of acicular pargasitic hornblende and plagioclase, with minor microphenocrysts of pyroxene, is distinct from the host andesite and is strongly suggestive of rapid cooling. The amphibole-rich nature of most of the mafic inclusions (Plail et al., this volume; Humphreys et al., 2012) also indicates genesis by rapid isobaric cooling. Such extensive amphibole crystallisation is unlikely to occur during decompression, owing to the shape of the amphibole stability curve, which is sub-parallel to typical decompression magma pathways (Carmichael, 2002; Davidson et al., 2007). Qualitative comparison of crystal sizes and volume fractions with experimental studies suggest that the enclaves experienced cooling rates of up to 2ºC/hour, and total cooling times of as little as 80 hours (Coombs et al., 2006). This short time frame is consistent with those derived from Ti diffusion profiles in Fe-Ti oxides, which suggest that the andesite was heated by invading mafic magma days to weeks before eruption (Devine et al., 2003). Other petrological features of the enclaves are consistent with rapid isobaric cooling: some mafic inclusions have glassy rims and they are generally rounded in shape.

The petrology and textures observed in the mafic inclusions are consistent with crystallisation driving vesiculation on interaction with the cooler andesite, similar to textures observed at Nea Kameni (Martin et al., 2006), Lassen Peak (Clynne, 1999), Mount St Helens, Mt Mazama and Trident Volcano, Alaska (Thomas and Tait, 1997; Coombs et al., 2006). Extensive crystallisation at the interface between the two magmas, the mafic magma (of basaltic to basaltic andesite composition) at a temperature of ~1020 to > 1100 ºC (Murphy et al., 2000; Humphreys et al., 2009) and the andesite at a temperature of ~835-875ºC (Murphy et al., 2000; Humphreys et al., 2009), drives the volatile concentration in the remaining melt

to saturation, thus causing exsolution and vesiculation. The size of the enclaves, ranging from sub-centimetre to decimetre, is similar to mafic inclusions in arc volcanic rocks elsewhere, and is consistent with the size expected as a result of instabilities developing in a thin foam at the interface between the underlying vesiculating mafic layer and the overlying silicic magma (Thomas and Tait, 1997).

The RhyoliteMelts algorithm (Ghiorso and Sacks, 1995; Gualda et al., 2012) was used to simulate the equilibrium crystallisation and vesiculation of the mafic melt against the cooler andesite, in an attempt to reproduce the textural observations presented here. An anhydrous basaltic andesite bulk composition (from Murphy et al., 2000) was used for the simulations, and a temperature drop from 1200 °C to 600 °C over a range of pressures from 300 to 100 MPa. Oxygen fugacity was fixed at one log unit above the NNO buffer (Humphreys et al. 2009a). The starting volatile content was allowed to vary between 0 and 10 wt% H_2O. The phases produced on cooling in the simulations were hornblende (in the more H_2O-rich simulations) and plagioclase feldspar, or pyroxene (ortho- and clino-) and plagioclase feldspar. For the H_2O-saturated simulations at all pressures there were significant proportions of liquid remaining after cooling to around 835 °C (up to ~55 wt%; **figure 13a**), which indicates that the interiors of the mafic inclusions were likely still liquid after entrainment. The maximum melt fraction in the glassy mafic inclusions (which contain amphibole) is around 40 vol%, consistent with quenching at 200-300 MPa (**figure 13a**). The effect of adding CO_2 to the system would be to decrease the activity of H_2O in the melt and enhance H_2O degassing, which would decrease the fraction of liquid remaining; our estimates of H_2O content are therefore a minimum.

It is likely that both the crystal and vesicle textures have been overprinted to some degree by degassing and crystallisation occurring during magma decompression, as was also proposed for the Trident Volcano (AK, USA) mafic inclusions by Coombs et al. (2006), based on both textural and compositional evidence. The most volatile-rich compositions were vapour-saturated prior to cooling; as the H_2O content decreased, vesiculation began during crystallisation. For the most H_2O-depleted compositions at the highest pressures, the melts remained undersaturated throughout cooling and crystallisation. **Figure 13b** shows the proportions of dissolved and exsolved H_2O in the system during cooling for the simulations performed at 300 MPa.

Upon cooling, crystallisation and vesiculation modify the bulk density of the magma (**Figure 14**). The change in density depends on the total amount of H_2O present in the system, the

pressure and the crystallising phases. The effect of increasing the total amount of H_2O in the system is to decrease the magma bulk density across the entire range of temperatures (**Figure 14**). The temperature region of interest is highlighted by a box in **Figure 14**. The bulk density of the andesite magma, with a total H_2O content of 10 wt% (dissolved plus exsolved H_2O), is shown by the small grey rectangle labeled "and". The change in bulk density yields potential for the flotation of mafic inclusions into the andesite. For the quenching simulations at 200-300 MPa, it is clear that the incoming mafic magma requires a total H_2O content of at least 6 wt% in order to achieve a similar or lower bulk density than the andesite and cause inclusion flotation. For all pressures, if the mafic magma has 8 wt% or more H_2O, then it will be saturated (and therefore bubble-bearing) when it is intruded into the cooler andesite. This is consistent with the observations of rounded vesicles in pools of clear glass in the glassy mafic inclusions (**Figure 5**; i.e. the bubbles did not nucleate heterogeneously on crystals). If the mafic magma were rich in CO_2 as well as H_2O then the required density for enclave flotation would be met at a much lower H_2O content.

We calculate the expected equilibrium porosity development during the quenching simulations (**figure 15**). The range in porosities observed in the mafic inclusions (shown by rectangles in **figure 15; table 4**) are consistent with total H_2O contents of >6 wt% H_2O for 300 MPa quenching and >4 wt% H_2O at 200 MPa, or >2 wt% H_2O at 100 MPa. It seems likely, comparing the density and porosity results, that if the quenching does occur at 100-200 MPa, then some of the original porosity on quenching must have been lost due to permeable vapour flow into the andesite, consistent with the observation of large vesicles close to the mafic inclusion interfaces. If the quenching takes place at 300 MPa, there is no need to invoke vapour loss from the inclusions; the density and porosity data are both consistent with the mafic magma having a H_2O content of at least 6 wt%, although vapour loss is not precluded and indeed is likely, particularly for the crystalline mafic inclusions which show evidence of significant bubble coalescence (**figure 6**). In fact, if CO_2 is added to the simulated system, porosities at all temperatures will increase markedly, which would mean that substantial vapour loss had occurred from all enclaves examined in this study.

Further constraints on mafic magma H_2O content are provided by the petrology of the amphiboles contained within the mafic inclusions, which are Al-rich (12-14.5 wt% Al_2O_3; Murphy et al., 2000) and are classified as magnesio-hastingsites (Murphy et al., 2000). The compositions of the amphibole yield a f_{O_2} relative to the NNO buffer of +1 and a H_2O

content of 7.0-9.5 wt% H_2O using the parameterisation of Ridolfi and Renzulli (2006; **Table 6**), which is entirely consistent with our thermodynamic quenching simulations and textural observations. The pressure and temperature from the parameterisation however, are up to 990 °C and 670 MPa, which would require that the framework amphibole formed deep in the crust. This seems questionable given that the enclaves incorporate andesite-derived phenocrysts that crystallised at much lower pressure, raising a question as to the applicability of this hygrometer for enclave mineralogy.

The results of the RhyoliteMelts simulations suggest that the mafic magma is H_2O-rich (with at least 6 wt% and probably >8 wt% total H_2O) and further, does not quench completely upon interaction with the cooler andesite; up to 30 or 40 wt% melt will remain in the interiors of the larger inclusions in particular. This melt will allow further vapour expansion and degassing during subsequent magma decompression and eruption whilst the inclusion is incorporated in the andesite magma. Decompression of the mafic inclusions, from 200-300 MPa to the surface, for a magma containing a total of >8 wt% H_2O, would result in the porosity increasing by several hundred times, which could not be contained within the quenched glassy margins of the mafic inclusions. The crystalline enclaves show clear evidence for vesicle coalescence. If permeability could not develop quickly enough for gas loss from the mafic inclusions to occur, and this appears to be the case owing to the lack of highly vesicular mafic inclusions surviving in the andesite, then this rapid expansion during decompression would inevitably result in the ductile auto-fragmentation of the mafic inclusions, thereby scattering the crystal and vapour contents into the andesite. This is a feasible and efficient means of mixing the two magmas and would explain very well the observations of mafic magma-derived crystals mixed homogeneously in the andesite (Seaman and Chapman, 2008; Humphreys et al., 2012), and would provide a mechanism for the efficient transfer of vapour from the mafic to the andesite magma, thus accounting for observations of gas fluxes at the surface (Edmonds et al., 2003; Christopher et al., 2010) and providing a mechanism for exsolved vapour to be "topped up" in the magma storage reservoir. Diffusive loss of H^+ might also occur during magma decompression, but this will only occur if the more mafic melt becomes oversaturated and may be most important for the small glassy inclusions, where porosity is limited and melt fraction is low.

5.4. Implications of exsolved vapour coexisting with magma prior to eruption

We have calculated, in a previous section, that the mass proportion of exsolved volatiles in the andesite magma reservoir prior to eruption might be as high as 1.6-2.4 wt% (in addition to the ~3.0-6.0 wt% H_2O and ~0-1000 ppm CO_2 dissolved in the melt), and of this exsolved vapour phase, 25-50 mol% may be CO_2. We have calculated this by: (1) using the mass of sulphur emitted as volcanic gases (**figure 8**) and (2) assuming that all of this sulphur resided in a pre-eruptive exsolved vapour phase, (3) calculating the amount of CO_2 coexisting with it from the C/S ratio of emitted gases measured using the Multi-GAS (**figure 7**) and (3) calculating the H_2O content of the vapour phase using the H_2O/CO_2 molar ratio of the gas phase in equilibrium with melt inclusions (**figure 3**) (from a chemical solution model Volatilecalc, Newman and Lowenstern, 2002). Using the pressure ranges acquired from the water content of melt inclusions (**figure 3**), we can define a magma storage area between 100 and 300 MPa. We find that for these range of conditions, the exsolved vapour occupies a volume fraction of approximately 4.3 to 25 vol%, depending on the pressure and the composition of the vapour (**figure 12**). It is likely that the magma reservoir is stratified with respect to exsolved vapour, with magma at the top of the magma reservoir having an exsolved vapour content of near to 13-25 vol%.

The presence of exsolved vapour has important implications for the bulk modulus of magma and hence its compressibility. For magma containing exsolved vapour, when the system is compressed, the gas volume changes by a much larger fraction than the magma volume. However, the gas volume is much smaller than the magma volume, so the total change in volume depends strongly on the amount of exsolved vapour present. We have calculated the effective bulk modulus β for magma containing exsolved vapour using (from Huppert and Woods, 2002):

$$\frac{1}{\beta} = \frac{1}{\beta_r} + \frac{1}{\rho}\left[-\frac{nP}{RT} - (1-n)\left(\frac{x}{\rho_c} + \frac{(1-x)}{\rho_m} \right) \right]^{-2} \qquad (5)$$

where β_r is the bulk modulus for vapour-undersaturated, or volatile-free magma, which is around 10 GPa (Tait et al., 1989), n is the total mass fraction of volatiles, x is the mass fraction of crystals in the magma, R is the universal gas constant (with a value of 8.314 $Jmol^{-1}K^{-1}$), T is the temperature (in Kelvin), P is the pressure (in Pa), ρ_c is the bulk density of the crystal assemblage, ρ_m is the melt density and ρ_{bulk} is the bulk magma density, calculated using:

$$\rho_{bulk} = \left[\frac{N}{\rho_{vap}} + (1-N)\left(\frac{\varphi}{\rho_c} + \frac{(1-\varphi)}{\rho_m} \right) \right]^{-1} \quad (6)$$

where ρ_{vap} is the vapour density, φ is the crystal fraction (taken as 0.5). Using a total volatile mass fraction of 0.096 to 0.065 (as estimated in an earlier section), we find that the effective bulk modulus of the compressible magma is 0.9-3.0 GPa for a magma reservoir at 200 MPa, or 0.5-1.0 GPa for a magma reservoir at 150 MPa (**figure 16**). Previously, the effective bulk modulus was calculated for Soufrière HiIls magma based on around 5.0 wt% H_2O and no excess exsolved vapour at 5-7 km depth (1 GPa; Voight et al., 2010), although it was acknowledged that observations of volatiles in both gases and melt inclusions suggests that that exsolved volatile phases in addition to H_2O are available to enhance the compressibility of magma at depth (Voight et al., 2010).

We investigate the implications of the reduced effective magma bulk modulus for eruption duration, and total erupted volume by considering a simple model whereby magma eruption rate Q is proportional to magma chamber overpressure Δp by λ, and that eruption is triggered by the attainment of a critical overpressure (we use 5 MPa; after Stasiuk et al., 1993; Huppert and Woods, 2002).

$$Q = \lambda \Delta p$$
$$\lambda = 0.1 \frac{\left(\rho_{bulk} A^2\right)}{H\mu} \quad (7)$$

where A is the conduit cross-sectional area (150 m^2), H is the magma chamber depth (8500 m) and μ is the magma viscosity (10^6 Pas; from Melnik and Sparks, 2002). We assume that the effects of eruption on magma compressibility are small. The total erupted volume V_e and eruption duration τ are given by (from Huppert and Woods, 2002):

$$V_e = \frac{V \Delta p_0}{\beta_{eff}}$$
$$\tau = \frac{\rho_{bulk} V}{\lambda \beta_{eff}} \quad (8)$$

where V is the magma chamber volume (allowed to vary from 10 to 1000 km^3) and Δp_0 is

the critical magma chamber overpressure required for eruption. The effect of varying bulk modulus and magma chamber volume on total erupted volume and eruption duration, given no magma recharge, are shown in **figure 17**. If magma recharge is incorporated, then eruption duration and erupted volume both increase by a magnitude dependent on the ratio between the critical overpressure for eruption and the recharge rate. If the recharge rate varies with time, then the relationships between total erupted volume, eruption duration and magma chamber volume become non-linear. We find, using this simple model, that the volume of the depth-integrated magma chamber must be 60-200 km^3 to account for both the eruption duration (>16 years), and the total erupted volume thus far (around 1 km^3). These estimates are consistent with those derived from considerations of ground deformation data (e.g Voight et al., 2010), and with seismic tomography, which, in combination with thermal modelling, has imaged 13 km^3 magma containing >30% melt between 5.5 and 7.5 km depth (which may represent only the top portion of the storage region; Paulatto et al., 2012). A large volume magma chamber is also consistent with the observation of a relatively constant bulk composition of the erupted products, despite quasi-continuous mafic recharge.

The mass fraction of exsolved vapour in the magma chamber may vary with time. Large lava dome collapses have been associated with large syn-collapse emissions of SO_2 gas (Edmonds et al., 2003; Carn et al., 2000; Carn and Prata, 2010; **figure 8**). This expulsion of vapour from the magma chamber may reduce both magma chamber overpressure and the bulk modulus of the remaining magma reservoir dramatically, which may initiate an eruptive pause whilst the reservoir is replenished, in both melt and exsolved vapour.

The lowering of the magma effective bulk modulus (or enhancement of compressibility) caused by the presence of substantial exsolved vapour has implications for interpretation of ground deformation data (Rivalta and Segall, 2008). It has been noted previously that the volumes inferred from modelling the continuous GPS data during periods of lava effusion are much lower than the dense rock equivalent (DRE) volumes (Elsworth et al., 2008; Mattioli et al., 2010; Voight et al, 2010; Foroozan et al., 2010). Part of this discrepancy must relate to magma recharge, as inflation occurs during repose periods (Voight et al., 2010). It is likely, however, that part of the discrepancy must also be due to the buffering effect of exsolved vapour on volume during magma reservoir decompression caused by magma removal. During episode 3 of lava dome growth, from 1 August 2005 to 20 April 2007, 282 x 10^6 m^3 magma (DRE) was erupted (Wadge et al., 2010). Using a single MOGI source at 11 km depth to model the subsidence accompanying lava extrusion as measured by continuous GPS, Mattioli et al. (2010) inferred a change in volume of only 53 +/-2 x 10^6 m^3, only 18-20% of the

observed volume erupted. If we assume a magma chamber volume of 100 km^3, then this erupted volume represents the removal of only 3 vol% of the total volume of magma in the reservoir, which is quite easily fully or partly accommodated through expansion of the exsolved vapour phase, which occupies 4-8 vol% (**figure 12**) at a pressure of 280 MPa (the pressure corresponding to the best fit depth of a single, point source; Mattioli et al., 2010). For comparison, eruption rate and geodetic data for the recent eruption of Mount St Helens (2004-2008) are consistent with eruption from a 10–25 km^3 reservoir containing 0.5–2 vol% exsolved vapour, an initial overpressure of 10–20 MPa, and no significant, sustained recharge (Mastin et al., 2009), using similar arguments for the effects of magma compressibility. The relatively small exsolved gas fraction prior to eruption at Mount St Helens is consistent with observations of very low fluxes of volcanic gases, in comparison to the more gas-rich eruptions in the 1980s (Gerlach et al., 2008); and with the eruption style, which was dominantly slow lava effusion (Vallance et al., 2008).

The presence of exsolved vapour in the magma storage reservoir has further implications for eruption dynamics and magma fragmentation processes. Even prior to magma decompression and eruption, the presence of pre-eruptive exsolved vapour bubbles imply that the magma has significant bulk porosity (4-11 vol% at 200-300 MPa) prior to magma decompression and ascent. This initial porosity has consequences for the development of permeability in the magma, its bulk viscosity and density, and subsequently for magma ascent rates and fragmentation in the conduit (Melnik and Sparks, 2002). The presence of pre-eruptive bubbles is implicit (yet not discussed) in most equilibrium models of conduit flow (e.g. Mastin, 2002). Equilibrium degassing cannot take place without pre-existing bubbles, otherwise supersaturation occurs prior to bubble nucleation and growth (Gardner, 2009). Equilibrium degassing is the most effective way of accelerating magma up a conduit or dyke system because there is no supersaturation: exsolution keeps pace with decompression. In reality however, it is likely that exsolution and degassing are not entirely in equilibrium, particularly during fast decompression in relatively hot rhyolite melt. Experiments have shown that magma can degas in equilibrium up to decompression rates of around 1.2 to 1.8 MPa/s for rhyolitic melts at 875 °C which have a viscosity of 10^5-10^6 Pas (Gardner et al., 2009). Studies of crystal (microlite) size distributions in Vulcanian pumice from Soufrière Hills suggest decompression rates of around 0.7-1.4 MPa/s, in multiple steps (assuming pressure drops of 14 MPa over 10-20 s; Couch et al., 2003; Clarke et al., 2007) and therefore decompression rates are probably low enough during the typical style of explosive activity to allow equilibrium degassing to occur, even close to the point of fragmentation, when porosity reaches 55-70 vol% (Melnik and Sparks, 2002). This decompression rate is similar to that

calculated using H_2O profiles in hourglass melt inclusions from Mount St Helens, which imply rates of 0.9-1.6 MPa/s (Humphreys et al., 2008). One important implication of this relatively low decompression rate is that it is likely that no new bubbles nucleate during magma ascent (which requires melt supersaturation).

Existing models of explosive fragmentation at Soufrière Hills have used a magma water content of 5 wt% H_2O and a bubble-free, "just-saturated" magma as a starting point for simulating bubble nucleation and growth (Clarke et al., 2002; 2007; Melnik and Sparks, 2002; Neuberg et al., 2006). This study suggests that initial H_2O contents might be >6 wt%, with an exsolved volatile mass fraction of 1.6 to 2.4 wt% (which might contain up to 50 mol% CO_2). This pre-eruptive vapour likely existed in the form of a population of small bubbles (of the order of a few microns in size), which then grow during magma decompression, with very little nucleation of new bubbles owing to the relatively low decompression rates, which allows equilibrium degassing to occur (similar to the "equilibrium mass transfer" case considered by Melnik and Sparks, 2002). The initial population of small bubbles leaves no trace in the resulting vesicle textures found in erupted andesite, as they have both grown in size and been subject to bubble coalescence. The original bubble population was likely to be small, with bubble number densities of 10^9-10^{12} cm^{-3} (using a porosity of 4-11 vol% and a bubble radius of 1-10 μm), which would promote trapping inside the magma instead of buoyant rise. These bubbles, at these high number densities, are expected to grow in size by approximately an order of magnitude during magma decompression to 40 MPa (Gardner et al., 1999), yielding a vesicle size distribution with a mode at 10-100 μm, similar to what we observe (**figure 6**).

Conclusions

We use the volatile contents of melt inclusions and nominally anhydrous phenocrysts, combined with volcanic gas flux and composition and the textural analysis of mafic inclusions erupted with the host andesite to conduct a detailed study of the volatile budget and to estimate the mass of exsolved vapour coexisting with magma prior to eruption at Soufrière Hills Volcano, Montserrat. Pre-eruptive andesite magma coexists with an exsolved vapour made up of 50-60 mol% H_2O, 40-50 mol% CO_2 and 1-4 mol% S gases and comprises 1.6-2.4 wt% of the bulk magma. The water contents of orthopyroxene phenocrysts indicate a deep zone of magma storage corresponding to a minimum pressure range (we have no record of melt CO_2) of 130-370 MPa, with a mode at 260 MPa, equivalent to ~ 10 km depth in the crust. Melt inclusions, in contrast, have equilibrated at shallower pressures, between 100 and

300 MPa, and inclusions containing >3 wt% H_2O are also enriched in CO_2, suggesting isobaric flushing with CO_2-rich gases. The intrusion of mafic magma into the andesite supplies heat and volatiles that sustains eruption and recharges the exsolved vapour content of the magma storage reservoir. The mafic magma contains >8 wt% H_2O (and likely significant quantities of CO_2 and S) upon intrusion into the host andesite at a pressure of 200-300 MPa and is likely saturated with respect to volatiles upon intrusion. Rapid quenching against the cooler andesite is accompanied by crystallisation and vesiculation, generating a porosity of 10-25 vol% in the mafic inclusions. The mafic inclusions often have a glassy margin, preventing gas loss by permeable flow, whilst the interior retains up to 40 wt% melt. Flotation of enclaves takes place when the bulk density becomes similar to that of the overlying the andesite. Upon entrainment into the andesite and magma decompression, we propose that most of the mafic inclusions undergo ductile autofragmentation, when further exsolution and expansion of the volatile phase in the interior of the inclusions overcomes the strength of the margins and crystal frameworks. In this way, the mafic components (crystals, melt and exsolved vapour) are scattered within the andesite host, generating a hybrid mixed magma and recharging the exsolved vapour content of the magma reservoir. The exsolved vapour in the andesite may amount to 4.3 to 8.2 vol% at 300 MPa and 6.0-11 vol% at 200 MPa and it is likely that the magma reservoir is zoned with respect to exsolved vapour, with the highest volume fractions of vapour in the upper part of the chamber. This volume of compressible fluid has important implications for eruption longevity and erupted volume, and for the behaviour of the magma reservoir during magma recharge and eruption. Using a simple model of no recharge and an output rate proportional to magma chamber pressure, we use the erupted volume and duration thus far to estimate the magma reservoir volume to be in the range 60-200 cubic kilometres. The exsolved vapour may in large part account for the discrepancy in volumes derived from best-fit models of ground deformation during eruptive periods, whereby the vapour expands in response to the decompression caused by magma removal, thereby compensating for a large proportion of the change in volume caused by eruption. The presence of exsolved vapour prior to magma decompression also has important implications for models of magma ascent and fragmentation: exsolution is likely to proceed in equilibrium during magma ascent, even during Vulcanian activity, with little nucleation of new bubbles. The development of porosity and permeability in models of magma flow must take into account the starting porosity.

Acknowledgements

ME acknowledges NERC grants NE/F001487/1 and NE/I016694/1, NERC ion probe facility grant IMF429/0511 and a Royal Society Research Grant. MCSH was supported by a Junior Research Fellowship from Trinity College, Cambridge and by a Royal Society University Research Fellowship. MCSH acknowledges the support of NERC ion probe facility grant IMF316/1007 and collaborative support from BGS. The Montserrat Volcano Observatory provided logistical support for the installation and servicing of the Multi-GAS instrument. Support staff Martin Walker and Jason Day at Earth Sciences, Cambridge provided assistance with sample preparation.

References

AIUPPA, A., FEDERICO, C., GIUDICE, G., GURRIERI, S., LIUZZO, M., SHINOHARA, H., FAVARA, R. M. & VALENZA, M. 2006. Rates of carbon dioxide plume degassing from Mount Etna volcano. *Journal of Geophysical Research*, 111(B09207), doi:10.1029/2006JB004307.

ANNEN, C., BLUNDY, J. D. & SPARKS, R. S. J., 2006. The genesis of intermediate and silicic magmas in deep crustal hot zones, *Journal of Petrology*, 47(3), 505–539, doi:10.193/petrology/egi084.

BACHMANN, O. & BERGANTZ G. 2006. Gas percolation in upper-crustal silicic crystal mushes as a mechanism for upward heat advection and rejuvenation of near-solidus magma bodies. *Journal of Volcanology and Geothermal Research*, 149(1–2), 85–102.

BAKER, D. 2008. The fidelity of melt inclusions as records of melt composition. *Contributions to Mineralogy and Petrology,* 156, 377–395.

BARCLAY, J., RUTHERFORD M. J., CARROLL M. R., MURPHY M. D., DEVINE J. D., GARDNER J. & SPARKS, R. S. J. 1998. Experimental phase equilibria constraints on pre-eruptive storage conditions of the Soufriere Hills magma. *Geophysical Research Letters*, 25(18), 3437-3440.

BARCLAY, J., HERD, R. A., EDWARDS, B. R., CHRISTOPHER, T., KIDDLE, E. J., PLAIL, M. & DONOVAN, A. 2010. Caught in the act: Implications for the increasing abundance of mafic enclaves during the recent eruptive episodes of the Soufrière Hills Volcano, Montserrat. *Geophysical Research Letters*, 37(L00E09), doi:10.1029/2010GL042509.

BLUNDY, J. & CASHMAN, K. V. 2005. Rapid decompression-driven crystallization recorded by melt inclusions from Mount St. Helens volcano. *Geology,* 33(10), 793–796.

BLUNDY, J., CASHMAN, K. V., RUST, A. & WITHAM, F. 2010. A case for CO_2-rich arc magmas. *Earth and Planetary Science Letters*, 290(3–4), 289–301.

BROWNE, B. L., EICHELBERGER, J. C., PATINO, L. C., VOGEL, T. A., UTO, K. & HOSHIZUMI, H. 2006. Magma mingling as indicated by texture and Sr /Ba ratios of plagioclase phenocrysts from Unzen volcano, SW Japan. *Journal of Volcanology and Geothermal Research,* 154, 103–116.

CARMICHAEL, I. S. 2002. The andesite aqueduct: perspectives on the evolution of intermediate magmatism in west-central (105-99°W) Mexico. *Contributions to Mineralogy and Petrology*, 143(6), 641-663.

CARN, S. A., WATTS, R. B., THOMPSON, G. & NORTON, G.E. 2000. Anatomy of a lava dome collapse: the 20 March 2000 event at Soufrière Hills Volcano, Montserrat. *Journal of Volcanology and Geothermal Research*, 131(3–4), 241–264.

CARN, S. A. & PRATA, F. J. 2010. Satellite based constraints on explosive SO_2 release from Soufrière Hills Volcano, Montserrat. *Geophysical Research Letters*, 37(L00E22), doi:10.1029/2010GL044971.

CARN, S. A., KROTKOV, N. A., YANG, K., HOFF, R. M., PRATA, A. J., KRUEGER, A. J., LOUGHLIN, S. C. & LEVELT, P. F. 2007. Extended observations of volcanic SO_2 and sulfate aerosol in the stratosphere. *Atmos. Chem. Phys. Discussions*, 7, 2857–2871.

CASHMAN, K. V. & MARSH, B. D. 1988. Crystal size distribution (CSD) in rocks and the kinetics and dynamics of crystallization II: Makaopuhi lava lake. *Contributions to Mineralogy and Petrology,* 99(3), 292-305.

CASHMAN, K. V., MANGAN, M. T., NEWMAN, S. 1994. Surface degassing and modifications to vesicle size distributions in active basalt flows. *Journal of Volcanology and Geothermal Research*, 61(1-2), 45–68.

CHRISTOPHER, T., EDMONDS, M., HUMPHREYS, M. C. S. & HERD, R. A. 2010. Volcanic gas emissions from Soufrière Hills Volcano, Montserrat 1995–2009, with implications for mafic magma supply and degassing. *Geophysical Research Letters*, 37, doi:10.1029/2009GL041325.

Christopher et al., this volume.

CLARKE, A. B., NERI, A., VOIGHT, B., MACEDONIO, G. & DRUITT, T. H. 2002. Computational modelling of the transient dynamics of the August 1997 Vulcanian explosions at Soufrière Hills Volcano, Montserrat: influence of initial conduit conditions on near-vent pyroclastic dispersal. *Geological Society, London, Memoirs* 21, 319-348.

CLARKE, A. B., STEPHENS, S., TEASDALE, R., SPARKS, R.S.J., DILLER, K., 2007. Petrologic constraints on the decompression history of magma prior to Vulcanian explosions at the Soufrière Hills volcano, Montserrat. *Journal of Volcanology and Geothermal Research*, 161(4), 261–274.

CLEMENTE, B., SCAILLET, B. & PICHAVANT, M. 2004. The Solubility of Sulphur in Hydrous Rhyolitic Melts. *Journal of Petrology,* 45(11), 2171–2196.

CLYNNE, M. A. 1999. A Complex Magma Mixing Origin for Rocks Erupted in 1915, Lassen Peak, California. *Journal of Petrology,* 40(1), 105-132.

COOMBS, M. L., EICHELBERGER, J. C. & RUTHERFORD, M. R. 2006. Experimental and textural constraints on mafic enclave formation in volcanic rocks. *Journal of Volcanology and Geothermal Research,* 119, 125-144.

COUCH, S., SPARKS, R. S. J., CARROLL, M. R. 2001. Mineral disequilibrium in lavas explained by convective self-mixing in open magma chambers. *Nature* 411, 1037-1039.

COUCH, S., HARFORD, C. L., SPARKS, R. S. J. & CARROLL, M. R. 2003. Experimental Constraints on the Conditions of Formation of Highly Calcic Plagioclase Microlites at the Soufriere Hills Volcano, Montserrat. *Journal of Petrology*, 44(8), 1455-1475.

DAVIDSON, J., TURNER, S., HANDLEY, H., MACPHERSON, C. & DOSSETO, A. 2007. Amphibole "sponge" in arc crust? *Geology*, 35(9), 787-790.

DEVINE, J. D., GARDNER, J. E., BRACK, H. P., LAYNE, G. D. & RUTHERFORD, M. J.1995. Comparison of microanalytical methods for estimating H_2O contents of silicic volcanic glasses. *American Mineralogist*, 80, 319-328.

DEVINE, J. D., RUTHERFORD, M. R., NORTON, G. E., YOUNG, S. R. 2003. Magma storage region processes inferred from geochemistry of Fe-Ti oxides in andesitic magma, Soufriere Hills Volcano, Montserrat, W.I. *Journal of Petrology,* 44(8), 1375-1400.

DRUITT, T. H., YOUNG, S. R., BAPTIE, B., BONADONNA, C., CALDER, E. S., CLARKE, A. B., COLE, P. D., HARFORD, C. L., HERD, R. A., LUCKETT, R., RYAN, G. & VOIGHT, B. 2002. Episodes of cyclic vulcanian explosive activity with fountain collapse at Soufriere Hills Volcano, Montserrat. *Geological Society, London, Memoirs*, 21, 281-306.

EDMONDS, M., PYLE, D. M. & OPPENHEIMER, C. 2001. A model of degassing at Soufrière Hills Volcano, Montserrat, West Indies, based on geochemical data. *Earth and Planetary Science Letters*, 186, 159-173.

EDMONDS, M., PYLE, D. M., & OPPENHEIMER, C. 2002. HCl emissions at Soufrière Hills Volcano, Montserrat, West Indies, during a second phase of dome building, November 1999 to September 2000, *Bulletin of Volcanology*, 64, 21-30, doi: 10.1007/s00445-001-0175-0.

EDMONDS, M., HERD, R. A., GALLE, B. & OPPENHEIMER, C. 2003a. Automated, high time-resolution measurements of SO_2 flux at Soufrière Hills Volcano, Montserrat, West Indies. *Bulletin of Volcanology*, 65, 578-586, doi: 10.1007/s00445-003-0286-x.

EDMONDS, M., OPPENHEIMER, C. M., PYLE, D. M., HERD, R. A. & THOMPSON, G. 2003b. SO_2 emissions from Soufrière Hills Volcano and their relationship to conduit permeability, hydrothermal interaction and degassing regime. *Journal of Volcanology and Geothermal Research*, 124(1-2), 23-43, doi: 10.1016/S0377-0273(03)00041-6.

EDMONDS, M., 2008. New Geochemical Insights into Volcanic Degassing. *Philosophical Transactions of the Royal Society Series A*, 366, 4559-4579, doi: 10.1098/rsta.2008.0185.

EDMONDS, M., AIUPPA, A., HUMPHREYS, M., MORETTI, R., GIUDICE, G., MARTIN, R. S., HERD, R. A. & CHRISTOPHER, T. 2010. Excess volatiles supplied by mingling of mafic magma at an andesite arc volcano. *Geochemistry, Geophysics, Geosystems*, 11(4), doi:10.1029/2009GC002781.

EICHELBERGER, J. C. 1980. Vesiculation of mafic magma during replenishment of silicic magma reservoirs. *Nature,* 288, 446 – 450.

ELSWORTH, D., MATTIOLI, G., TARON, J., VOIGHT, B. & HERD, R. 2008. Implications of Magma Transfer Between Multiple Reservoirs on Eruption Cycling. *Science* 322, 246-248.

FOGEL, R. A. & RUTHERFORD, M. J. 1990. The solubility of carbon dioxide in rhyolitic melts: A quantitative FTIR study. *American Mineralogist*, 75, 1311–1326.

FOROOZAN, R., D. ELSWORTH, B. VOIGHT & G. S. MATTIOLI, 2010. Dual reservoir structure at Soufrière Hills Volcano inferred from continuous GPS observations and heterogeneous elastic modeling. *Geophysical Research Letters*, 37, L00E12, doi:10.1029/2010GL042511.

GARDNER, J. E., HILTON, M. & CARROLL, M. R. 1999. Experimental constraints on degassing of magma: isothermal bubble growth during continuous decompression from high pressure. *Earth and Planetary Science Letters,* 168, 201–218.

GARDNER, J. E. 2009. The impact of pre-existing gas on the ascent of explosively erupted magma. *Bulletin of Volcanology*, 71, 835–844, DOI 10.1007/s00445-009-0276-8.

GERLACH T. M., WESTRICH, H. R., CASADEVALL, T. J. & FINNEGAN, D. L. 1994. Vapor saturation and accumulation in magmas of the 1989-1990 eruption of Redoubt Volcano, Alaska. *Journal of Volcanology and Geothermal Research,* 62, 317-337.

GERLACH, T. M., MCGEE, K. A., DOUKAS, M. P. 2008. Emission Rates of CO_2, SO_2, and H_2S, Scrubbing, and Preeruption Excess Volatiles at Mount St. Helens, 2004-2005. *US Geological Survey Professional Paper*, 1750, 543-571.

GHIORSO, M. S. & SACK, R. O. 1995. Chemical Mass Transfer in Magmatic Processes. IV. A Revised and Internally Consistent Thermodynamic Model for the Interpolation and Extrapolation of Liquid-Solid Equilibria in Magmatic Systems at Elevated Temperatures and Pressures. *Contributions to Mineralogy and Petrology,* 119, 197-212.

GRANT, K. J., KOHN, S. C. & BROOKER, R. A. 2007. The partitioning of water between olivine, orthopyroxene and melt synthesised in the system albite–forsterite–H_2O. *Earth and Planetary Science Letters* 260, 227–241.

GUALDA, G. A. R. & ANDERSON JR, A. T. 2007. Magnetite scavenging and the buoyancy of bubbles in magmas. Part 1: Discovery of a pre-eruptive bubble in Bishop rhyolite. *Contributions to Mineralogy and Petrology,* 153, 733–742, DOI 10.1007/s00410-006-0173-5.

GUALDA, G. A. R., GHIORSO, M. S., LEMONS, R. V. & CARLEY, T. L. 2012. Rhyolite-MELTS: A modified calibration of MELTS optimized for silica-rich, fluid-bearing magmatic systems. *Journal of Petrology*, published online, doi: 10.1093/petrology/egr080.

HAMMOUYA, G., ALLARD, P., JEAN-BAPTISTE, P., PARELLO, F., SEMET, M. P. & YOUNG, S. R. 1998. Pre- and syn-eruptive geochemistry of volcanic gases from Soufrie're Hills Volcano, Montserrat, West Indies. *Geophysical Research Letters,* 25, 3685-3688.

HATTORI, K. 1993. High-sulfur magma, a product of fluid discharge from underlying mafic magma: Evidence from Mount Pinatubo, Philippines. *Geology*, 21(12), 1083-1086.

HAURI, E., WANG, J., DIXON, J. E., KING, P. E., MANDEVILLE, C. & NEWMAN, S. 2002. SIMS analysis of volatiles in silicate glasses 1. Calibration, matrix effects and comparisons with FTIR. *Chemical Geology,* **183**, 99– 114.

HAURI, E. H., GAETANI, G. A. & GREEN, T. H. 2006. Partitioning of water during melting of the Earth's upper mantle at H_2O-undersaturated conditions. *Earth and Planetary Science Letters,* 248, 715–734.

DE HOOG, J. C. M., HATTORI, K. H. & HOBLITT, R. P. 2004. Oxidized sulfur-rich mafic magma at Mount Pinatubo, Philippines. *Contributions to Mineralogy and Petrology,* 146, 750–761, DOI 10.1007/s00410-003-0532-4.

HUMPHREYS, M. C. S., BLUNDY, J. & SPARKS, R. S. J. 2006. Magma Evolution and Open-System Processes at Shiveluch Volcano: Insights from Phenocryst Zoning. *Journal of Petrology* 47(12), 2303-2334.

HUMPHREYS, M. C. S., MENAND, T., BLUNDY, J. D., KLIMM, K. 2008. Magma ascent rates in explosive eruptions: Constraints from H_2O diffusion in melt inclusions. *Earth and Planetary Science Letters*, 270(1–2), 25–40.

HUMPHREYS, M. C. S., CHRISTOPHER, T. & HARDS, V. 2009a. Microlite transfer by disaggregation of mafic inclusions following magma mixing at Soufrie`re Hills volcano, Montserrat. *Contributions to Mineralogy and Petrology,* 157, 609–624, DOI 10.1007/s00410-008-0356-3.

HUMPHREYS, M. C. S., EDMONDS, M., CHRISTOPHER, T., HARDS, V. 2009b. Chlorine variations in the magma of Soufriere Hills Volcano, Montserrat: Insights from Cl in hornblende and melt inclusions. *Geochimica et Cosmochimica Acta,* 73(19), 5693-5708

HUMPHREYS, M. C. S., EDMONDS, M., CHRISTOPHER, T. & HARDS, V., 2010. Magma hybridisation and diffusive exchange recorded in heterogeneous glasses from Soufrière Hills Volcano, Montserrat. *Geophysical Research Letters*, 37, doi:10.1029/2009GL041926.

HUMPHREYS, M. C. S., EDMONDS, M., BARCLAY, J., PLAIL, M., PARKES, D. & CHRISTOPHER, T. 2012. A new method to quantify the real supply of mafic components to a hybrid andesite. *Contributions to Mineralogy and Petrology*, online first, DOI: 10.1007/s00410-012-0805-x.

HUPPERT, H. & WOODS, A. W. 2002. The role of volatiles in magma chamber dynamics. *Nature,* 420, 493-495.

KLUG C. & CASHMAN, K. V. 1994. Vesiculation of May 18, 1980, Mount St. Helens magma. *Geology*, 22(5), 468-472.

KOGA, K., HAURI, E., HIRSCHMANN, M., BELL, D. 2003. Hydrogen concentration analyses using SIMS and FTIR: Comparison and calibration for nominally anhydrous minerals. *Geochemistry, Geophysics, Geosystems*, 4(1019), doi:10.1029/2002GC000378.

KOHN S. C., ROOME, B. M., SMITH, M. E. & HOWES, A. P. 2005. Testing a potential mantle geohygrometer; the effect of dissolved water on the intracrystalline partitioning of Al in orthopyroxene. *Earth and Planetary Science Letters,* 238, 342–350.

KOYAGUCHI, T., & BLAKE, S. 1991, Origin of mafic enclaves: Constraints on the magma mixing model from fluid dynamic experiments, in DIDIER, J. & BARBARIN, B. eds. Enclaves and granite petrology: Amsterdam, Elsevier, p. 415–429.

LESNE, P., S. C. KOHN, J. BLUNDY, F. WITHAM, R. E. BOTCHARNIKOV, H. BEHRENS, 2011. Experimental Simulation of Closed-System Degassing in the System Basalt–H_2O–CO_2–S–Cl. *Journal of Petrology*, 52, 9, 1737-1762.

MANGAN M., CASHMAN, K. V. & NEWMAN, S. 1993. Vesiculation of basaltic magma during eruption. *Geology,* 21, 157-160.

MANGAN M. & SISSON, T. 2000. Delayed, disequilibrium degassing in rhyolite magma: decompression experiments and implications for explosive volcanism. *Earth and Planetary Science Letters,* 183, 441-455.

MARSH, B. D. 1998. Crystal size distribution (CSD) in rocks and the kinetics and dynamics of crystallization: I. Theory. *Contributions to Mineralogy and Petrology,* 99, 277–291.

MARTIN, V. M., PYLE, D. M. & HOLNESS, M. B. 2006. The role of crystal frameworks in the preservation of enclaves during magma mixing. *Earth and Planetary Science Letters,* 248, 787–799.

MASTIN, L. G. 2002, Insights into volcanic conduit flow from an open-source numerical model. *Geochemistry, Geophysics, Geosystems*, 3(7), 10.1029.

MASTIN L. G., LISOWSKI, M., ROELOFFS, E. & BEELER, N. 2009. Improved constraints on the estimated size and volatile content of the Mount St. Helens magma system from the 2004–2008 history of dome growth and deformation. *Geophysical Research Letters*, 36(L20304), doi:10.1029/2009GL039863.

MATTIOLI, G. S., HERD, R. A., STRUTT, M. S., RYAN, G., WIDIWIJAYANTI, C. & VOIGHT, B. 2010. Long term surface deformation of Soufrière Hills Volcano, Montserrat from GPS geodesy: Inferences from simple elastic inverse models. *Geophysical Research Letters*, 37(L00E13), doi:10.1029/2009GL042268.

MELNIK, O. & SPARKS, R. S. J. 1999. Nonlinear dynamics of lava dome extrusion. *Nature,* 402, 37-41.

MELNIK, O. & SPARKS, R. S. J. 2002. Dynamics of magma ascent and lava extrusion at Soufrière Hills Volcano, Montserrat. Geological Society, London, Memoirs, 21, 153-171.

MELNIK, O., BARMIN, A.A., SPARKS, R.S.J. 2005. Dynamics of magma flow inside volcanic conduits with bubble overpressure buildup and gas loss through permeable magma. *Journal of Volcanology and Geothermal Research,* 143, 53– 68.

METRICH, N. & WALLACE, P. J. 2008. Volatile Abundances in Basaltic Magmas and Their Degassing Paths Tracked by Melt Inclusions. *Reviews in Mineralogy & Geochemistry*, 69, 363-402, 2008.

MIERDEL, K. & KEPPLER, H. 2004. The temperature dependence of water solubility in enstatite. *Contributions to Mineralogy and Petrology,* 148, 305–311, DOI 10.1007/s00410-004-0605-z.

MOORE, G. & CARMICHAEL, I. S. E. 1998. The hydrous phase equilibria (to 3 kbar) of an andesite and basaltic andesite from western Mexico: constraints on water content and conditions of phenocryst growth. *Contributions to Mineralogy and Petrology,* 130(3-4), 304-319, DOI: 10.1007/s004100050367

MURPHY, M. D., SPARKS R. S. J., BARCLAY, J., CARROLL, M. R., LEJEUNE, A. M., BREWER, T. S., MACDONALD, R., BLACK, S. & YOUNG, S. 1998. The role of magma mixing in triggering the current eruption at the Soufrière Hills volcano, Montserrat, West Indies. *Geophysical Research Letters,* 25(18), 3433–3436.

MURPHY, M. D., SPARKS, R. S. J., BARCLAY, J., CARROLL, M. J. & BREWER, T. S. 2000. Remobilisation of andesite magma by intrusion of mafic magma at the Soufrière Hills volcano, Montserrat, West Indies. *Journal of Petrology,* 41, 21-42.

NEWMAN, S. & LOWENSTERN, J. B. 2002. VolatileCalc: a silicate melt–H2O–CO2 solution model written in Visual Basic for excel. Com*puters & Geosciences,* 28, 597–604.

NEUBERG, J. W., TUFFEN, H., COLLIER, L., GREEN, D., POWELL, T. & DINGWELL, D. 2006. The trigger mechanism of low-frequency earthquakes on Montserrat. *Journal of Volcanology and Geothermal Research,* 153, 37–50.

OPPENHEIMER, C., EDMONDS, M., FRANCIS, P. & BURTON M. 2002. Variation in HCl/SO_2 gas ratios observed by Fourier transform spectroscopy at Soufrière Hills Volcano, Montserrat. *Geological Society, London, Memoirs*, 21, p. 621-639.

PAPALE, P. & POLACCI, M. 2009. Role of carbon dioxide in the dynamics of magma ascent in explosive eruptions. *Bulletin of Volcanology*, 60, 583–594.

PLAIL, M., BARCLAY, J., HUMPHREYS, M. C. S., EDMONDS, M., HERD R. & CHRISTOPHER, T. this volume. Characterisation of mafic enclaves in the erupted products of Soufrière Hills Volcano, Montserrat 1995-2010.

PRATA, A. J., CARN, S. A., STOHL, A. & KERKMANN, J. 2007. Long range transport and fate of a stratospheric volcanic cloud from Soufrière Hills volcano, Montserrat. *Atmospheric Chemistry and Physics,* 7(19), 5093-5103.

PAULATTO, M., MINSHULL, T. A. & HENSTOCK, T. J. 2010. Constraints on an intrusive system beneath the Soufriére Hills Volcano, Montserrat, from finite difference modeling of a controlled source seismic experiment. *Geophysical Research Letters*, 37(L00E01), doi:10.1029/2009GL041805.

PAULATTO, M, C. ANNEN, T. J. HENSTOCK, E. KIDDLE, T. A. MINSHULL, R. S. J. SPARKS, B. VOIGHT, 2012. Magma chamber properties from integrated seismic tomography and thermal modeling at Montserrat. *Geochemistry, Geophysics, Geosystems,* 13(1), DOI: 10.1029/2011GC003892.

RAUCH, M. & KEPPLER, H. 2002. Water solubility in orthopyroxene. *Contributions to Mineralogy and Petrology* 143, 525–536, DOI 10.1007/s00410-002-0365-6.

RIDOLFI, F AND A RENZULLI, 2006. Calcic amphiboles in calc-alkaline and alkaline magmas: thermobarometric and chemometric empirical equations valid up to 1,130°C and 2.2 GPa. *Contributions to Mineralogy and Petrology*, DOI 10.1007/s00410-011-0704-6.

Rivalta, E and P Segall, 2008. Magma compressibility and the missing source for some dike Intrusions. *Geophysical Research Letters*, 35(L04306), doi:10.1029/2007GL032521.

SCAILLET, B., CLEMENTE, B., EVANS, B. W. & PICHAVANT, M. 1998. Redox control of sulfur degassing in silicic magmas. *Journal of Geophysical Research,* 103(B10), 23,937-23,949.

SCAILLET, B. & EVANS, B. W. 1999. The 15 June 1991 Eruption of Mount Pinatubo. I. Phase Equilibria and Pre-eruption *P–T–f*O_2–*f*H_2O Conditions of the Dacite Magma. *Journal of Petrology*, 40(3), 381-411, doi: 10.1093/petroj/40.3.381.

SCAILLET, B. & PICHAVANT, M. 2003. Experimental constraints on volatile abundances in arc magmas and their implications for degassing processes. *Geological Society, London, Special Publications*, 213, 23-52.

SCHMIDT, M. W. & POLI, S. 1998. Experimentally based water budgets for dehydrating slabs and consequences for arc magma generation. *Earth Planetary Science Letters,* 163, 361–79.

SEAMAN., S.J. & CHAPMAN, M. 2008. The fate of basaltic enclaves during pyroclastic eruptions: An origin of andesitic ignimbrites. *Journal of Volcanology and Geothermal Research,* 178, 671–682.

SHINOHARA, H., TOSHIMICHII IYAMA, J., & MATSUO, S. 1989. Partition of chlorine compounds between silicate melt and hydrothermal solutions: I. Partition of NaCl-KC1. *Geochimica et Cosmochimico Acta,* 53, 2617-2630.

SHINOHARA, H., AIUPPA, A., GIUDICE, G., GURRIERI, S. & LIUZZO, M. 2008. Variation of H_2O/CO_2 and CO_2/SO_2 ratios of volcanic gases discharged by continuous degassing of Mount Etna volcano, Italy. *Journal of Geophysical Research*, 113(B09203), doi:10.1029/2007JB005185.

SIGNORELLI, S. & CARROLL, M. R. 2002. Experimental constraints on the origin of chlorine emissions at the Soufrière Hills volcano, Montserrat. *Bulletin of Volcanology,* 63, 574–575, DOI 10.1007/s00445-001-0176-z.

SISSON, T.W. & GROVE, T.L. 1993. Experimental investigations of the role of H20 in calc-alkaline differentiation and subduction zone magmatism. *Contributions to Mineralogy and Petrology,* 113, 143-16.

SPARKS, R. S. J. & MARSHALL, L. A. 1986. Thermal and mechnamical constraints on mixing between mafic and silicic magmas. *Journal of Volcanology and Geothermal Research*, 29, 99—124.

SPARKS, R. S. J., AND 19 OTHERS 1998. Magma production and growth of the lava dome of the Soufriere Hills Volcano, Montserrat, West Indies: November 1995 to December 1997. *Geophysical Research Letters*, 25, 3421–3424, doi:10.1029/98GL00639.

SPARKS, R. S. J., MURPHY, M. D., LEJEUNE, A. M., WATTS, R. B., BARCLAY, J. B., YOUNG & S. R. 2000. Control on the emplacement of the andesite lava dome of the Soufriere Hills Volcano, Montserrat, by degassing-induced crystallization. *Terra Nova,* 12, 1, 14-20.

STALDER R. & SKOGBY, H. 2002. Hydrogen incorporation in enstatite. *European Journal Mineralogy,* 14(6), 1139-1144.

STALDER, R. 2004. Influence of Fe, Cr and Al on hydrogen incorporation in orthopyroxene. *European Journal Mineralogy*, 16(5), 703-711.

STASIUK, M., JAUPART, C. & SPARKS, R. S. J. 1993. On the variations of flow rate in non-explosive lava eruptions. *Earth Planetary Science Letters*, 114, 505–516.

TAIT, S., C. JAUPART & S. VERGNIOLLE, 1989. Pressure, gas content and eruption periodicity of a shallow, crystallising magma chamber. *Earth and Planetary Science Letters*, 92(1), 107-123.

TATSUMI, Y., & EGGINS, S.,1995. Subduction zone magmatism, Blackwell, Cambridge, 211 pp.

THOMAS, N. & TAIT, S. R. 1997. The dimensions of magmatic inclusions as a constraint on the physical mechanism of mixing. *Journal of Volcanology and Geothermal Research*, 75(1–2), 167–178.

VALLANCE, J. W., SCHNEIDER, D. J., SCHILLING, S. P. 2008. Growth of the 2004-2006 Lava-Dome Complex at Mount St. Helens, Washington. *US Geological Survey Professional Paper*, 1750, 169-208.

VILLEMANT, B., MOUATT, J., MICHEL, A. 2008. Andesitic magma degassing investigated through H_2O vapour–melt partitioning of halogens at Soufrière Hills Volcano, Montserrat (Lesser Antilles). *Earth Planetary Science Letters*, 269(1-2), 271–289.

VOIGHT, B., LINDE, A. T., SACKS, I. S., MATTIOLI, G. S., SPARKS, R. S. J., ELSWORTH, D., HIDAYAT, D., MALIN, P. E., SHALEV, E., WIDIWIJAYANTI, C., YOUNG, S. R., BASS, V., CLARKE, A., DUNKLEY, P., JOHNSTON,

W., MCWHORTER, N., NEUBERG, J., & WILLIAMS, P. 2006. Unprecedented pressure increase in deep magma reservoir triggered by lava-dome collapse. *Geophysical Research Letters,* 33(L03312), doi:10.1029/2005GL024870.

VOIGHT, B., WIDIWIJAYANTI, C., MATTIOLI, G., ELSWORTH, D., HIDAYAT, D. & STRUTT, M. 2010. Magma sponge hypothesis and stratovolcanoes: Case for a compressible reservoir and quasi-steady deep influx at Soufrière Hills Volcano, Montserrat. *Geophysical Research Letters,* 37(L00E05), doi:10.1029/2009GL041732.

WADGE, G., HERD, R., RYAN, G., CALDER, E. S. & KOMOROWSKI, J.C. 2010. Lava production at Soufrière Hills Volcano, Montserrat: 1995–2009. *Geophysical Research Letters,* 37(L00E03), doi:10.1029/2009GL041466.

WADGE, G., VOIGHT, B., SPARKS, R.S.J., COLE, P. & LOUGHLIN, S.C. this volume. An Overview of the Eruption of Soufrière Hills Volcano from 2000-2010.

WALLACE, P. J., 2001. Volcanic SO_2 emissions and the abundance and distribution of exsolved gas in magma bodies. *Journal of Volcanology and Geothermal Research,* 108, 85-106.

WALLACE P. J. & GERLACH, T. M. 1994. Magmatic Vapor Source for Sulfur Dioxide Released During Volcanic Eruptions: Evidence from Mount Pinatubo. *Science,* 265, 497-499.

WALLACE, P. J., ANDERSON, A. T. & DAVIS, A. M. 1995. Quantification of pre-eruptive exsolved gas contents in silicic magmas. *Science,* 377, 612-616.

WALLACE, P.J. & EDMONDS, M. 2011. The Sulfur Budget in Magmas: Evidence from Melt Inclusions, Submarine Glasses, and Volcanic Gas Emissions. *Reviews in Mineralogy and Geochemistry*, 73(1), 215-246, DOI: 10.2138/rmg.2011.73.8.

WALKER, G.P.L. & SKELHORN, R.R. 1966. Some associations of acid and basic igneous rocks. *Earth-Science Reviews*, 2, 93–109.

WATSON, I. M., OPPENHEIMER, C., VOIGHT, B., FRANCIS, P.W., CLARKE, A., STIX, J., MILLER, A.D., PYLE, D.M., BURTON, M.R., YOUNG, S.R., NORTON, G., LOUGHLIN, S. & DARROUX, B. 2001. The relationship between degassing and grounddeformation at Soufrière Hills Volcano, Montserrat. Journal of Volcanology and Geothermal Research, 98, 117–126.

YAMASHITA, S. 1999. Experimental Study of the Effect of Temperature on Water Solubility in Natural Rhyolite Melt to 100 MPa. *Journal of Petrology*, 40(10), 1497–1507.

YOSHIMURA, S. & NAKAMURA, M. 2011. Carbon dioxide transport in crustal magmatic systems. *Earth and Planetary Science Letters,* 307, 470–478.

YOUNG, S. R., FRANCIS, P. W., BARCLAY, J., CASADEVALL, T. J., GARDNER, C. A., DARROUX, B., DAVIES, M. A., DELMELLE, P., NORTON, G. E., MACIEJEWSKI, A. J. H., OPPENHEIMER, C. M. M., STIX, J. & WATSON, I. M., 1998. Monitoring SO_2 emissions at the Soufriere Hills Volcano: implications for changes in eruptive conditions. *Geophysical Research Letters*, 25(19), 3681–3684.

ZAJACZ,, Z., A. CANDEAL, AP. M. PICCOLI, C. SANCHEZ-VALLE, 2012. The partitioning of sulfur and chlorine between andesite melts and magmatic volatiles and the exchange coefficients of major cations. Geochimica Cosmochimica Acta, 89, 81-101.

ZELLMER, G., HAWKESWORTH, C. J., SPARKS, R. S. J., THOMAS, L. E., HARFORD, C. L., BREWER, T. S. & LOUGHLIN, S. C. 2003. Geochemical evolution of the Soufriere Hills Volcano, Montserrat, Lesser Antilles Volcanic Arc. *Journal of Petrology,* 44(8), 1349-1374.

Figures and Tables

Figure 1: Mafic inclusions in lava dome blocks emplaced as a block-and-ash deposit on 8 January 2007 in the Belham River Valley at a) outcrop and b) hand specimen scales. Most of these mafic inclusions are of the crystalline type, of decimetre dimensions, with large vesicles in the interior and glassy margins.

Figure 2: Secondary Ion Mass Spectrometry (SIMS) calibration curves for water in glasses and orthopyroxene, used to convert normalised ion yields to concentrations: linear working curves for rhyolite glass for a) the Cameca 6f at the SIMS facility at the Carnegie Institution; and b) the Cameca 4f NERC SIMS facility at the University of Edinburgh (two curves for two

days of analysis); c) for H_2O in orthopyroxene on the Cameca 6f at the SIMS facility at the Carnegie Institution.

Figure 3: Melt inclusion SIMS volatile data, from the Cameca 6f ion probe at the Carnegie Institution and the Cameca 4f NERC SIMS facility at the University of Edinburgh (differentiated by symbols shown in legend): water (in wt%) plotted versus a) carbon dioxide concentrations (ppm), b) chlorine concentrations (ppm) and c) sulphur concentrations (ppm); d) chlorine plotted against fluorine (both in ppm). Error bars show the estimated uncertainty, based on the standard deviation of repeats of the standard glasses (the uncertainty on chlorine concentration is a similar size to the symbols). Isobars in (a) show melt compositions in equilibrium at a fixed pressure (marked with pressure in MPa) and isopleths show the range of melts in equilibrium with a vapour phase of fixed composition (vapour H_2O composition marked, in mol% H_2O). Isobars and isopleths calculated using VolatileCalc (Newman and Lowenstern, 2002).

Figure 4: Water concentrations in orthopyroxene (in ppm) by SIMS at the Cameca 6f ion probe at the Carnegie Institution, plotted against distance from the rim of the crystal, in microns. Error bars reflect an uncertainty of ~5%.

Figure 5: Images of mafic inclusions in lava dome blocks emplaced 8 January 2007 in the Belham River Valley. Top: backscatter images acquired using the JOEL JSM-820 Scanning Electron Microscope at Earth Sciences, Cambridge; and bottom: transmitted light images acquired using a Zeiss Axioskop microscope. a) a representative “glassy” mafic inclusion and b) a representative “crystalline” mafic inclusion. The transmitted light image bottom left shows isolated vesicles in pools of brown glass. Phases of interest are labelled.

Figure 6: Vesicle volume distributions (left; VVD) and vesicle size distributions (right; VSD), for three representative sample types: a) glassy mafic inclusion, b) crystalline mafic inclusion and c) andesite lava dome rock. Data discussed in text.

Figure 7: Volcanic gas composition and flux data, derived from Multi-GAS and DOAS measurements at Soufrière Hills Volcano. a) Molar CO_2/SO_2 and H_2S/SO_2 ratios in volcanic gases and b) fluxes of CO_2 and SO_2 from June 2010 to January 2011. Uncertainties are typically 8-14% for gas ratios and ~30-35% for gas fluxes.

Figure 8: Cumulative emission of sulphur (in the form of volcanic gases SO_2 and H_2S; from Christopher et al., 2010 and updated using MVO SO_2 fluxes and Multi-GAS data from **figure 7**) and cumulative erupted magma flux (from Wadge et al., this volume) with time.

Figure 9: Melt-orthopyroxene H_2O partition coefficients as a function of orthopyroxene Al_2O_3 content. A regression is drawn through data taken from published experimental results (Koga et al., 2003; Hauri et al., 2006; Grant et al., 2007).

Figure 10: Two profiles of melt H_2O derived from the H_2O concentration in orthopyroxene grains, showing the general pattern of melt H_2O concentrations of 6-8 wt% prevailing throughout growth of the core of the crystal, with a decrease down to 2-4 wt% at the rims. Uncertainties are shown by the error bars and are typically +/-11%.

Figure 11: Histogram to show H_2O concentrations in melts in equilibrium with orthopyroxene (derived from H_2O concentration in orthopyroxene measured by SIMS, using a melt-opx partition coefficient for H_2O; from **table 3**; n=173), and H_2O concentrations in melt inclusions (n=46). Uncertainties in H_2O concentration are shown by the horizontal bars.

Figure 12: The volume of exsolved vapour coexisting with magma prior to eruption, calculated using the Ideal Gas Law. The two curves correspond to the end member cases constrained by the volcanic gas and melt inclusion data, of 1.6 wt% and 2.4 wt% exsolved vapour comprising 50 mol% H_2O and 50 mol% CO_2.

Figure 13: Results of RhyoliteMelts simulations of rapid quenching of a mafic magma from 1200 to 600 °C. a) Melt fraction remaining with temperature, for simulations at pressures ranging from 100 to 300 MPa and for total H_2O contents of 0-10 wt%. H_2O-saturated magmas retain up to 40% melt after quenching, whereas H_2O-free melts crystallise completely. The range of observed glass fractions in the enclaves are shown. b) The evolution of dissolved and exsolved magma H_2O content during quenching at 300 MPa, for a range of total H_2O contents, showing the rapid increase in dissolved H_2O concentrations up to saturation, followed by exsolution and the development of an exsolved vapour.

Figure 14: Results of RhyoliteMelts simulations to show the evolution of bulk magma density during quenching from 1200 to 600 °C, with a range of total H_2O contents (marked) at 100, 200 and 300 MPa. Also shown is the bulk density of andesite magma containing a total of 10 wt% H_2O (grey bar labelled “and”). The temperature range of interest, corresponding to

the temperature difference between the andesite and mafic magma compositions (Murphy et al., 2000; Humphreys et al., 2009a) is delineated by a box.

Figure 15: Comparison between the porosity development in the RhyoliteMelts simulations with that observed in mafic inclusions. The plot shows the results of simulations at 100, 200 and 300 MPa, with each curve corresponding to a different total H_2O content (2, 6 and 10 wt%; marked). Boxes show the range of mean porosities observed for the mafic inclusions, plotted at the temperature range 835-875 °C (from Murphy et al., 2000; Humphreys et al., 2009a).

Figure 16: The variation of effective bulk modulus of bubbly magma (in GPa) with pressure, calculated for total volatile contents of 5, 6.5 and 9.6 wt% (dissolved plus exsolved volatiles; see text for discussion).

Figure 17: The influence of magma effective bulk modulus on the relationships between eruption duration and total erupted volume with magma chamber volume, assuming the simple case of no recharge at depth. Each curve is marked with the effective bulk modulus. Details of calculations are given in text. The current eruption duration (16 years) and erupted volume (~ 1 km^3; Wadge et al., this volume) are marked, with the estimated range in effective bulk modulus calculated from the results presented in this work.

Table 1: Sample types and their emplacement/eruption dates used in this study.

Table 2: Melt inclusion volatile concentrations measured by SIMS at the NERC ion probe facility and at the ion probe facility at the Carnegie Institution. *Analysis in the form of grain number, melt inclusion number. Sample MVO1524d. Cl and H_2O data for the 4f ion probe from Humphreys et al. (2009). f.i.c.: fluid inclusion contamination.

Table 3: Orthopyroxene H_2O content in ppm, measured by SIMS, with distance across the orthopyroxene crystals in microns (10^{-6} m). Also shown are the measured Al_2O_3 concentrations in wt%, the calculated partition coefficient, $D_{H_2O}^{opx-melt}$, for H_2O between opx and melt (from the calibration curve in figure 9), and the calculated melt H_2O content, in wt%, which has an average uncertainty of +/- 11% (see text for more discussion). na: not analysed.

Table 4: Summary of textural data from image analysis backscatter images, including sample type, vesicle number density, bulk porosity (3-D), modal aspect ratio and modal shape factor. Calculations are described in the text.

Table 5: Volcanic gas composition and flux, from Multi-GAS and DOAS instruments, June 2010 to January 2011. Fluxes are in 10^3 kg/day.

Table 6: Estimation of oxygen fugacity relative to the NNO buffer and mafic magma H_2O content (wt%) from mafic amphibole compositions presented by Murphy et al. (2000), using the empirical parameterisation of Ridolfi and Renzulli (2011).

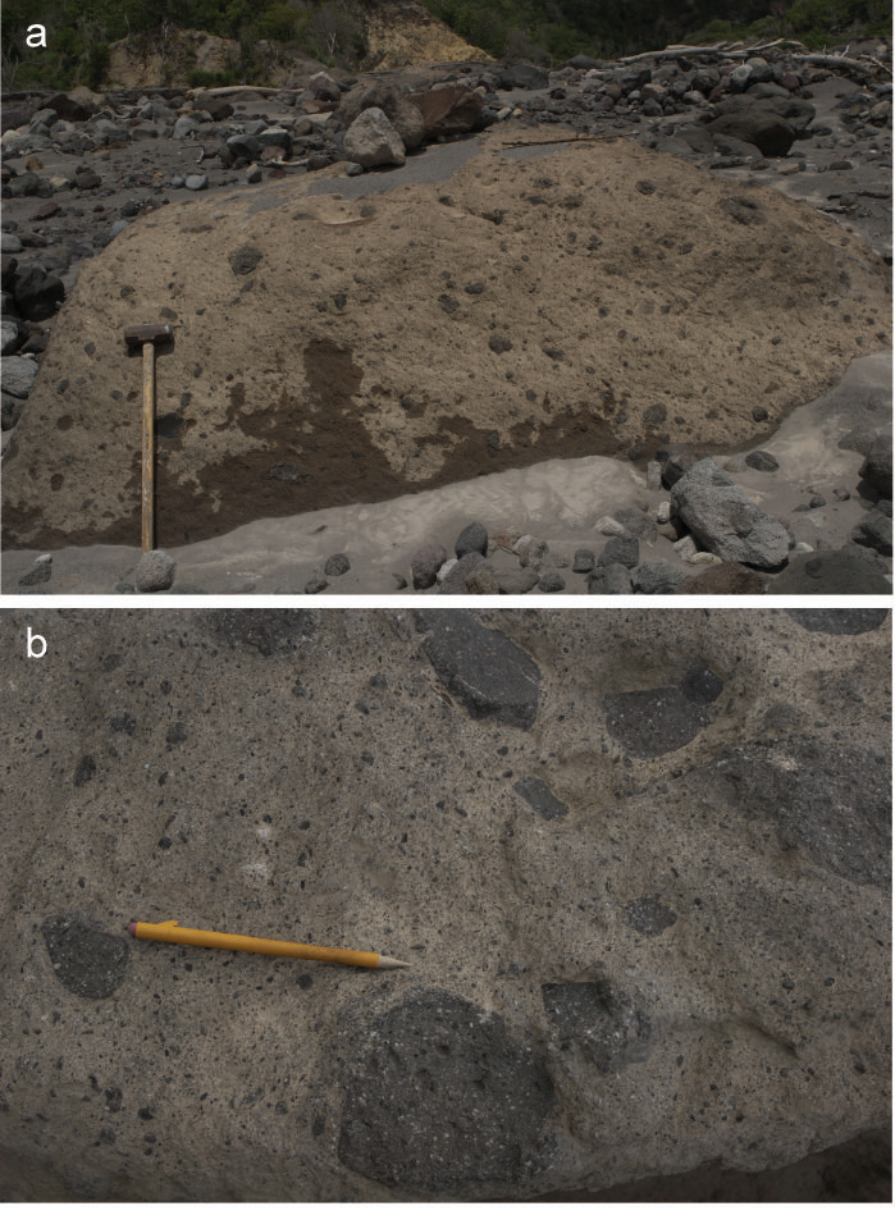
a
b

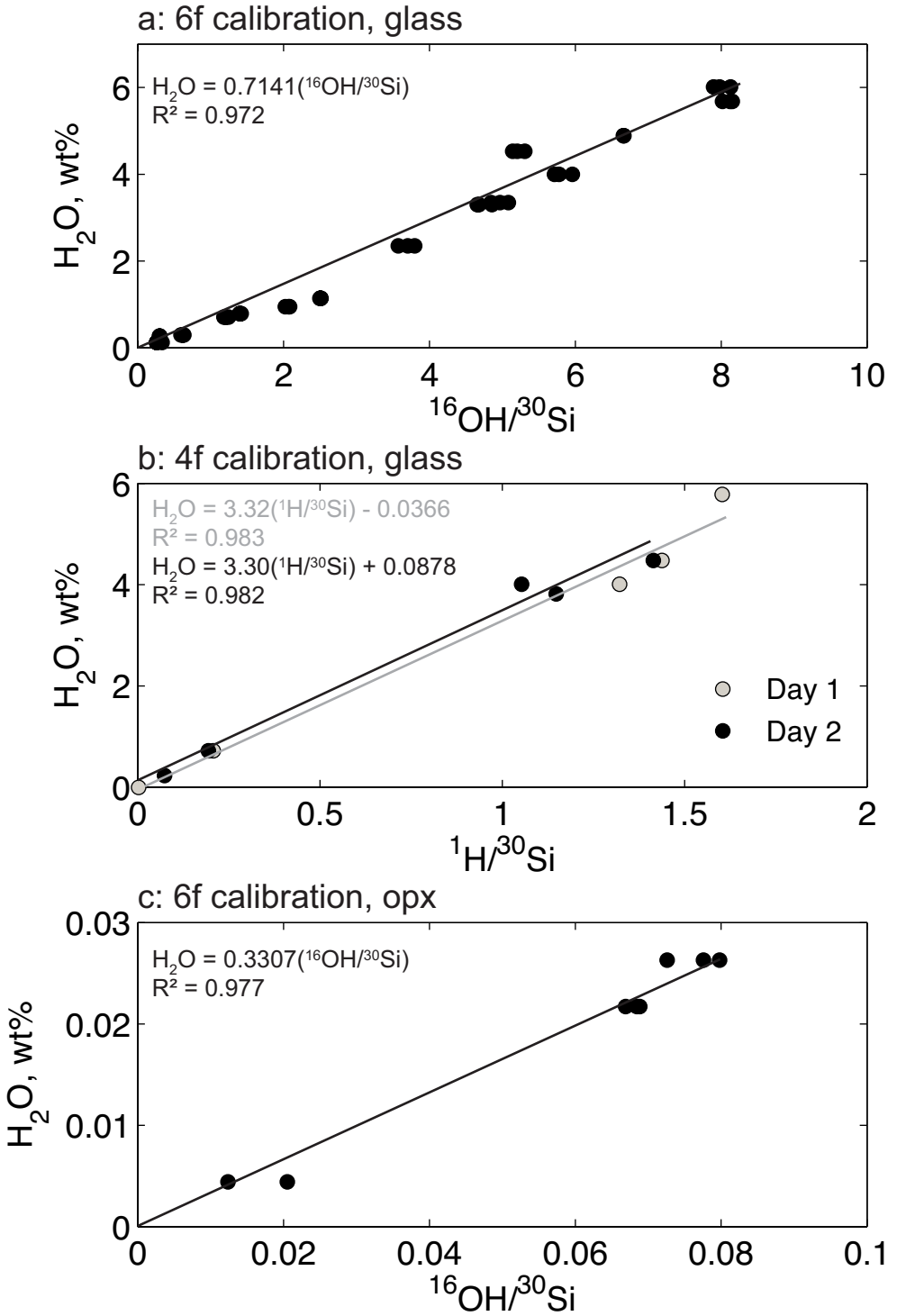
a: 6f calibration, glass
H2O = 0.7141(16OH/30Si)
R² = 0.972
H2O, wt%
16OH/30Si
b: 4f calibration, glass
H2O = 3.32(1H/30Si) - 0.0366
R² = 0.983
H2O = 3.30(1H/30Si) + 0.0878
R² = 0.982
Day 1
Day 2
H2O, wt%
1H/30Si
c: 6f calibration, opx
H2O = 0.3307(16OH/30Si)
R² = 0.977
H2O, wt%
16OH/30Si

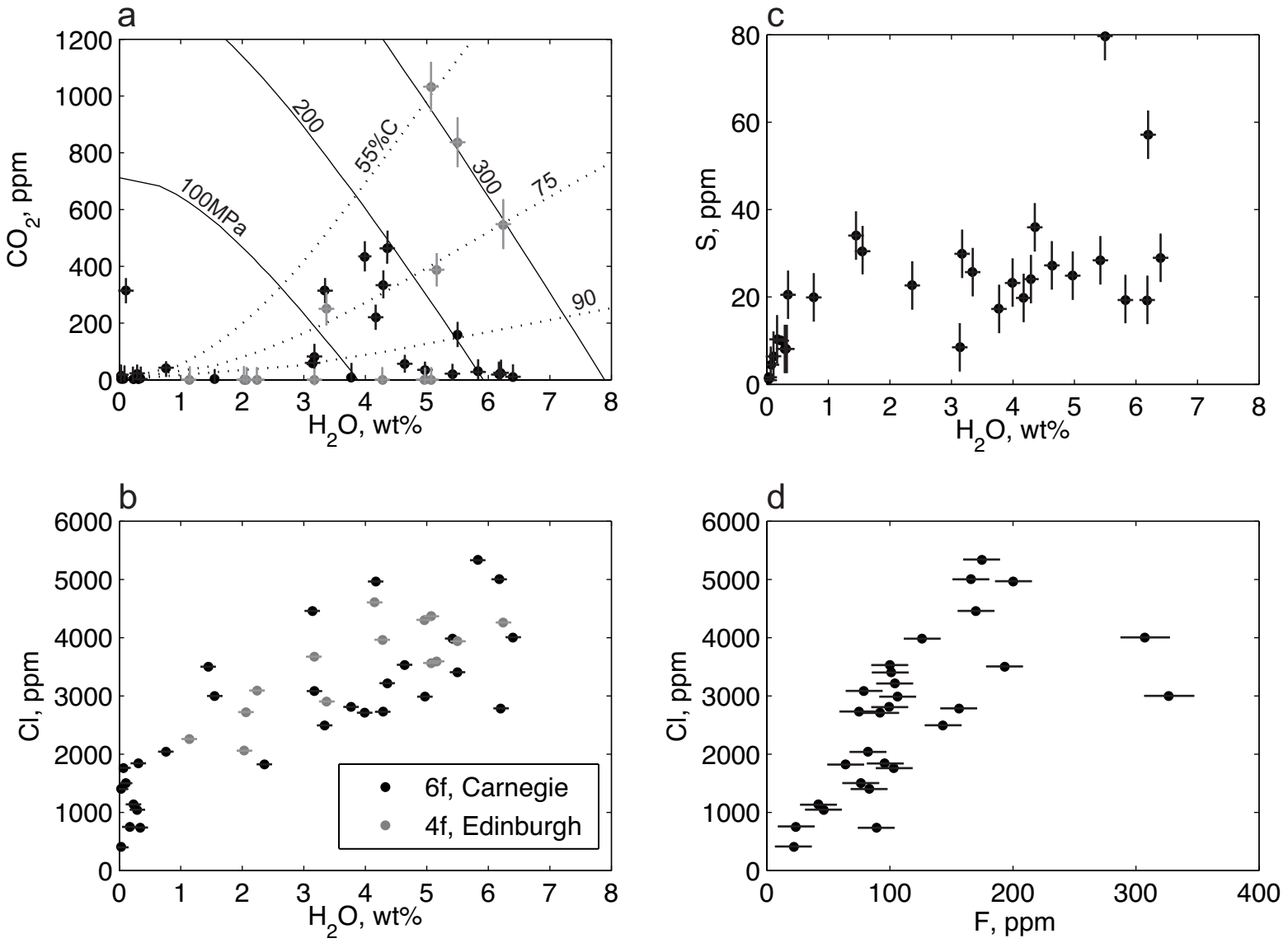
a
CO_2, ppm
H_2O, wt%
200
300
100MPa
55%C
75
90
b
Cl, ppm
H_2O, wt%
6f, Carnegie
4f, Edinburgh
c
S, ppm
H_2O, wt%
d
Cl, ppm
F, ppm

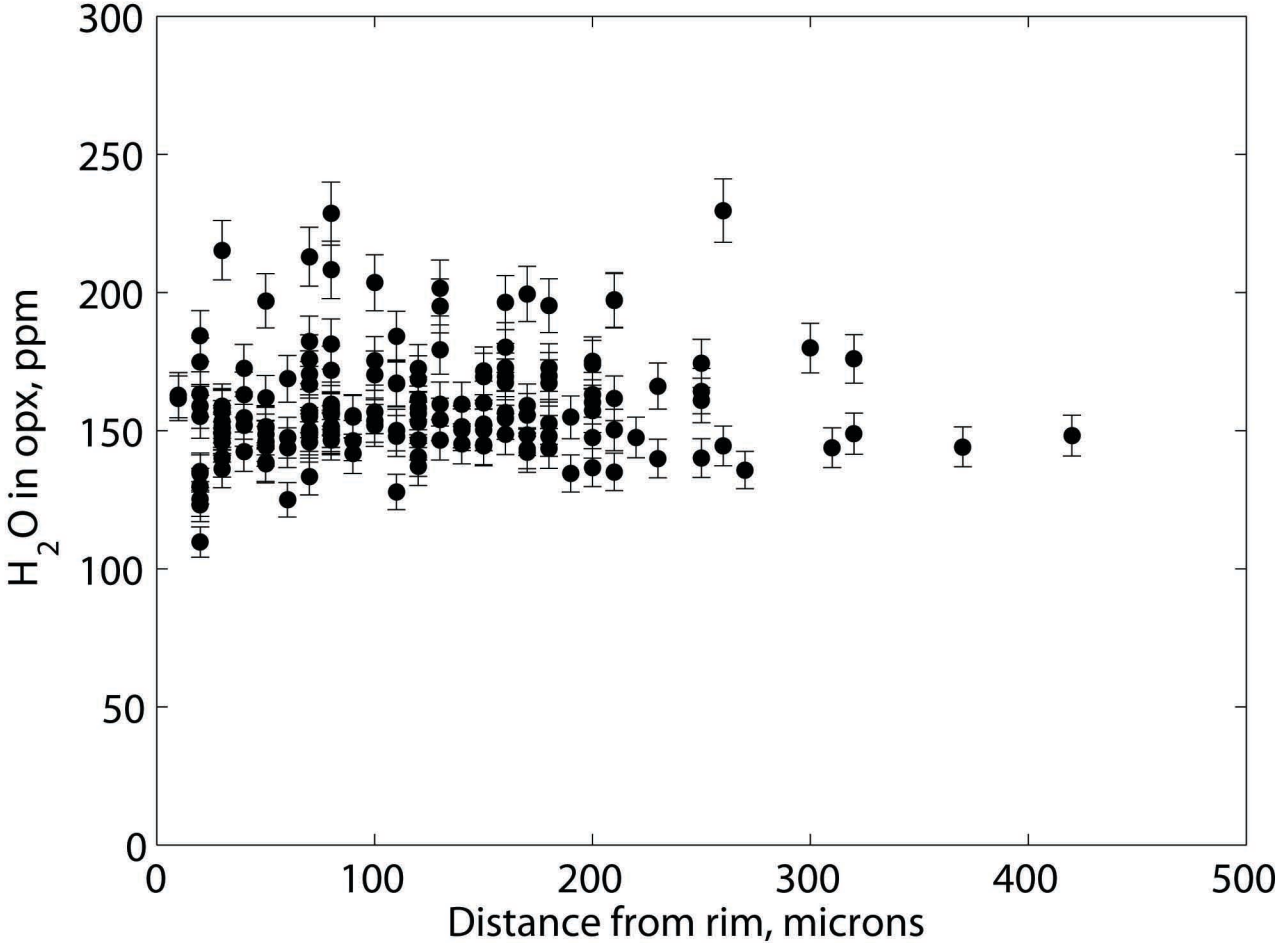
300
250
200
150
100
50
0
H_2O in opx, ppm
0
100
200
300
400
500
Distance from rim, microns

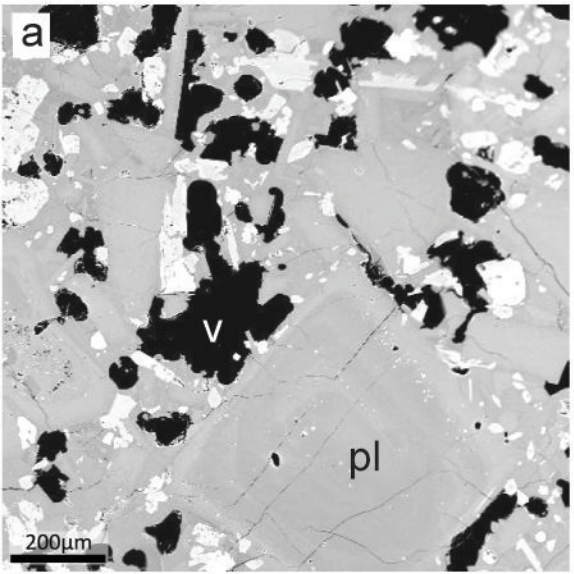
a
v
pl
200µm

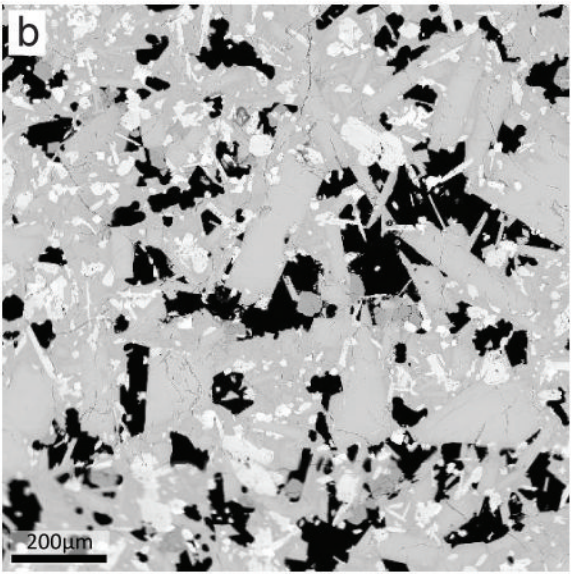
b
200µm

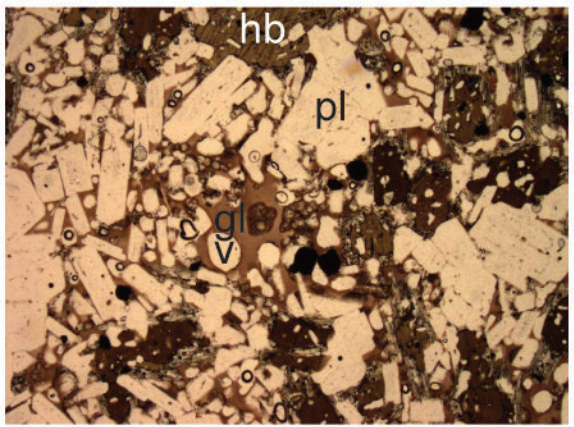
hb
pl
gl
v

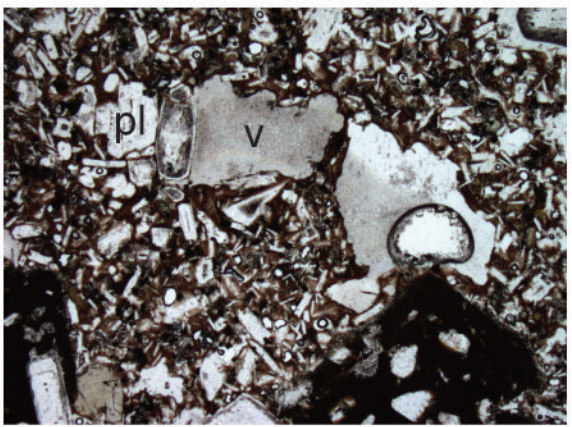
pl
v

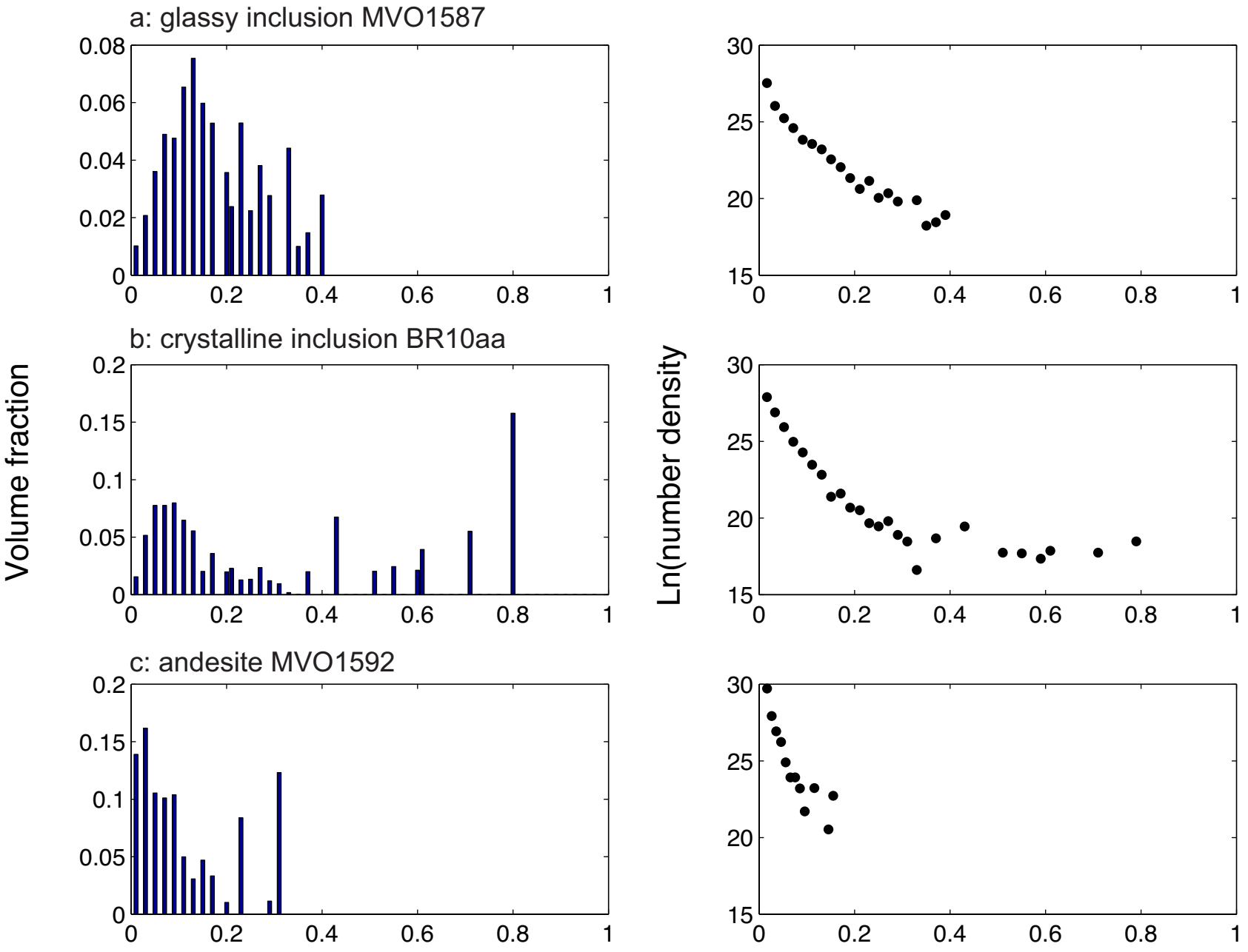
a: glassy inclusion MVO1587
b: crystalline inclusion BR10aa
c: andesite MVO1592
Volume fraction
Ln(number density
Equivalent diameter, mm

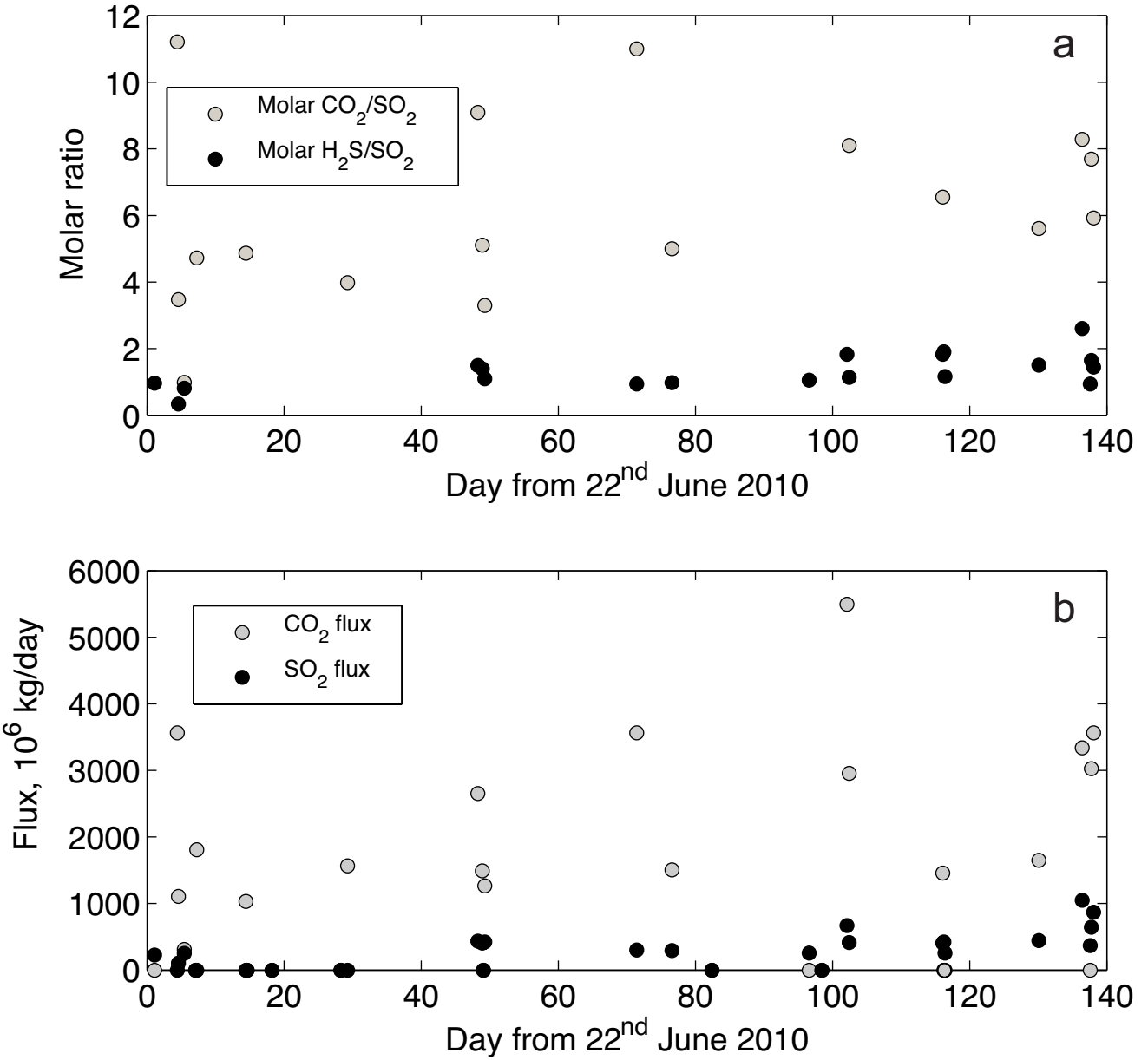
a
Molar CO2/SO2
Molar H2S/SO2
Molar ratio
Day from 22nd June 2010
b
CO2 flux
SO2 flux
Flux, 10^6 kg/day
Day from 22nd June 2010

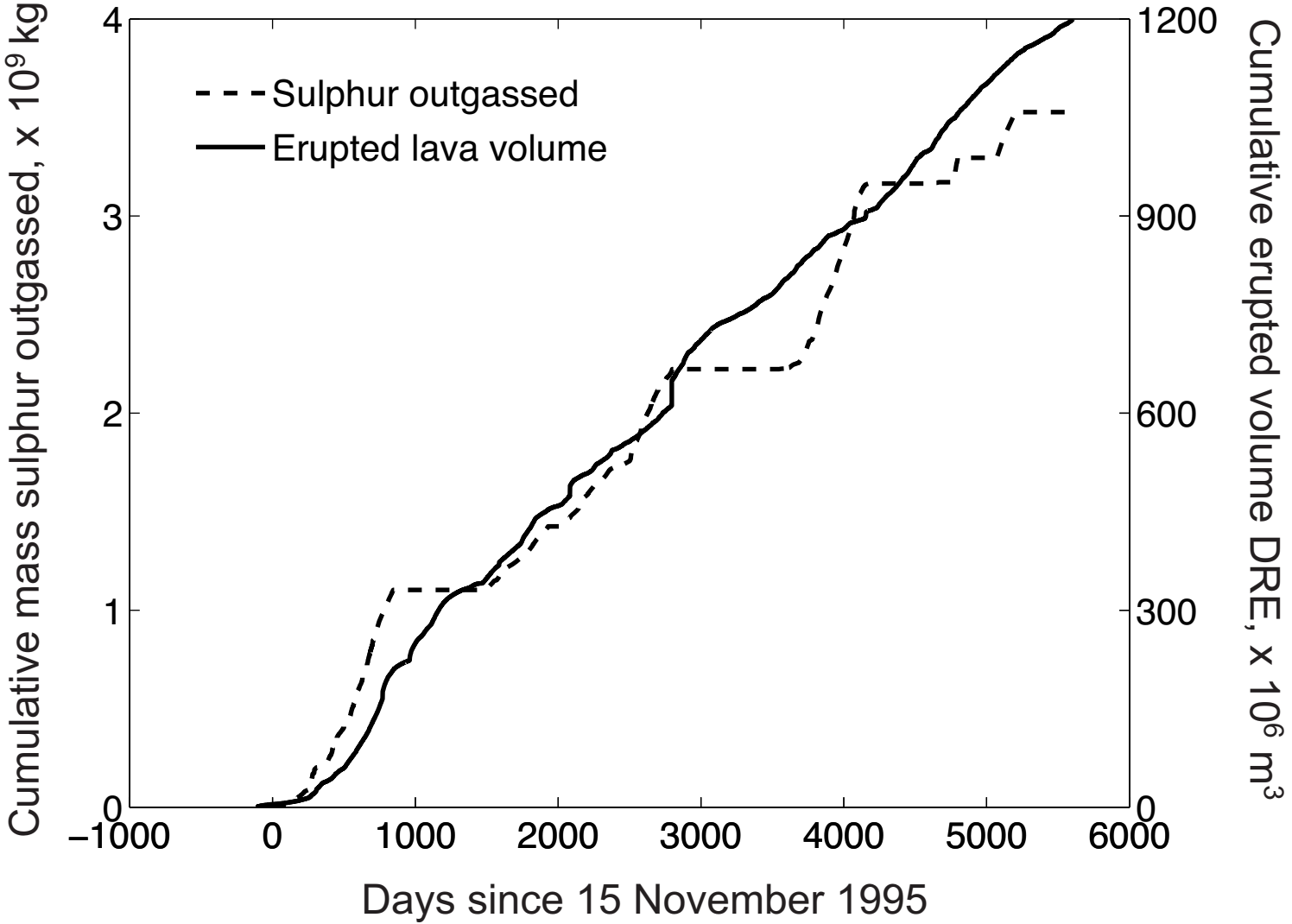
Sulphur outgassed
Erupted lava volume
Cumulative mass sulphur outgassed, x 10^9 kg
Cumulative erupted volume DRE, x 10^6 m^3
Days since 15 November 1995
0
1
2
3
4
0
300
600
900
1200
−1000
0
1000
2000
3000
4000
5000
6000

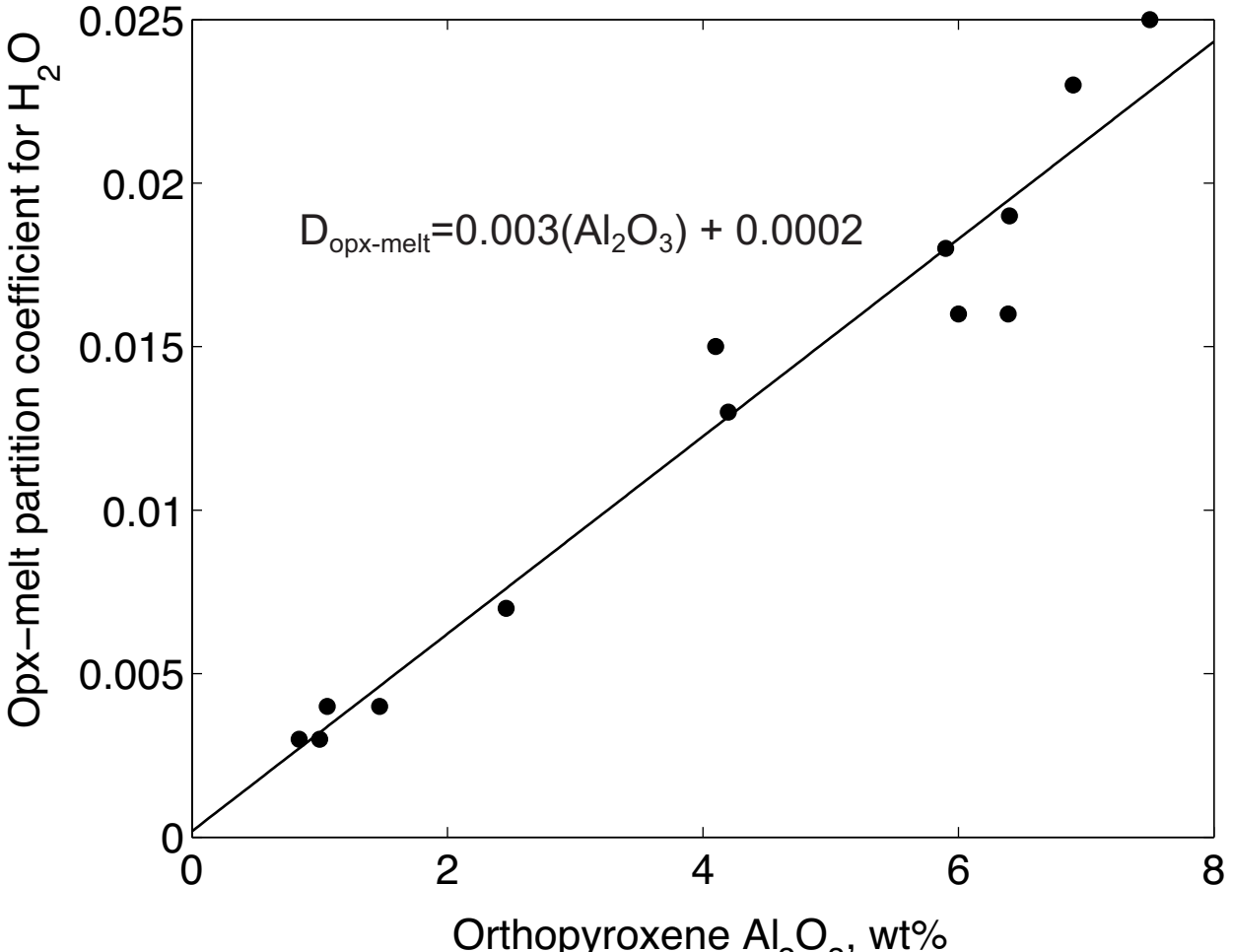
0.025
0.02
0.015
0.01
0.005
0
Opx–melt partition coefficient for H_2O
$D_{opx\text{-}melt}=0.003(Al_2O_3) + 0.0002$
0
2
4
6
8
Orthopyroxene Al_2O_3, wt%

a: opx grain 27

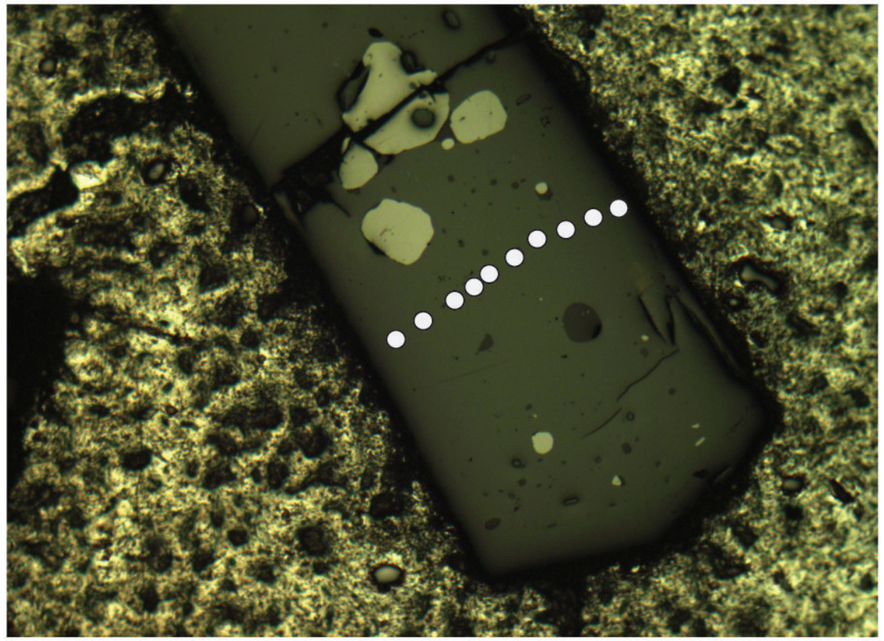

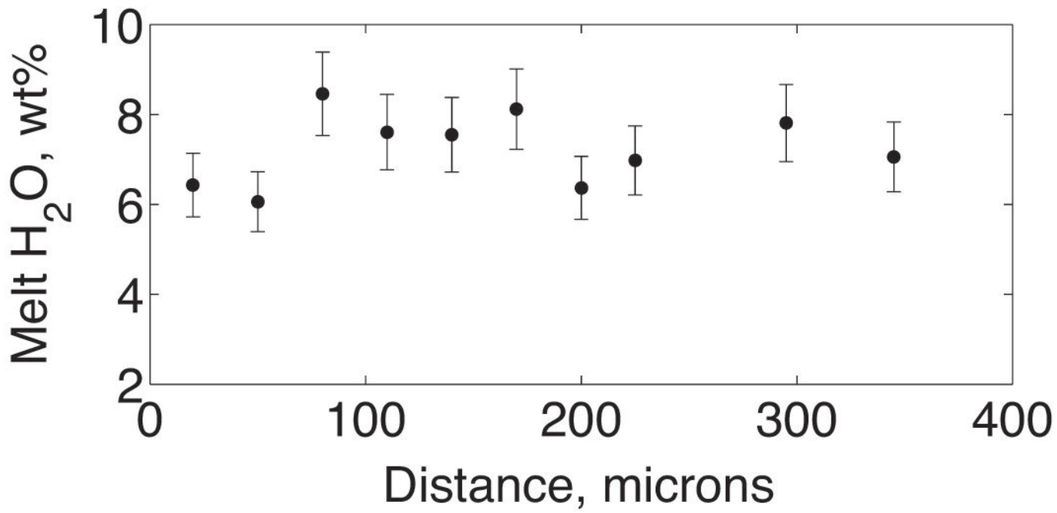

b: opx grain 12

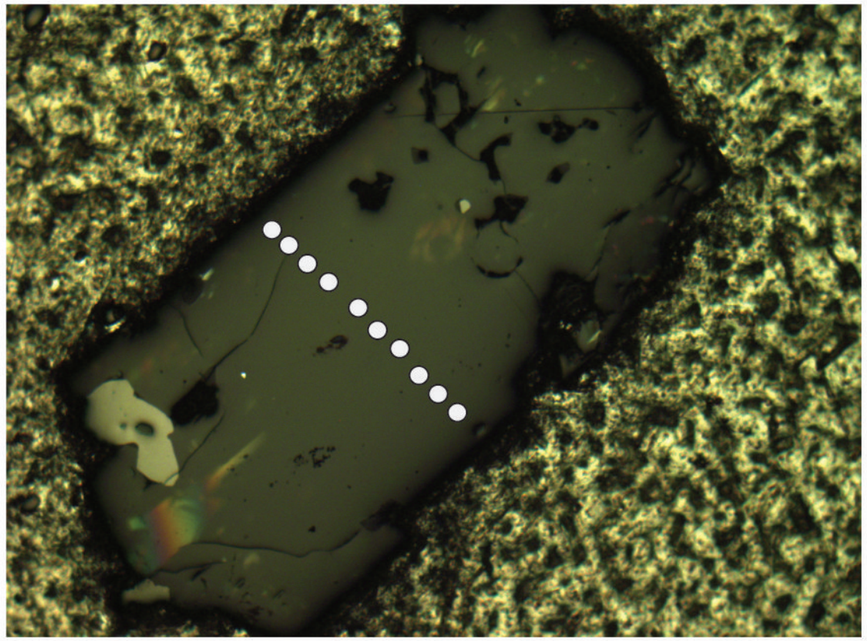

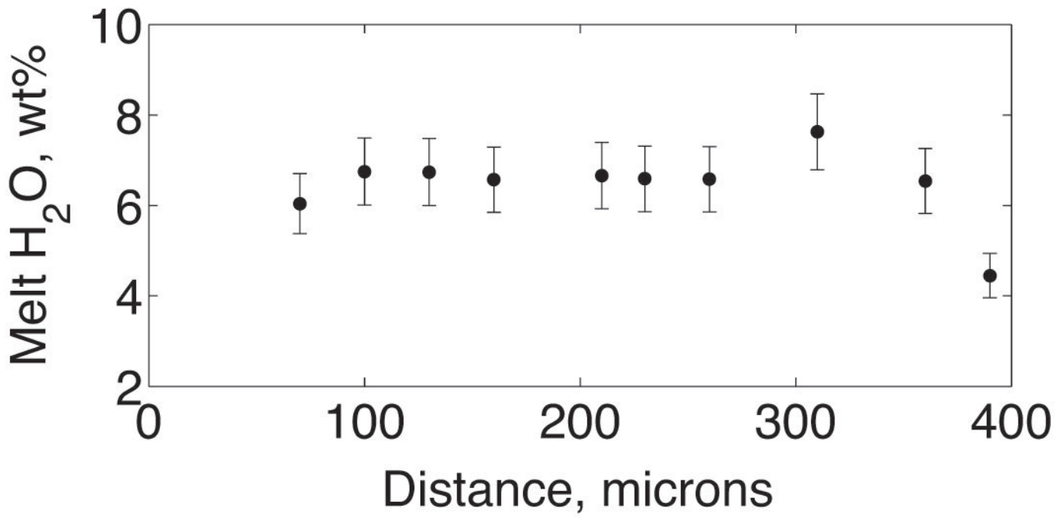

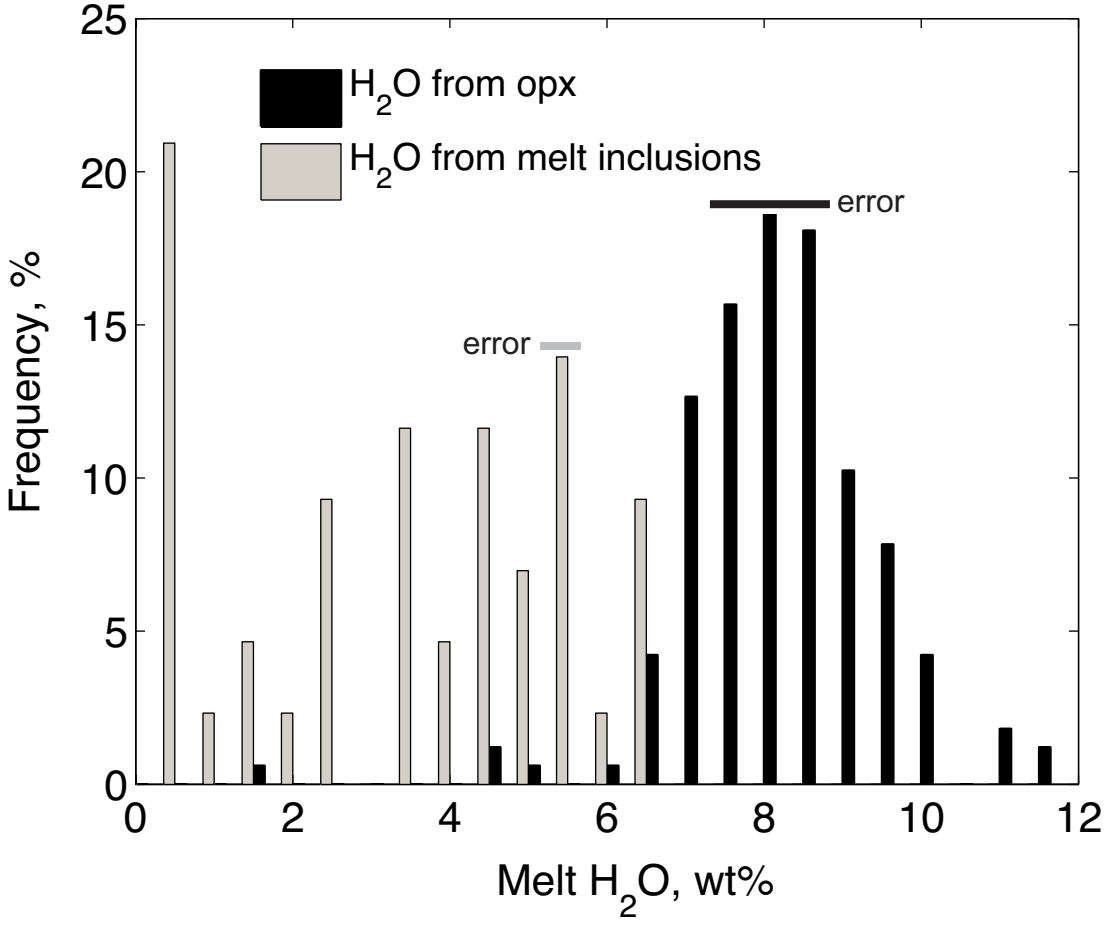
25
20
15
10
5
0
Frequency, %
0
2
4
6
8
10
12
Melt H2O, wt%
H2O from opx
H2O from melt inclusions
error
error

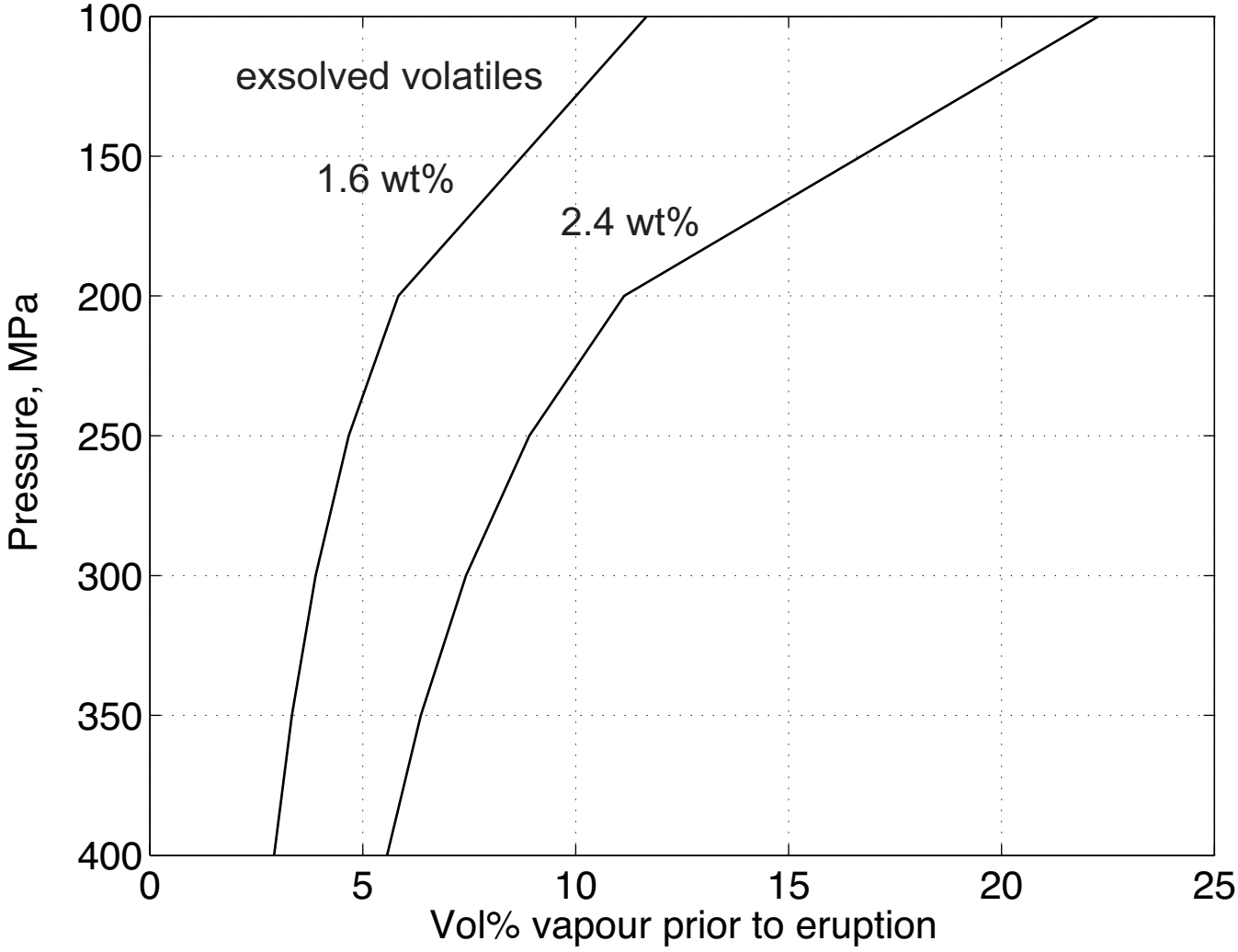
exsolved volatiles
1.6 wt%
2.4 wt%
Pressure, MPa
100
150
200
250
300
350
400
0
5
10
15
20
25
Vol% vapour prior to eruption

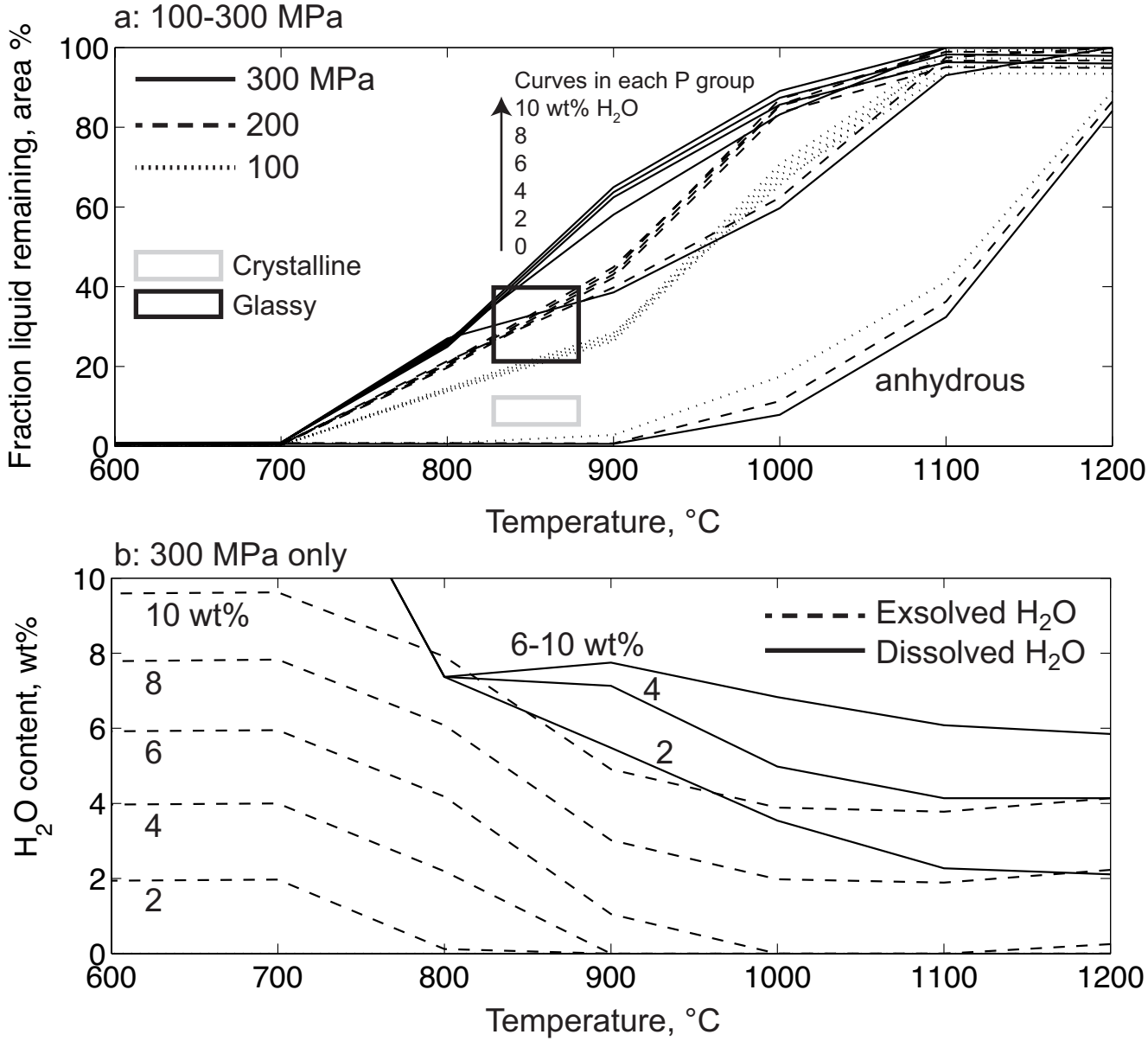
a: 100-300 MPa
Fraction liquid remaining, area %
300 MPa
200
100
Curves in each P group
10 wt% H2O
8
6
4
2
0
Crystalline
Glassy
anhydrous
Temperature, °C
b: 300 MPa only
H2O content, wt%
10 wt%
8
6
4
2
6-10 wt%
4
2
Exsolved H2O
Dissolved H2O
Temperature, °C

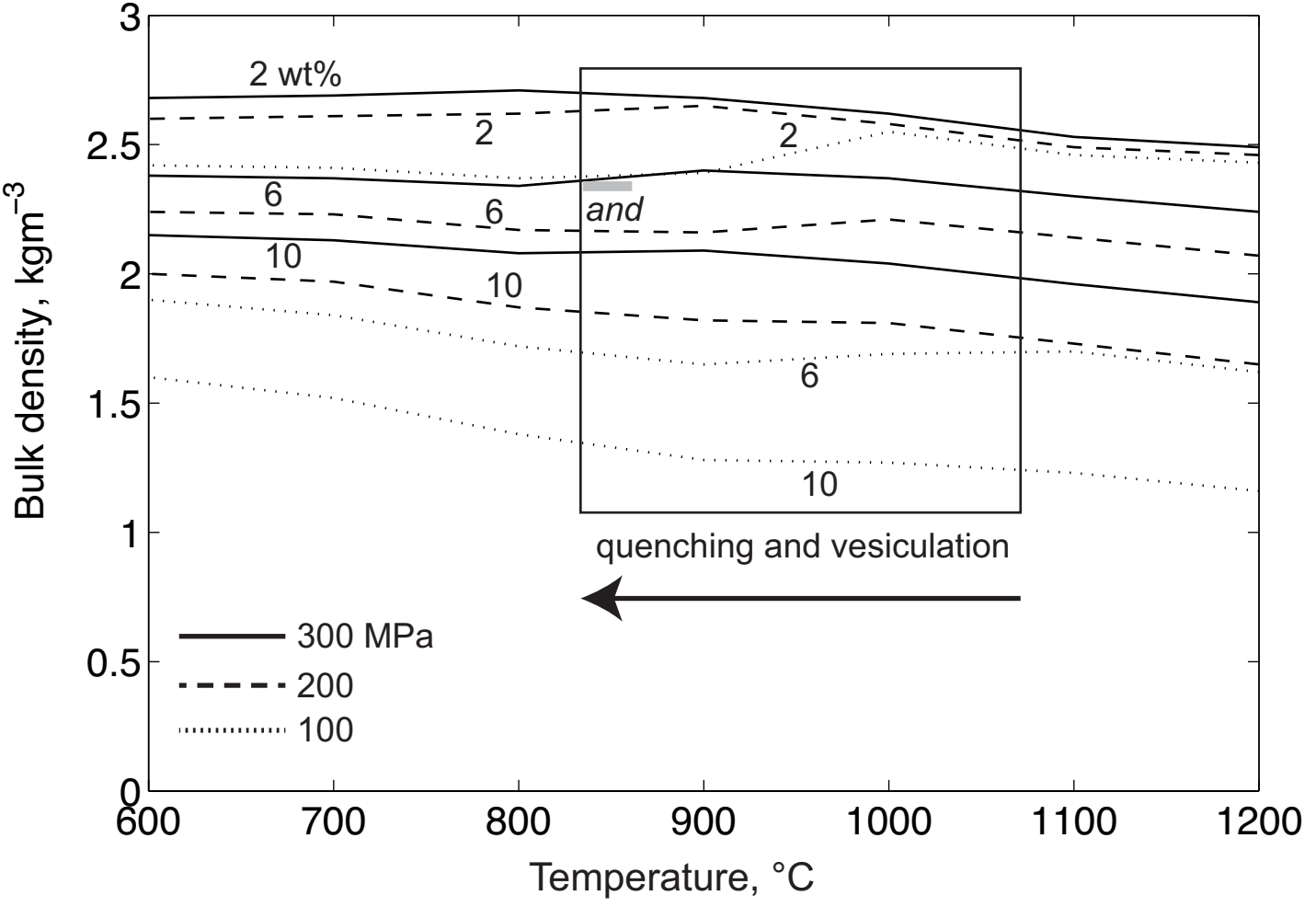
Bulk density, kgm^{-3}
Temperature, °C
2 wt%
2
6
10
2
6
10
and
6
10
quenching and vesiculation
300 MPa
200
100
0
0.5
1
1.5
2
2.5
3
600
700
800
900
1000
1100
1200

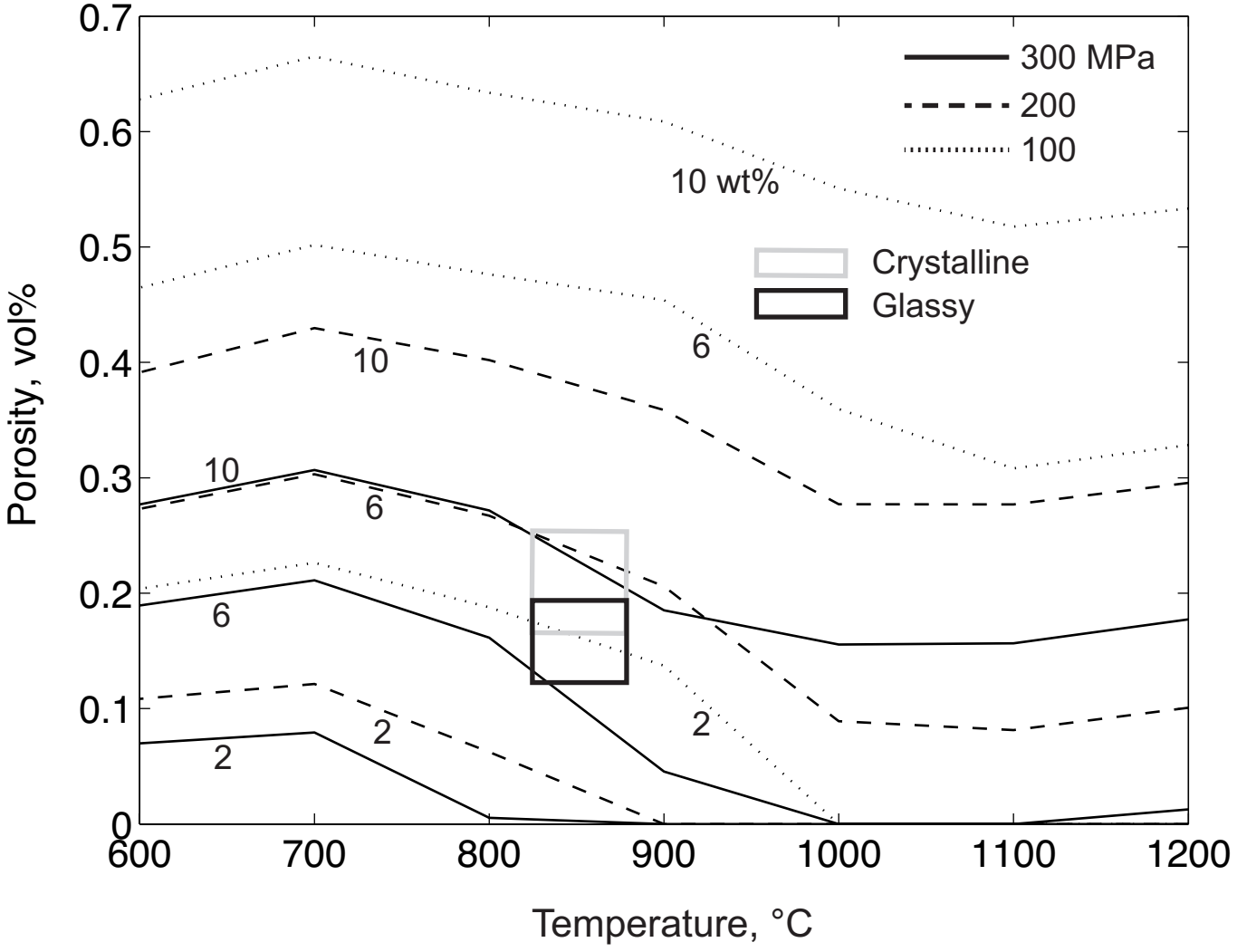
0.7
0.6
0.5
0.4
0.3
0.2
0.1
0
Porosity, vol%
600
700
800
900
1000
1100
1200
Temperature, °C
300 MPa
200
100
10 wt%
Crystalline
Glassy
10
10
6
6
6
2
2
2

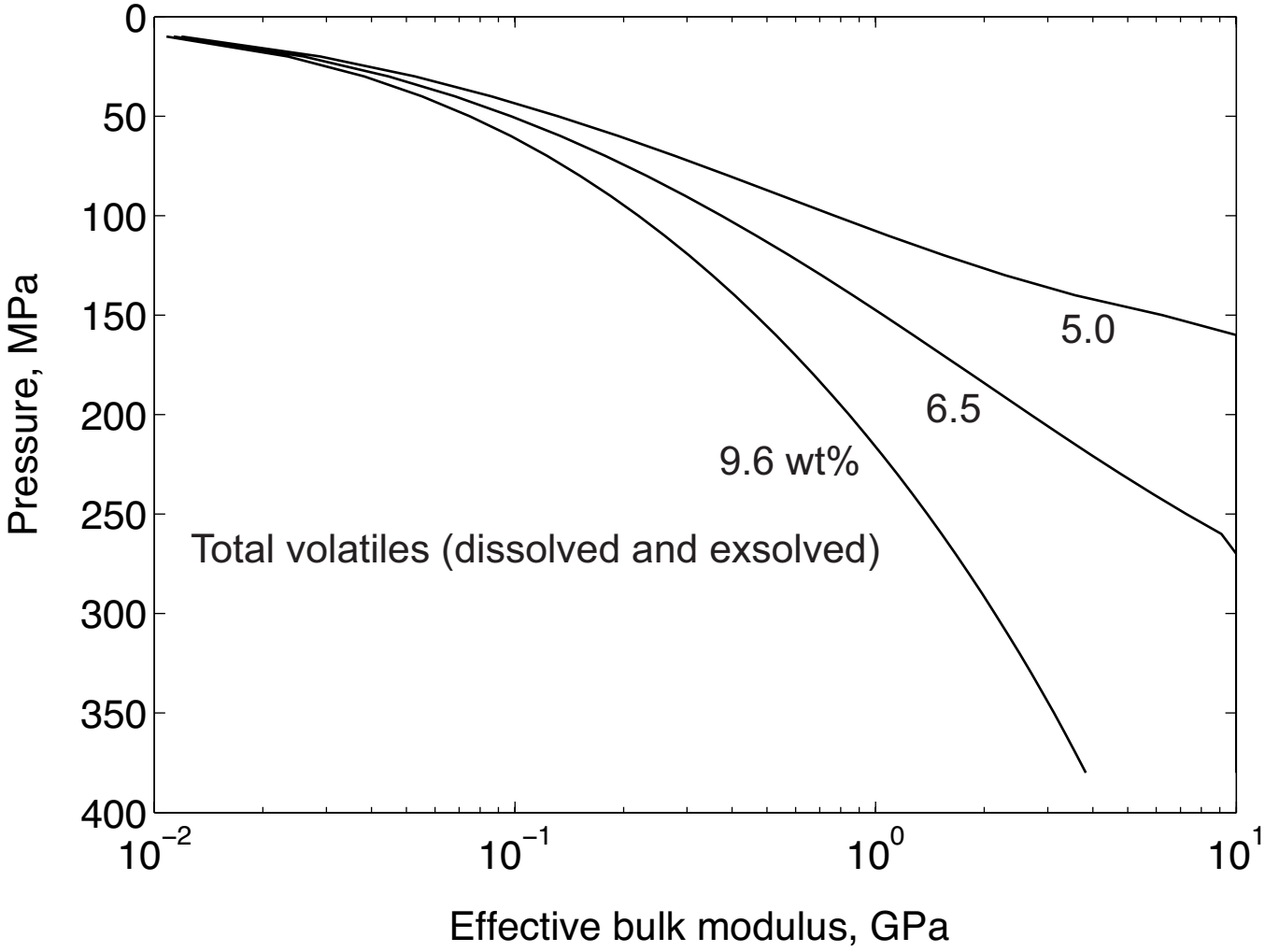
0
50
100
150
200
250
300
350
400
Pressure, MPa
10^{-2}
10^{-1}
10^{0}
10^{1}
Effective bulk modulus, GPa
5.0
6.5
9.6 wt%
Total volatiles (dissolved and exsolved)

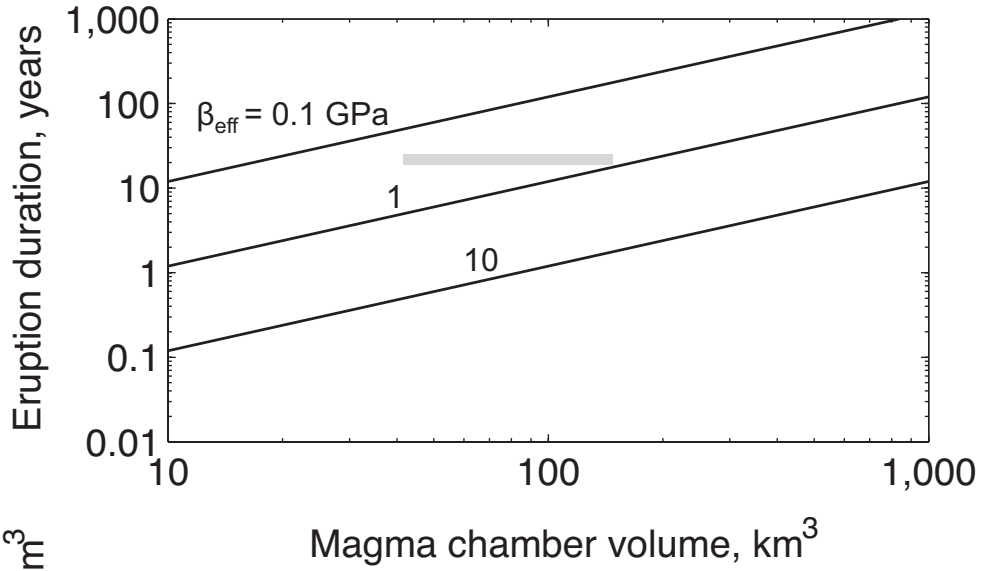
1,000
100
10
1
0.1
0.01
Eruption duration, years
β_{eff} = 0.1 GPa
1
10
10
100
1,000
Magma chamber volume, km^3

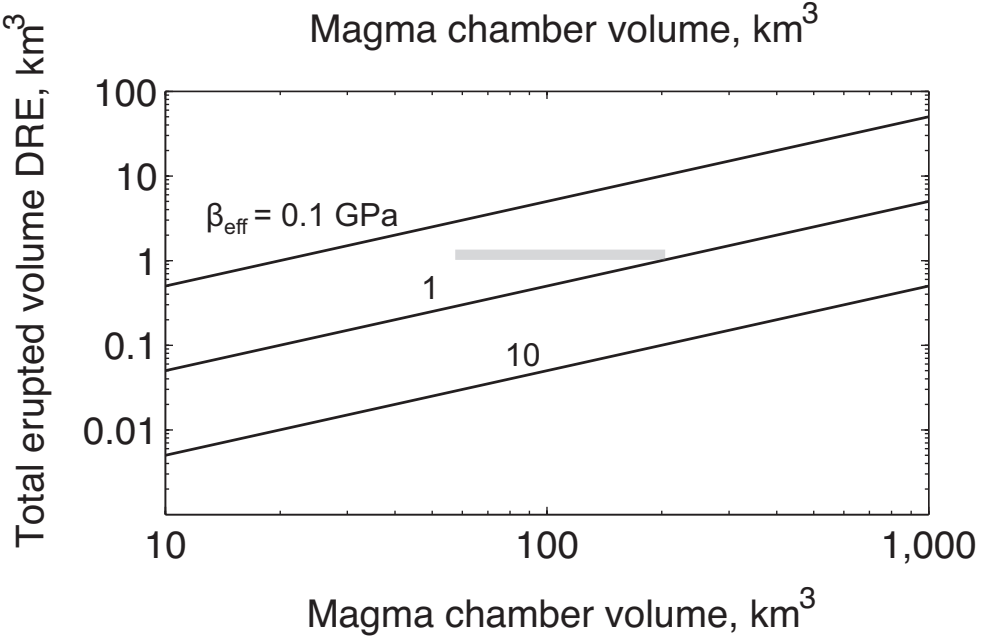
Total erupted volume DRE, km^3
100
10
1
0.1
0.01
β_{eff} = 0.1 GPa
1
10
10
100
1,000
Magma chamber volume, km^3

Table 1: Sample types and their emplacement/eruption dates used in this study.

Sample name	Sample type	Emplacement/eruption date	Used for:
BR1a-1	Crystalline MI	Emplaced block and ash flow deposit, 8 January 2007, Belham River Valley	Image analysis, textural studies
BR1a-2			
BR1a-3			
BR1a-All			
BR1b-1	MI margin		
BR1b-2	Andesite margin		
BR1b-3	Andesite		
BR1b-4	Crystalline MI		
BR1c-1	Andesite margin		
BR1c-4	MI margin		
BR1c-5	Crystalline MI		
BR10aa-1			
BR10aa-2			
BR10aa-3			
BR10aa-4			
BR10aa-All			
BR10ab-1			
BR10ab-2			
BR10ab-3			
BR10ab-4			
BR10ab-All			
BR11b-1	Glassy MI		
BR11b-2			
BR11b-3			
BR11b-4			
MT19-1	MI margin	Emplaced Aymer's River, January 2010	
MT19-2	Glassy MI		
MT19-3	Andesite margin		
MT19-4	Andesite		
MVO-1592-1	Andesite margin		
MVO-1592-2	Andesite		
MVO-1592-3	MI margin		
MVO-1592-4	Glassy MI		
MVO-1566-1	MI margin	White's River, emplaced January 2010	
MVO-1566-4	Glassy MI		
MVO-1542	Pumice (fall)	Erupted 12-15 July 2003	Image analysis, textural studies Orthopyroxene H_2O concentrations (SIMS) Orthopyroxene-hosted melt inclusion volatile concentrations (SIMS) Plagioclase-hosted melt inclusion volatile concentrations (SIMS)

Table 2: Melt inclusion volatile concentrations measured by SIMS at the NERC ion probe facility and at the ion probe facility at the Carnegie Institution. *Analysis in the form of grain number, melt inclusion number. Sample MVO1524d. Cl and H_2O data for the 4f ion probe from Humphreys et al. (2009). f.i.c.: fluid inclusion contamination.

Ion Probe	Analysis*	Host phase	H_2O, wt%	CO_2, ppm	S, ppm	Cl, ppm	F, ppm
Cameca 4f, NERC ion probe facility	2,2	Plagioclase	4.15	f.i.c.		4610	
	3,1		5.16	387		3590	
	4,1		6.24	546		4260	
	8,1		3.17	0		3670	
	9,1		2.06	0		2720	
	9,3		2.03	0		2060	
	10,1		5.07	1032		3560	
	15,1		5.07	0		4370	
	15,2		4.96	0		4300	
	15,3		5.50	836		3940	
	16,2		2.24	0		3090	
	14,2		4.28	0		3960	
	11,2		3.37	251		2900	
	4,2		1.14	0		2260	
Cameca 6f, Carnegie Institution	01,1		2.36	f.i.c.	23	1821	64
	02,2		6.18	18.8	19	5004	166
	02,2b		5.83	30.1	19	5335	175
	03,1		3.99	433	23	2714	92
	04,1		4.29	334	24	2732	75
	05,1		3.77	8.0	17	2812	99
	05,5		4.97	34.1	25	2988	106
	05,6b		0.23	2.3	10	1137	42
	08,1b		4.17	220	20	4964	200
	05,4		0.76	40.6	20	2044	82
	05,12		0.03	3.7	1	406	22
	05,12b		0.07	3.5	4	1758	103
	05,11		0.11	315	6	1500	76

	05,10		0.31	2.2	8	1840	96
	08,1		3.14	58.4	9	4457	170
	08,2		5.50	159	80	3404	101
	09,2		0.40	20.6	8	1044	46
	10,1		4.36	464	36	3214	104
	13,1		3.17	80.3	30	3085	79
	13,3		5.42	19.7	28	3982	126
	13,4		4.64	55.9	27	3531	100
	13,5		0.03	14.4	2	1405	83
	15,1		6.40	10.0	29	4000	307
	16,2		3.34	315	26	2494	143
	15,1	Orthopyroxene	0.34	5.2	21	736	89
	27,1		1.55	2.6	30	2999	327
	27,3		6.20	23.6	57	2782	156

Table 3: Orthopyroxene H_2O content in ppm, measured by SIMS, with distance across the orthopyroxene crystals in microns (10^{-6} m). Also shown are the measured Al_2O_3 concentrations in wt%, the calculated partition coefficient, $D_{H_2O}^{opx-melt}$, for H_2O between opx and melt (from the calibration curve in figure 9), and the calculated melt H_2O content, in wt%, which has an average uncertainty of +/- 11% (see text for more discussion). na: not analysed.

Crystal	Distance, microns	H_2O, ppm	Al_2O_3, wt%	$D_{H_2O}^{opx-melt}$	Melt H_2O, wt%		Crystal	Distance, microns	H_2O, ppm	Al_2O_3, wt%	$D_{H_2O}^{opx-melt}$	Melt H_2O, wt%
4	40	169	0.52	0.0017	9.7		16	1	134	na		
	150	168	0.57	0.0019	8.8			2	134	na		
	160	173	0.61	0.0020	8.5			3	144	na		
	200	175	0.61	0.0020	8.6			4	157	na		
	300	175	0.69	0.0023	7.8			5	151	na		
	500	174	0.56	0.0019	9.3			6	144	na		
	750	174	0.56	0.0019	9.2			7	140	na		
	775	164	0.48	0.0016	10.0			8	144	na		
	845	173	0.59	0.0020	8.7			9	144	na		
	945	181	0.49	0.0017	10.9			10	144	na		
	1005	163	0.50	0.0017	9.6			11	148	na		
1	40	142	0.65	0.0022	6.6		17	1	184	0.80	0.0026	7.1
	110	167	0.72	0.0024	7.1			2	162	0.72	0.0023	6.9
	200	157	0.51	0.0017	9.0			3	158	0.55	0.0018	8.6
	220	170	0.62	0.0021	8.2			4	167	0.65	0.0021	7.8
	300	160	0.72	0.0024	6.8			5	229	0.65	0.0021	10.7
2	40	173	0.67	0.0022	7.8		18	1	159	0.74	0.0024	6.6
	70	176	0.58	0.0019	9.1			2	150	0.49	0.0017	9.0
	70	150	0.58	0.0019	9.1			3	161	0.59	0.0020	8.2
	150	170	0.65	0.0021	7.0			4	145	0.56	0.0019	7.7
	180	155	0.76	0.0025	6.9			5	153	0.61	0.0020	7.5
	190	157	0.58	0.0019	8.0			6	142	0.54	0.0018	7.8
	210	172	0.58	0.0019	8.1			7	169	0.50	0.0017	9.9
	250	151	0.65	0.0022	8.0			8	142	0.54	0.0018	7.8
	290	144	0.54	0.0018	8.3			9	169	0.71	0.0023	7.2
	320	149	0.58	0.0019	7.4		19	1	155	0.61	0.0020	7.6
3	40	155	0.61	0.0020	7.6			2	170	0.62	0.0021	8.3
	70	157	0.56	0.0019	8.4			3	172	0.54	0.0018	9.5

	170	143	0.50	0.0017	8.5			4	199	0.88	0.0028	7.0
	130	154	0.52	0.0018	8.7			5	162	0.59	0.0020	8.2
	150	149	0.60	0.0020	7.4			6	173	0.64	0.0021	8.2
	200	157	0.60	0.0020	7.8			7	158	0.49	0.0017	9.5
5	50	138	0.48	0.0016	8.4			8	151	0.57	0.0019	7.9
	120	137	0.50	0.0017	8.0			9	149	0.54	0.0018	8.2
	150	170	0.57	0.0019	9.0		21	1	123	0.57	0.0019	6.5
	190	125	0.48	0.0016	7.6			2	146	0.59	0.0020	7.5
6	50	151	0.63	0.0021	7.2			3	150	0.55	0.0019	8.1
	100	157	0.61	0.0020	7.7			4	147	0.61	0.0020	7.2
	150	172	0.69	0.0023	7.5			5	153	0.61	0.0020	7.5
	175	167	0.65	0.0022	7.8			6	167	0.62	0.0021	8.1
	245	163	0.68	0.0022	7.3			7	150	0.66	0.0022	6.8
7	170	148	0.58	0.0019	7.6			8	152	0.52	0.0018	8.6
	100	152	0.58	0.0019	7.9			9	148	0.73	0.0024	6.2
	75	157	0.66	0.0022	7.2			10	166	1.15	0.0036	4.6
	300	180	0.63	0.0021	8.6			11	230	1.00	0.0032	7.2
8	520	148	0.68	0.0022	6.6			12	123	0.57	0.0019	6.5
	550	150	0.51	0.0017	8.7		22	1	136	0.55	0.0019	7.3
	580	156	0.61	0.0020	7.7			2	155	0.56	0.0019	8.2
	30	151	0.69	0.0023	6.6			3	150	0.56	0.0019	8.0
	80	149	0.61	0.0020	7.3			4	135	0.49	0.0017	8.0
	105	146	0.59	0.0020	7.5			5	136	0.47	0.0016	8.4
9	125	151	0.61	0.0020	7.5			6	149	0.51	0.0017	8.6
	155	175	0.72	0.0023	7.4			7	176	0.76	0.0025	7.1
	165	163	0.70	0.0023	7.1			8	140	0.53	0.0018	7.8
	180	151	0.69	0.0023	6.6			9	144	0.45	0.0015	9.4
	30	151	0.65	0.0022	7.0			10	146	0.53	0.0018	8.1
	80	172	0.72	0.0024	7.3		25	1	152	0.49	0.0017	9.0
	140	160	0.51	0.0017	9.2			2	182	0.70	0.0023	7.9
10	180	167	0.62	0.0021	8.1			3	184	0.65	0.0021	8.6
	205	179	0.72	0.0024	7.6			4	180	0.62	0.0021	8.7
	245	155	0.58	0.0019	8.0			5	160	0.62	0.0020	7.8
	285	149	0.52	0.0018	8.4			6	153	0.54	0.0018	8.4

	305	157	0.74	0.0024	6.5			7	149	0.50	0.0017	8.7
	325	162	0.51	0.0017	9.3			8	157	0.50	0.0017	9.2
	30	215	0.57	0.0019	na			1	135	0.63	0.0021	6.4
	70	213	1.11	0.0035	6.0			2	139	0.70	0.0023	6.1
	100	203	0.94	0.0030	6.7			3	147	0.51	0.0017	8.5
	130	202	0.93	0.0030	6.7			4	148	0.58	0.0019	7.6
	160	196	0.93	0.0030	6.6			5	145	0.57	0.0019	7.5
12	210	197	0.92	0.0030	6.7		27	6	156	0.57	0.0019	8.1
	230	197	0.93	0.0030	6.6			7	137	0.65	0.0021	6.4
	260	195	0.92	0.0030	6.6			8	134	0.58	0.0019	7.0
	310	195	0.79	0.0026	7.6			9	153	0.59	0.0020	7.8
	30	208	0.99	0.0032	6.5			10	155	0.67	0.0022	7.1
	70	151	1.06	0.0034	4.5			1	159	0.56	0.0019	8.5
	20	130	0.60	0.0020	6.5			2	147	0.50	0.0017	8.6
	50	197	0.61	0.0020	9.6			3	146	0.52	0.0018	8.3
	80	156	0.58	0.0019	8.0			4	160	0.61	0.0020	7.9
	120	141	0.57	0.0019	7.3			5	159	0.63	0.0021	7.6
	160	149	0.77	0.0025	5.9			6	160	0.58	0.0020	8.2
15	200	147	0.66	0.0022	6.8		28	7	163	0.63	0.0021	7.8
	250	161	0.73	0.0024	6.7			8	150	0.54	0.0018	8.3
	275	147	0.59	0.0020	7.5			9	155	0.53	0.0018	8.6
	325	156	0.52	0.0018	8.8			10	128	0.37	0.0013	9.7
	375	146	0.60	0.0020	7.3			11	133	0.42	0.0015	9.2
	385	125	na	na	na			12	140	0.53	0.0018	7.8
								13	110	0.39	0.0014	7.9

Table 4: Summary of textural data from image analysis backscatter images, including sample type, vesicle number density, bulk porosity (3-D), modal aspect ratio and modal shape factor. Calculations are described in the text.

Sample number	Type	Vesicle number density, m^{-3}	Bulk porosity	Modal Aspect Ratio	Modal Shape Factor
BR10a	Crystalline mafic inclusions	2.07×10^{12}	0.17	0.48	0.38
BR10b		2.67×10^{12}	0.22	0.58	0.43
BR11b		2.37×10^{12}	0.17	0.53	0.43
BR1a		2.49×10^{12}	0.25	0.48	0.43
BR1b		1.83×10^{12}	0.22	0.53	0.33
BR1c		1.75×10^{12}	0.21	0.53	0.43
MT19	Glassy mafic inclusions	8.69×10^{11}	0.12	0.43	0.38
MVO1587		1.31×10^{12}	0.19	0.63	0.33
MVO1592		2.34×10^{12}	0.11	0.53	0.28
BR11b	Mafic inclusion margin	2.70×10^{12}	0.16	0.63	0.48
BR1b		2.62×10^{12}	0.30	0.53	0.28
BR1c		2.11×10^{12}	0.21	0.53	0.58
MT19		9.30×10^{12}	0.07	0.53	0.53
MVO1592		2.75×10^{12}	0.11	0.53	0.38
BR11b	Andesite	1.70×10^{13}	0.24	0.43	0.53
BR1b		4.01×10^{13}	0.26	0.48	0.43
MT19		1.08×10^{14}	0.22	0.53	0.48
MVO1592		7.42×10^{13}	0.09	0.48	0.43
BR11b	Andesite < 5 cm from mafic inclusion	5.38×10^{13}	0.14	0.43	0.43
BR1c		7.11×10^{13}	0.18	0.48	0.38
MT19		9.97×10^{12}	0.13	0.53	0.33
MVO1592		7.23×10^{13}	0.12	0.48	0.33
BR12	Bomb	8.32×10^{13}	0.24	0.20	0.78
Pumice	Pumice	8.73×10^{13}	0.73	0.26	0.63

Table 5: Volcanic gas composition and flux, from Multigas and *DOAS instruments, July 2008 to January 2011. Fluxes are in 10^3 kg/day.

Date and time	Mean molar CO_2/SO_2	Mean molar H_2S/SO_2	SO_2 flux*	CO_2 flux	H_2S flux
10/7/08 13.00	5.3	0.6	460	1676	136
10/7/08 14.45	5.6			1771	
10/7/08 15.30		0.7			175
10/7/08 17.30	4.0	0.6		1265	153
10/7/08 19.30	4.5			1423	
11/7/08 10.00	5.0	1.0	411	1413	218
11/7/08 16.10	3.8	0.6		1074	136
11/7/08 16.45	3.8	0.7		1074	146
11/7/08 19.00		0.5			115
11/7/08 20.00	3.1	0.6		876	121
11/7/08 22.00	5.0	0.8		1413	182
12/7/08 14.00	5.5	0.6	404	1528	126
12/7/08 16.00	6.1	0.6		1694	138
12/7/08 20.00	5.5			1528	
13/7/08 2.00	5.9	0.7	561	2276	213
13/7/08 8.00		0.7			199
13/7/08 10.00		0.8			229
13/7/08 16.00		0.9			271
13/7/08 18.00	5.6			2160	
14/7/08 0.00		1.0	342		182
14/7/08 12.00	8.0	0.6		1881	107
14/7/08 18.00	4.0	0.8		941	140
14/7/08 20.00	6.0			1411	140
22/6/10 2.00		1.0	233		225
25/6/10 10.00	11.2		318	3566	
25/6/10 14.00	3.5	0.3	318	1105	106
26/6/10 10.00	1.0	0.8	311	308	251
28/6/10 2.00			383		
28/6/10 6.00	4.7		383	1809	
5/7/10 10.00	4.9		212	1032	
5/7/10 14.00			212		
9/7/10 6.00			227		
19/7/10 6.00			415		
20/7/10 6.00	4.0		393	1565	
8/8/10 6.00	9.1	1.5	292	2654	437
8/8/10 22.00	5.1	1.4	292	1491	406
9/8/10 2.00			383		
9/8/10 6.00	3.3	1.1	383	1263	421
31/8/10 10.00	11.0	0.9	324	3566	303
5/9/10 14.00	5.0	1.0	301	1505	293
11/9/10 10.00			216		
25/9/10 14.00		1.1	243		257
27/9/10 10.00			170		
1/10/10 2.00	15.1	1.8	365	5494	668
1/10/10 10.00	8.1	1.1	365	2955	415
15/10/10 2.00	6.6	1.8	222	1455	407
15/10/10 6.00		1.9	222		423
15/10/10 10.00		1.2	222		258
29/10/10 2.00	5.6	1.5	294	1649	442
4/11/10 10.00	8.3	2.6	403	3338	1051
5/11/10 14.00		0.9	394		370
5/11/10 18.00	7.7	1.6	394	3027	646
6/11/10 2.00	5.9	1.4	601	3564	869

Table 7: Estimation of oxygen fugacity relative to the NNO buffer and mafic magma H_2O content from 7 mafic amphibole compositions (spanning Mg-hastingsites and pargasites) measured by Murphy et al. (2000), using the empirical parameterisation of Ridolfi et al. (2006).

Wt%	**1**	**2**	**3**	**4**	**5**	**6**	**7**	**Mean**
SiO_2	42.8	43.1	41.9	41.7	40.8	41.2	47.1	**42.6**
TiO_2	1.77	1.72	1.78	1.68	1.94	1.78	1.65	**1.76**
Al_2O_3	12.2	12.0	13.3	14.1	14.4	14.0	7.5	**12.5**
FeO	13.4	12.8	13.0	12.5	14.0	12.5	12.5	**13.0**
MnO	0.24	0.25	0.19	0.21	0.29	0.21	0.39	**0.25**
MgO	13.4	14.1	13.4	13.4	12.2	12.7	14.4	**13.4**
CaO	11.7	11.6	11.8	11.8	11.2	11.5	11.4	**11.6**
Na_2O	2.21	2.23	2.35	2.38	2.16	2.22	1.77	**2.19**
K_2O	0.24	0.27	0.22	0.18	0.21	0.19	0.18	**0.21**
Total	97.9	98.8	98.0	98.0	97.1	96.3	96.8	**97.6**
ΔNNO	0.8	1.0	0.7	0.7	0.4	0.5	1.3	**0.8**
H_2O_{melt}	7.6	7.1	8.1	8.8	9.4	9.2	5.4	**7.9**